D180-30708-1

Final Report

Task 5 - Space Debris Measurement, Mapping and Characterization System

SPACE STATION INTEGRATED WALL DAMAGE AND PENETRATION DAMAGE CONTROL

By

B. M. Lempriere

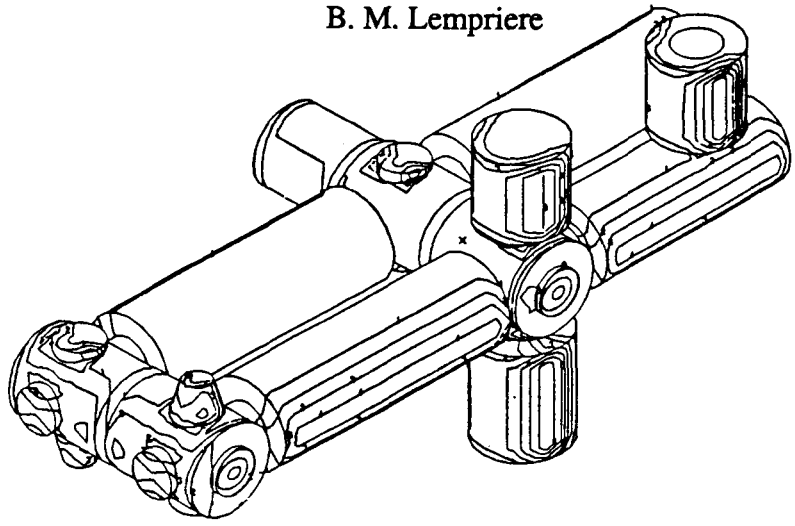

Prepared for

National Aeronautics and Space Administration

16 December 1987

Contract NAS8-36426
1 August 1987 to 16 December 1987

Technical Management
NASA George C. Marshall Space Flight Center
Marshall Space Flight Center, Alabama
Structures and Propulsion Laboratory

Structural Development
Sherman L. Avans

Boeing Aerospace Company
Seattle, Washington

D180-30708-1

Final Report

Task 5 - Space Debris Measurement, Mapping and Characterization System

SPACE STATION INTEGRATED WALL DAMAGE AND PENETRATION DAMAGE CONTROL

By

B. M. Lempriere

Prepared for

National Aeronautics and Space Administration

16 December 1987

Contract NAS8-36426
1 August 1987 to 16 December 1987

Technical Management
NASA George C. Marshall Space Flight Center
Marshall Space Flight Center, Alabama
Structures and Propulsion Laboratory
Structural Development
Sherman L. Avans

Boeing Aerospace Company
Seattle, Washington

This page left blank intentionally

ABSTRACT

This report documents the procedures and results of a study of a conceptual system for measuring the debris environment on the Space Station. The study was conducted in two phases: the first consisted of experiments aimed at evaluating location of impact through panel response data collected from acoustic emission sensors; the second analyzed the available statistical description of the environment to determine the probability of the measurement system producing useful data, and analyzed the results of the previous tests to evaluate the accuracy of location and the feasibility of extracting impactor characteristics from the panel response. The conclusions were that for one panel the system would not be exposed to any event, but that the entire Logistics Module would provide a modest amount of data. The use of sensors with higher sensitivity other than those used in the tests could be advantageous. The impact location could be found with sufficient accuracy from panel response data. The waveforms of the response were shown to contain information on the impact characteristics, but the data set did not span a sufficient range of the variables necessary to evaluate the feasibility of extracting the information.

KEY WORDS

Space Debris
Impact Tests
Transient Bending
Sensors
Space Environment
Panel Response
Spectral Analysis
Acoustic Emission

This page left blank intentionally

CONTENTS

This page left blank intentionally

FIGURES

List of Tables

This page left blank intentionally

1.0 INTRODUCTION

While developing techniques for repairing damage to the Space Station by meteoroid or debris impact, a need arose for a system to locate perforations that may be small and hidden.

A previous NASA proposal to develop a "nervous system" for the Space Station (Ref 1), included the suggestion that acoustic emission sensors could be used to locate impacts. It was stated that acoustic emission signatures might be correlated to specific types of event, but that sensor development was inadequate to allow the extraction of impactor characteristics.

A preliminary experiment conducted at BAC in 1986 on IR&D funding showed that acoustic emission sensors would provide a practicable means of collecting data from the impact response of a panel, and a simple algorithm was able to determine the impact location with satisfactory precision. This led to the present effort aimed at evaluating the potential of an impact detection and characterization system added on to an existing NASA/MSFC contract in two phases.

The purpose of the first phase was to evaluate the limitations of the location method from the point of view of designing a system with a reasonable number of sensors. The effort consisted mainly of conducting experiments.

The purpose of the second phase was to develop a conceptual design of an instrumentation system for deployment on the initial Space Station Modules for measuring, mapping, and characterizing the meteoroid/debris space environment. The data from this instrumentation would be used for the design of the "evolutionary" Space Station module meteoroid/debris protection system.

This report summarizes work accomplished under the NASA Contract NAS8-36426, "Integrated Wall Design and Penetration Damage Control", during the periods 1 January through May 31 and 1 August through 16 December 1987. This program was sponsored by NASA Marshall Space Flight Center with Mr. Sherman Avans as the Contracting Officer's representative. Performance of this contract was under the direction of the Engineering Technology Organization of the Boeing Aerospace Company with Mr. Paul Stern as Program Manager and Mr. Alex Coronado as Technical Leader.

A report (Ref 2) released at the completion of the first phase is superseded by this one.

This page left blank intentionally

2.0 THE MEASUREMENT SYSTEM

A concept for a measurement system was drawn. Data from the existing data-base on space debris distributions were used to identify the probability of the concept acquiring meaningful impact data. Data from impact experiments were then used to establish the feasibility of the system.

Two aspects of the proposed measurement system were evaluated: the sensitivity of the sensors in relation to the probabilities of experiencing measurable impacts and the ability to extract the needed data from sensor measurements. For these evaluations, the existing data base on space debris distributions were reviewed, and impact experiments were performed on panels, the motions being measured with several sensor types.

2.1 The Measurement System Concept

The concept for a space experiment uses an instrumented panel as a particle impact detector. Impacts of space debris on a panel will produce a vibrational response which can be monitored by sensitive yet simple instruments. Since the motions propagate as waves, relatively few sensors are needed to monitor a large area, typically one per square foot or more. Thin film sensors, cheap and easy to use and repair, can be placed on the inside of the shield plates, with electrical connections to a simple data collection system. The data extraction methods discussed below derive from waveform analysis and are not dependent on amplitude calibration, even if this changes with temperature.

By using existing panels such as the meteoroid/debris shields, the experiment is cost effective and not intrusive. The panels can be recovered eventually for analysis of any impact craters. The shield panels on the Logistics Module of the Space Station provide a useful opportunity for this experiment: they will be shielded from meteoroids from above by the rest of the structure, the surface is cylindrical in the plane of orbit and thus provides a directionally sensitive experiment, and the panels will be recoverable every 6 months when the module is retrieved. They are approximately 55 in. (1.4m) square with an area of about 2 sq.m. each, as sketched in Figure 1.

The data collection system is described by the electronic schematic given in Figure 2 which shows the functional blocks needed to provide the basic data functions of the system. These begin with a collection of sensors, typically 10 to a panel on each of up to 10 panels. For each sensor there is a microchip to provide digitization and a data buffer for about 200 points. Data flows through the buffer into a trigger circuit which selects the neighbors nearest to a given sensor which triggers at a preset signal level. This feature will only be necessary if required by limitations on computation or transmission systems. Data from these neighbors is then drawn from the buffers and recorded for further processing in-situ or for transmission.

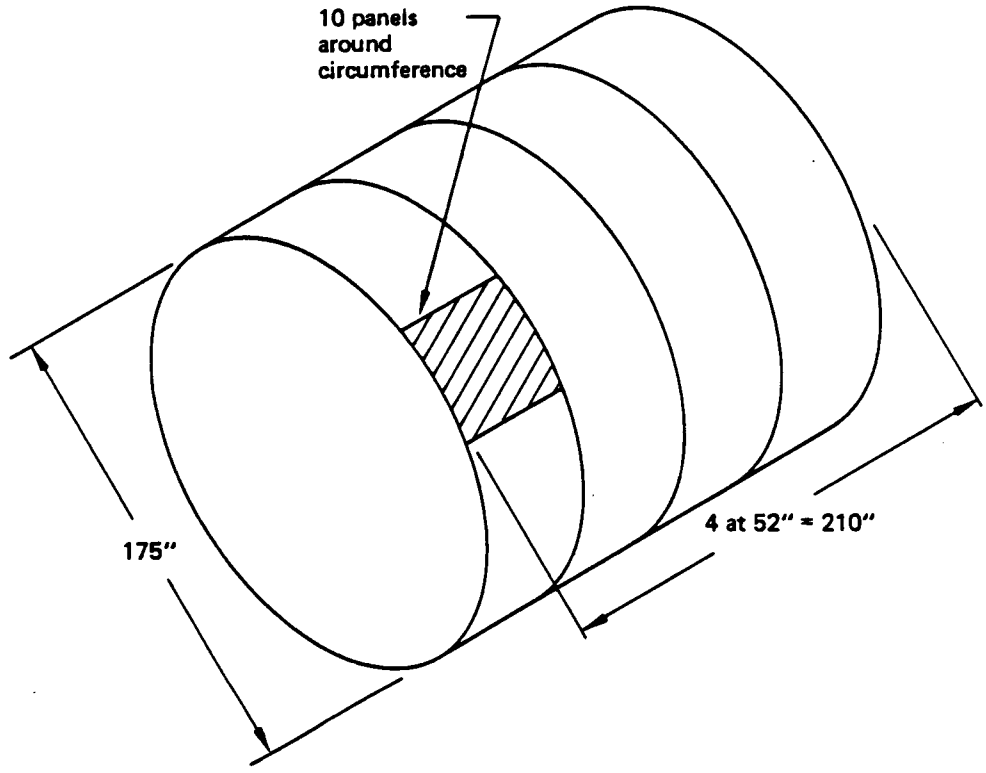

Figure 1. Typical Logistics Module Shield Panel

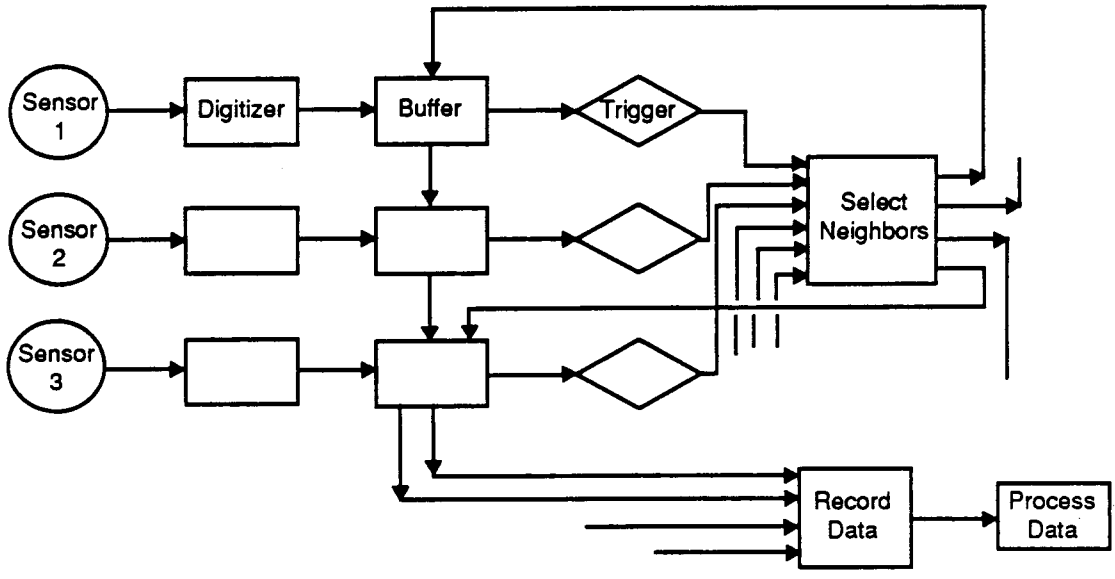

Figure 2. Schematic of Data Flow

The digitized data buffers will store approximately 0.5 ms of data at a sampling period of 5 microsecs. This is processed in real time to trigger recording at the first occurrence of a preset signal-to-noise ratio from any of the sensors. Signals from the immediate neighbors of the trigger sensor will be recorded for a period of 1 ms.

These signals will be used to locate the impact and to evaluate characteristics of the impact, eg its amplitude in time and spectral domains, its rise-time, and its phase spectrum. Eventual recovery of the panels will allow examination of the impact craters for further analysis of the impactor.

2.2 Probability Evaluations

The probability of impacts which could be monitored by the panel response system was estimated. To estimate the limits of detection, the system was assumed to respond to the transverse motions of elastic bending. These are governed by a dual wave equation whose solutions are determined by imparted momentum. For the small particles discussed below (with diameter-to-plate thickness ratio less than 0.1) the imparted momentum would be determined by the projectile momentum. The majority of the tests described in this report were in the elastic regime. The smallest impacts in the experiments used BB pellets. These were .172 (4.4 mm) dia. steel balls (density = 7.8 g/cc) having a mass of 342 milligrams. Velocities were around 280 ft/sec. (85 m/s), thus momentum was about 85 g.m/s. A set of tests was made using .156 in (4.0 mm) dia. nylon spheres (density = 1.1g/cc) having a mass of 37 milligrams, with velocities about 540 f/sec (165 m/s), and momentum of 6 g.m/s. The signals from the AE transducers were in most cases quite high so that it is plausible that a detection limit using these transducers would be a momentum of about 0.1 to 1 g.m/s.

The prescribed Space Debris environment for the Space Station as given by D.J.Kessler (Ref. 3) and reproduced in Figure 3a, shows that particles up to 0.03 mm can be expected at 400 Km and up to 0.06 mm at 500 Km altitudes. (Space Debris data presented by F. Hörz (Ref 4) reproduced in Figure 3(b) shows that particles up to 0.3 mm dia can be expected.) The most probable velocity is 12 to 14 Km/sec as shown in Figure 4. The momentum of an aluminum particle of this size and velocity is about 0.55 g.m/s (or 550 g.m/s for the Hörz data).

The expected number of impacts on the sensor during a typical mission within a range of momenta was determined with the following ground rules: (1) The sensor will be located on the Logistics Module which can be represented as a right circular cylinder whose axis lies along the local vertical; (2) The module is not shielded from the debris threat by any other component of the space station; and (3) The environment of JSC 20001 (Ref. 3) was used with a factor of 2 increase in flux. The increased flux level was proposed for this study by D.J. Kessler, the author of Reference 3, to account for the anticipated increase in the debris environment after the mid 1990's.

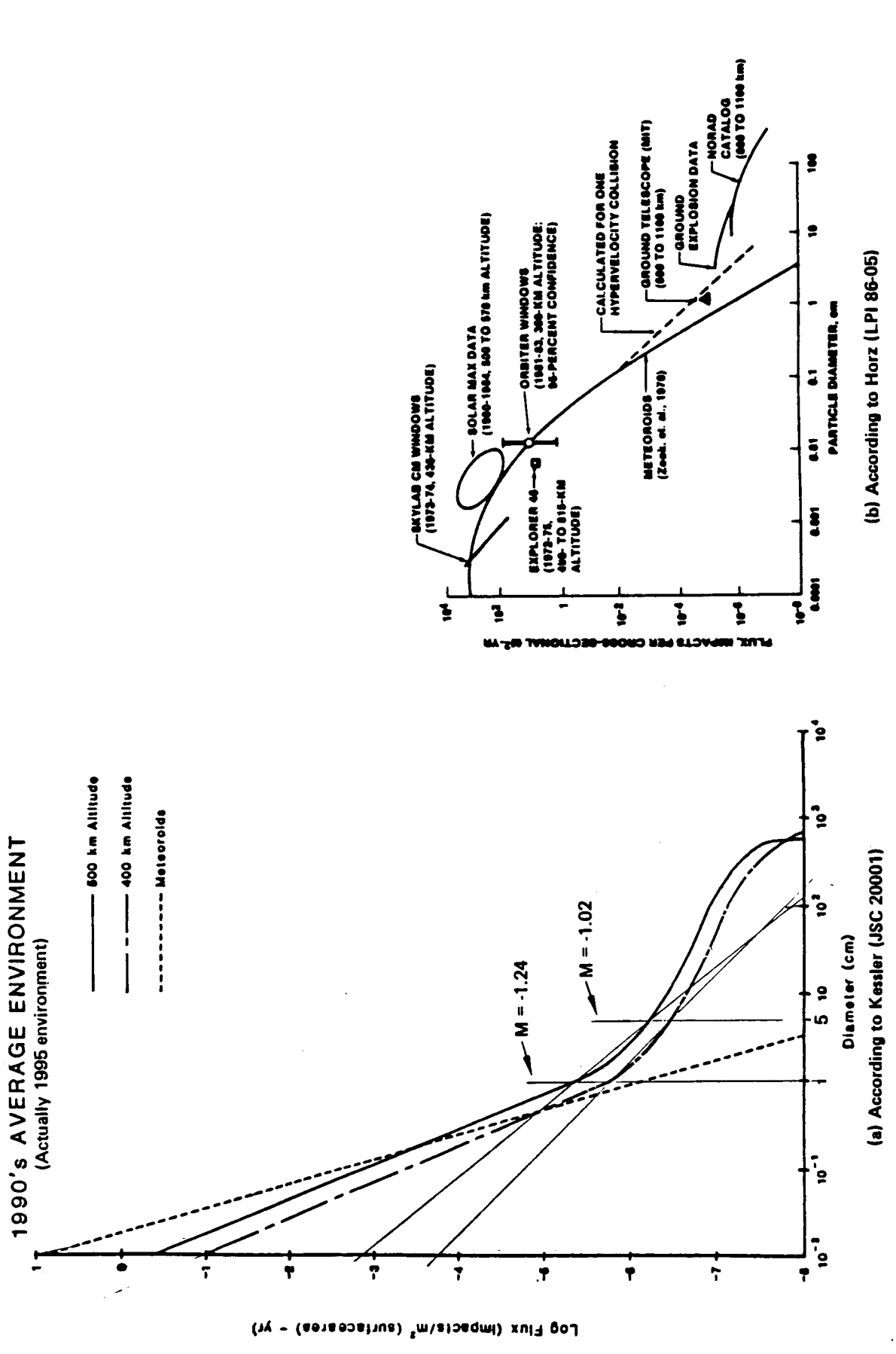

Figure 3. Space Debris Environment

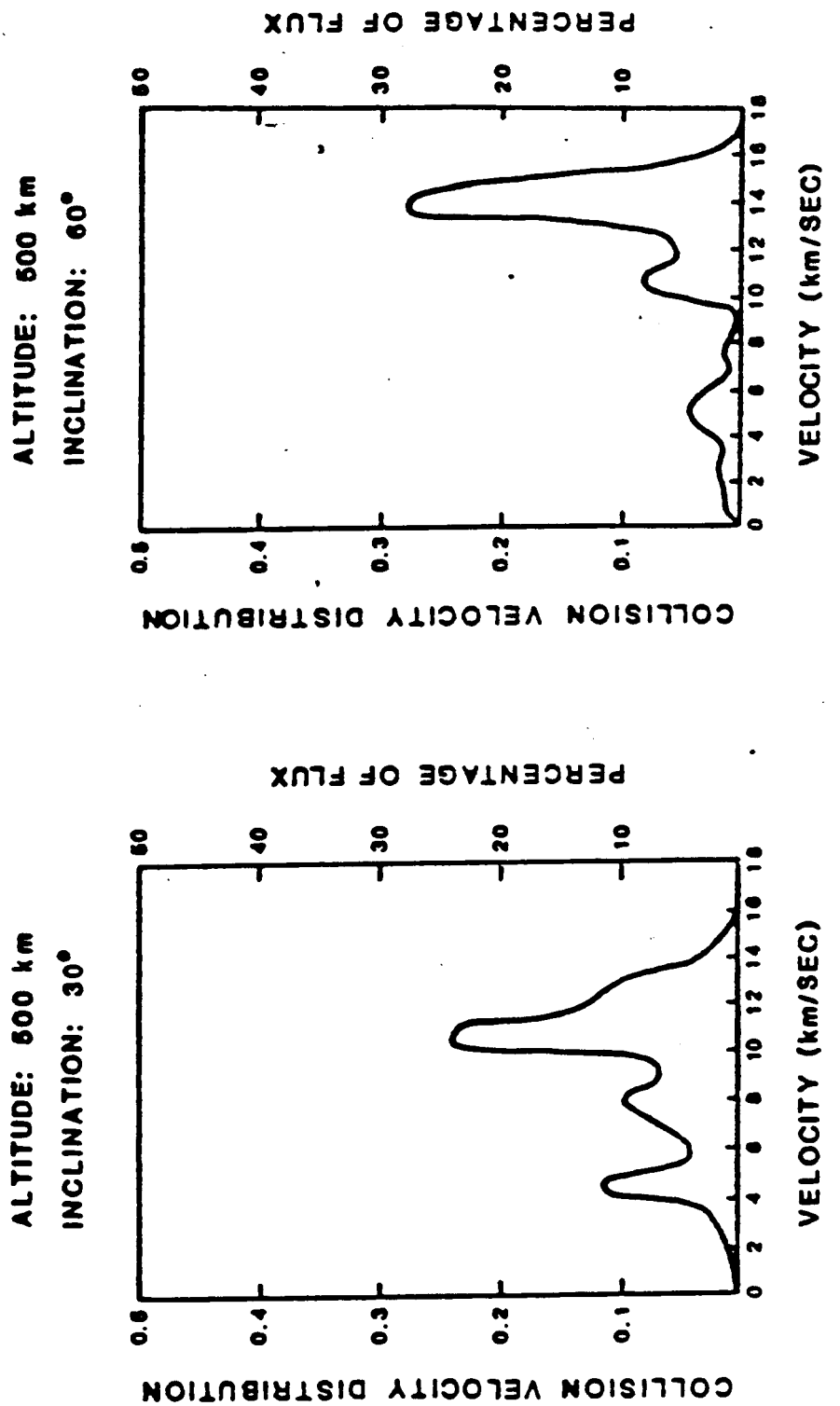

Figure 4. Probability Distributions for Debris Velocity (According to Kessler (JSC 20001))

The derivation of the governing equations is given in Appendix B. The two equations for the probability of momentum m or greater and the expected number of impacts with momentum m or greater were solved by the numerical approximations given in Figures 5 and 6 respectively. These equations were programmed using existing subroutines from the BUMPER analysis where possible. The momentum distribution is a function of the minimum diameter chosen, therefore, the minimum diameter was included as a user input. It was also desirable to include a multiplier on the flux equation as a user input. The rest of the inputs relate to the sensor geometry and exposure time as well as the integration steps.

$$G(m) = P(M \leq m) = \frac{V}{R}$$

$$V = \sum_{j=1}^{NPHI} \sum_{i=1}^{NT} H \left[\left[\frac{m}{CV(\theta_i)[\cos(\theta_i - \phi_j)]^+} \right]^{\frac{1}{3}} \right] \left[\cos(\theta_i - \phi_j) \right]^+ W(\theta_i) \Delta\theta\Delta\phi$$

$$R = \sum_{j=1}^{NPHI} \sum_{i=1}^{NT} \left[\cos(\theta_i - \phi_j) \right]^+ W(\theta_i) \Delta\theta\Delta\phi$$

where

H = $1 - \overline{H}$

$\overline{H}$ = $\frac{F_{DEB}(D)}{F_{DEB}(D_0)}$

NPHI = *Number of* ϕ *steps*

NT = *Number of* θ *steps*

Figure 5. Probability of Occurrence of Momentum m or Greater

$$N_{exp} = RHT \sum_{j=1}^{NPHI} \sum_{i=1}^{NT} F_{DEB} \left[\left[\frac{m}{CV(\theta_i)[\cos(\theta_i - \phi_j)]^+} \right]^{\frac{1}{3}} \right] \left[\cos(\theta_i - \phi_j) \right]^+ W(\theta_i) \Delta\theta\Delta\phi$$

where

NPHI = *Number of* ϕ *steps*
NT = *Number of* θ *steps*
R = *Radius of logistics module*
H = *Height of sensor panel*
T = *Exposure time of sensor*

Figure 6. Expected Number of Impacts of Momentum m or Greater

The analysis was performed using the default inputs for both the normal and absolute momentum calculations. The results are shown in Figures 7 to 9. The results indicate that for a typical 6 month mission a sensor in the most advantageous location will encounter fewer than 1 particle with sufficient momentum to register. Estimates for the expected number of impacts on the entire Logistics Module, as a function of particle diameter are given in Appendix B. The results show that for a momentum measurement system with a threshold of about 0.1 g.m/s, the probability of an event in the six-month period of each experiment is about 0.3.

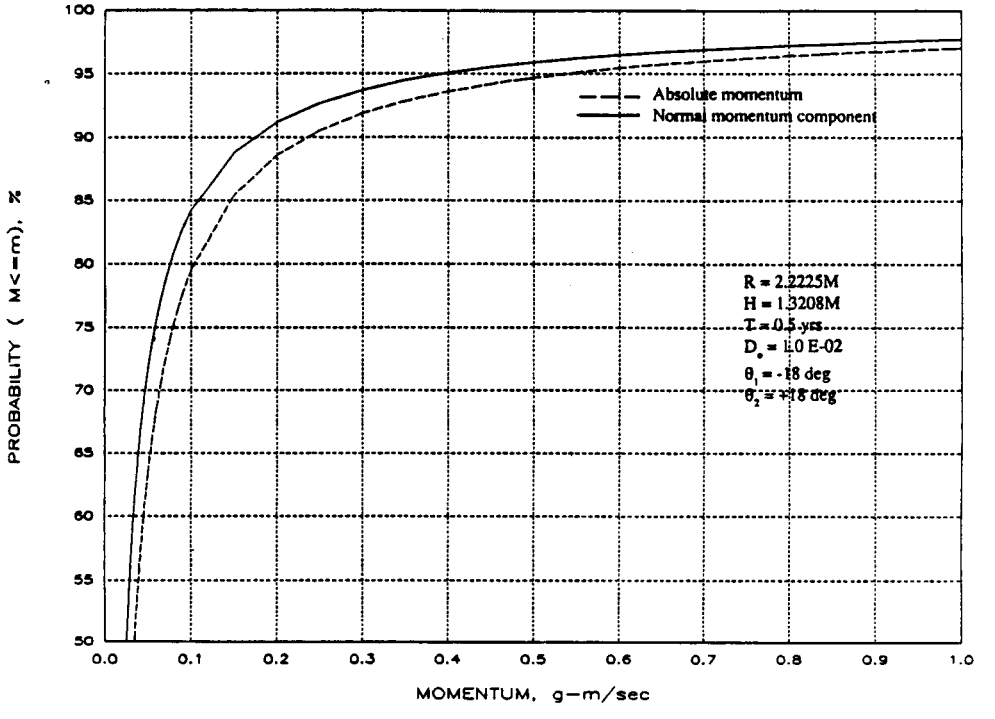

Figure 7. Momentum Distribution, $M \leq m$

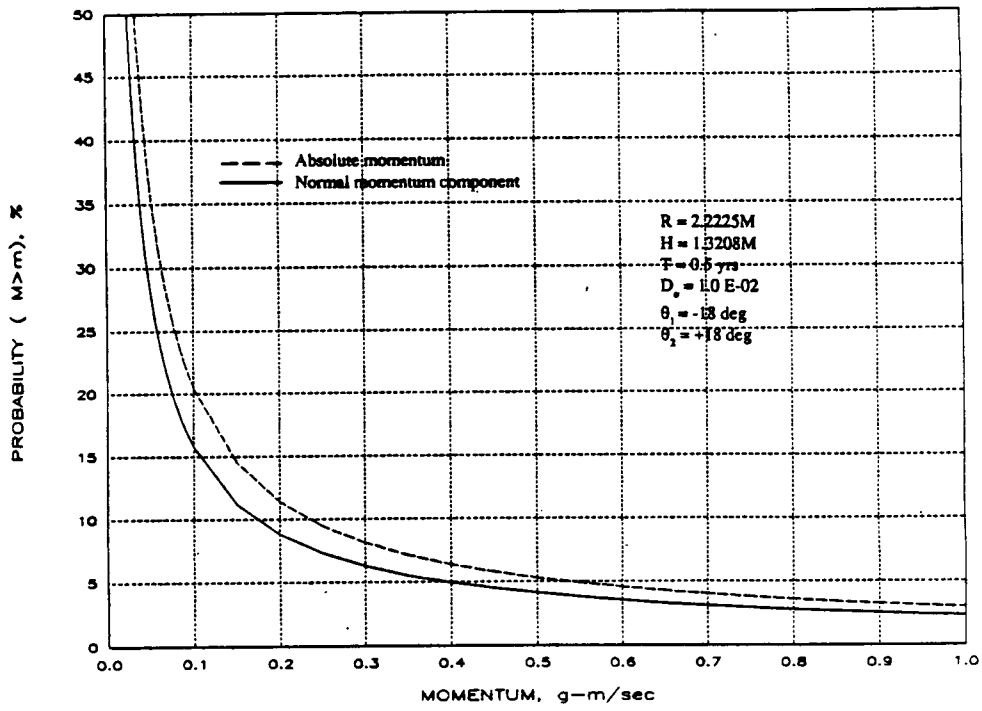

Figure 8. Momentum Distribution, M > m

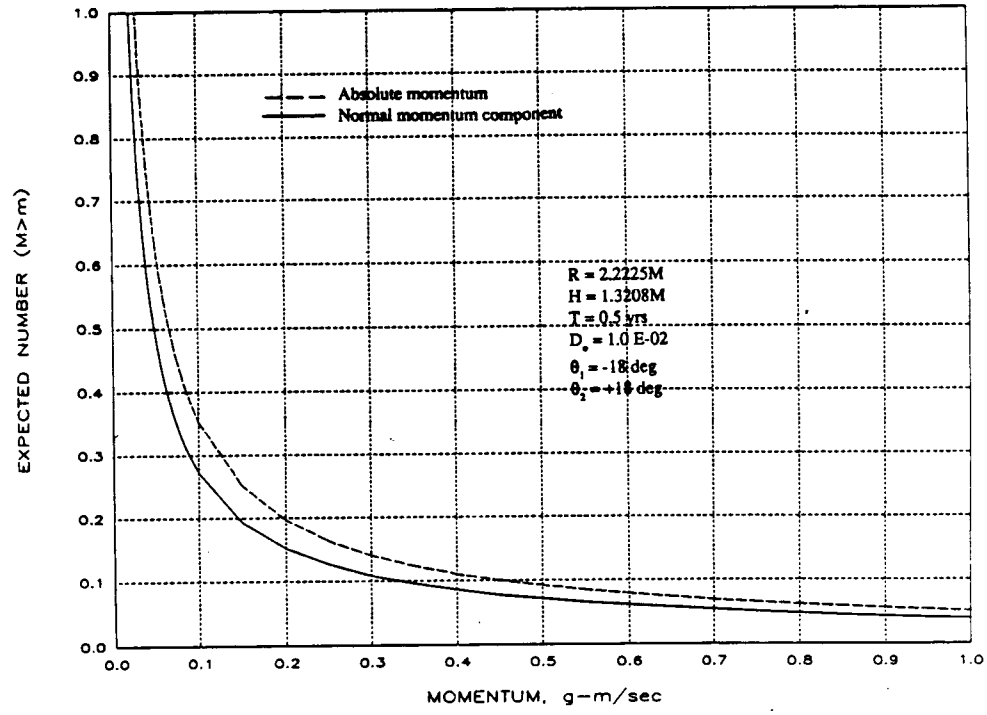

Figure 9. Expected Number of Impacts, M > m

3.0 IMPACT TESTS

Tests were made on a 1.22 m x 1.83 m x 4.76 mm (4 ft x 6 ft x 3/16 in) thick aluminum panel. The impactor was either a copper clad steel or a nylon BB from a common BB gun. A sample of the integrally-stiffened machined Space Station waffle panel shown in Figure 10 was used for a brief series of tests including 4 penetration tests under high velocity impact from a powder gun.

The first few tests were made using two wide-band acoustic emission sensors with a two-channel digitizer. A multi-channel device was acquired later to enable the recording of signals from several transducers on each test.

Broad band acoustics emission transducers were used for most of the measurements, but thin film polymer sensors and a low-frequency piezoelectric sensor were also used.

A large low-frequency (100 KHz) ultrasonic transducer was placed under the impact point in several tests to provide an impact time fiducial.

3.1 Descriptions Of Tests

The sequence of tests that were conducted to gather relevant data on sensor locations and gains, and impact locations and velocities is given in Tables 1-4. The test configurations of the later tests are shown in Figure 11a through f. The purpose of each test and a discussion of the test progression follows. The results are presented and discussed below. Reproductions of all recorded waveforms are given in Appendix A.

The first three tests of 01/21 were made to examine changes in the waveforms between two sensors spaced apart in a line. They were placed at 102 mm (4 in) and at 254 mm or 381 mm (10 in or 15 in) from the impact. Waveforms for the three tests are shown in Appendix A as Figure A-1. The several waveforms at 102 mm (4 in) and those at 254 mm (10 in) are quite similar to each other indicating repeatability. The 254 mm (10 in) waveforms exhibit the expected dispersion (spreading of the pulse to lower frequency at longer time) but their amplitudes were not the same.

Repeatability between tests was of concern, since distance effects could only be evaluated from data on repeated tests, because only two recording channels were available

The next series of six tests was made on 02/10 to provide data at several distances, with improved experimental techniques. The two transducers for each test were bonded with Loctite and the launcher was mounted at a fixed distance from the panel. The data for sensors at 125 mm, 178 mm, and 254 mm (5 in, 7 in, and 10 in)(figure A-2) showed expected changes with distance. The data from the near-in reference sensor at 76 mm (3 in) (figure A-3) showed considerable variation in signal strengths and waveforms among the tests.

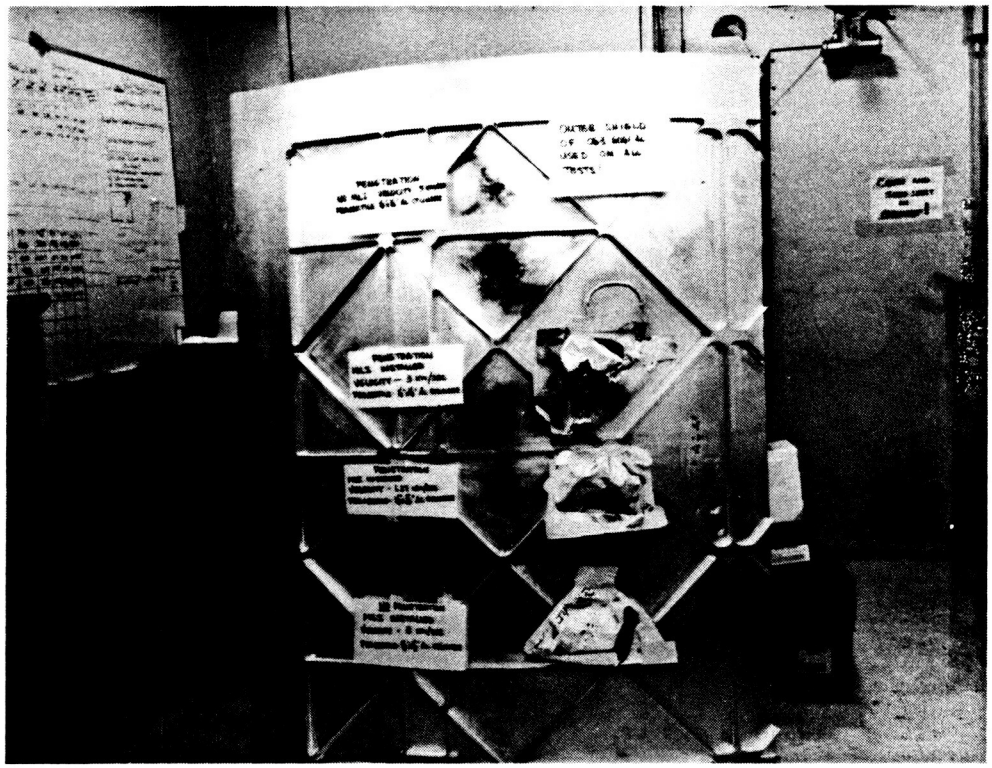

Complete Waffle Panel

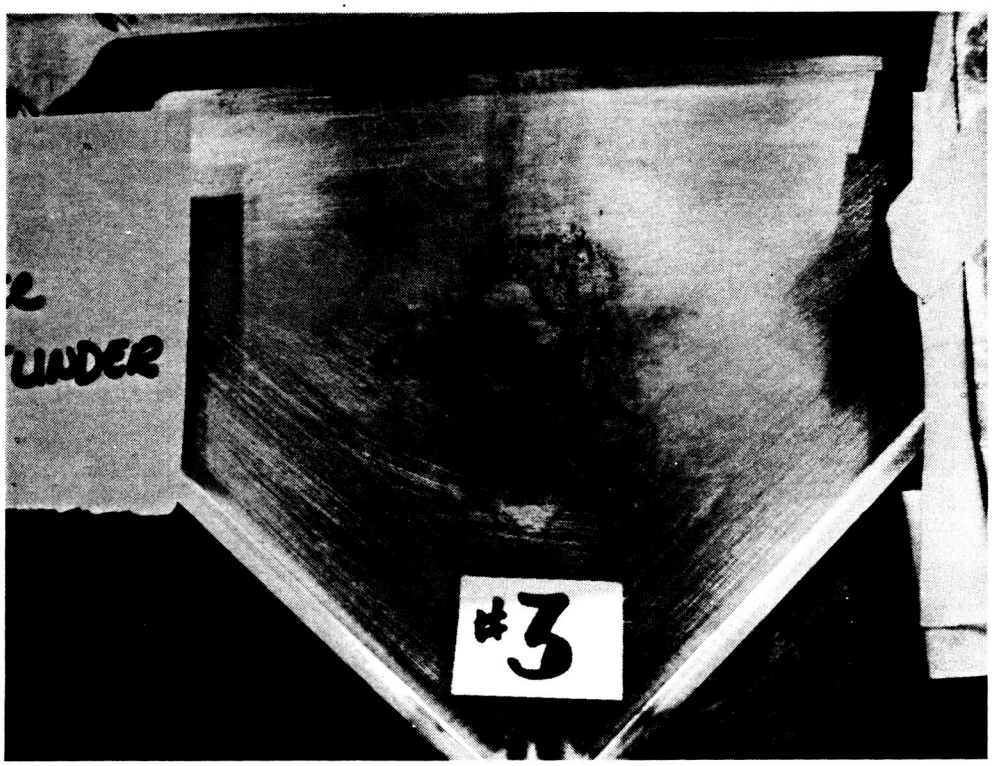

Closeup of shot (05/05)

Figure 10. Waffle Panel After Hypervelocity Impact

Table 1. Preliminary Tests

Note: Digitization Interval: 0.5 Microsec

Date	Data Id	Sensor Distance From Impact (ins)					Sensor Gain (v/div)	Measured Impact Velocity (ft/sec)
		#1	#2	#3	#4	#5		
Dispersion Data								
01/21/87	IMP1.DAT	4	10	-	-	-	1.0	-
01/21/87	IMP2.DAT	4	10	-	-	-	2.0	-
01/21/87	IMP3.DAT	4	-	15	-	-	2.0	-
02/10/87	IMPACT.DAT	3	-	7	-	-	5.0	-
02/10/87	IMPACT.DAT	3	-	7	-	-	5.0	-
02/10/87	IMPACT.DAT	3	5	-	-	-	5.0	-
02/10/87	IMPACT.DAT	3	5	-	-	-	5.0	-
02/10/87	IMPACT.DAT	3	-	-	10	-	5.0	-
02/10/87	IMPACT.DAT	3	-	-	10	-	5.0	-
Impact Velocity Data								
03/05/87	0306.AE	3	-	-	10[a]	0	5.0	293.3
03/06/87	0306.AE	3	-	7	-	0	5.0	285.3
03/06/87	0306.AE	3	5	-	-	0	5.0	285.8
Evaluate Transducer #4								
03/20/87	0320.AE	12	-	-	12	0	5.0	279.0
03/20/87	0320.AE	12	-	-	12	0	2.0	279.0

a - Gain = 2.0

Table 2. Multi-Channel Fixed Distance Data

Note: Digitization Interval: 1.0 Microsec

Date	Data Id	Sensor Distance From Impact (ins)					Measured Impact Velocity (ft/sec)
		#1	#2	#3	#4	#5	
03/25/87	0325_1.AE	12	12	12	12	0	270.0
03/25/87	0325_2.AE	12	12	12	12	0	268.7
04/01/87	0401.AE	12	12	12	12	-	265.5
04/01/87	0402.AE	12	12	12	12	-	261.6
		Sensor Gains (x1E04)					
	0325_1.AE	1.56	1.56	1.56	0.31	7.80	
	0325_2.AE	1.56	3.13	0.31	3.13	1.56	
	0401.AE	1.56	1.56	3.13	0.16	-	
	0402.AE	3.13	3.13	0.31	3.13	-	

Table 3(a) Location Tests

Notes: Digitization interval: 1.0 microsec
Locations of sensors and impacts shown in Figs 11(a) to (f).

Date	Data Id	Measured Impact Velocity (ft/sec)	Impactor
Flat Panel			
04/06/87	0406_1.AE	260.3	Steel ball
04/06/87	0406_2.AE	260.3	Steel ball
04/06/87	0406_3.AE	270.2	Steel ball
04/06/87	0407-1.AE	268.7	Steel ball
04/14/87	0414_1.AE	520.5	Nylon sphere
04/14/87	0414_2.AE	540.8	Nylon sphere
04/14/87	0414_3.AE	520.2	Nylon sphere
04/14/87	0414_4.AE	526.0	Nylon sphere
Waffle Panel			
Low velocity			
04/20/87	0420_1.AE	536.0	Nylon sphere
04/20/87	0420_2.AE	539.7	Nylon sphere
04/20/87	0420_3.AE	537.8	Nylon sphere
04/20/87	0420_4.AE	538.9	Nylon sphere
04/20/87	0420_5.AE	555.1	Nylon sphere
04/20/87	0420_6.AE	520.4	Nylon sphere
04/23/87	0423_1.AE	262.1	Steel ball
04/23/87	0423_2.AE	263.4	Steel ball
04/23/87	0423_3.AE	256.1	Steel ball
04/23/87	0423_4.AE	267.9	Steel ball
04/23/87	0423_5.AE	276.9	Steel ball
04/23/87	0423_6.AE	258.4	Steel ball
High velocity			
05/04/87	0504_1.AE	3.10 km/sec	1/4" dia x 1/4" long Al, no MLI
05/04/87	0504_2.AE	3.22 km/sec	1/4" dia x 1/4" long Al, with MLI
05/05/87	0505_1.AE	1.27 km/sec	1/4" dia x 1/4" long Al, no MLI
05/06/87	0506_1.AE	3.30 km/sec	1/8" dia x 1/8" long Al, no MLI

Note: MLI=Multi-layer insulation

Table 3(b). Sensor Gains and Types for Location Tests

Test Number	Sensor Gain (x1E04)						
	1	2	3	4	5	6	7
0406-1	3.13	3.13	3.13	3.13			
0406-2	1.56	7.81	3.13	1.56			
0406-3	3.13	7.81	3.13	3.13			
0407-1	3.13	7.81	1.56	3.13			
0414-1	0.78	0.78	1.56	0.78			
0414-2	0.78	0.78	1.56	0.78			
0414-3	0.78	0.78	1.56	0.78			
0414-4	0.78	0.78	1.56	0.78			
0420-1	1.56	1.56	0.016(K)	1.56	0.078(K)		
0420-2	1.56	1.56	0.160(K)	1.56	0.078(K)		
0420-3	1.56	0.78	0.16-(K)	3.12	0.078(K)		
0420-4	0.16	3.12	0.031(K)	0.31	0.016(K)		
0420-5	0.78	1.56	0.078(K)	0.78	0.031(K)		
0420-6	0.78	0.78	0.016(K)	0.78	0.078(K)		
0423-1	7.81	3.13	3.13	7.81	0.16(K)	3.13(S)	0.078(S)
0423-2	7.81	7.81	1.56	7.81	0.16(K)	3.13(S)	0.078(S)
0423-3	7.81	7.81	1.56	7.81	0.16(K)	3.13(S)	0.078(S)
0423-4	7.81	7.81	1.56	7.81	0.16(K)	3.13(S)	0.160(S)
0423-5	0.078	7.81	0.78	0.78	0.16(K)	1.56(S)	0.078(S)
0423-6	0.078	3.13	0.78	3.13	0.16(K)	3.13(S)	0.078(S)
0504-1	7.81	7.81	7.81	7.81	1.56(K)	7.81	7.81(S)
0504-2	15.63	7.81	7.81	7.81	1.56(K)	15.63	7.81(S)
0505-1	15.63	7.81	7.81	7.81	0.78(K)	15.63	0.78(S)
0506-1	7.81	7.81	7.81	3.13	0.78(K)	7.81	3.13(S)

NOTES:

(K) designates "Kynar" thin foil sensor

(S) designates "Sondicator" low frequency piezo sensor

All other data are for acoustic emission (AE) sensors

Table 4. Impact and Transducer Locations and Edge Echo Paths

			Direct Min Echo			First Pulse	
	X(cm)	Y(cm)	Path(mm)	Path (cm)	Dirn	TOA(mus)	Tprop
#406-1							
Impact	147.8	75.1					
Xdcr #1	151.8	91.1	164.92	68.07	E	194	32.8
Xdcr #2	91.4	91.3	586.80	95.80	N	271	109.8
Xdcr #3	91.5	29.8	722.62	119.05	S	297	135.8
Xdcr #4	152.4	30	453.34	79.57	E	240	78.8
						161.2	
#406-2						5.40	
Impact	83.8	92.4					
1	151.8	91.1	680.12	90.91	N	309	123.6
2	91.4	91.3	76.79	60.62	N	198	12.6
3	91.5	29.8	630.72	121.88	N	308	122.6
4	152.4	30	927.35	139.48	N	354	168.6
						185.4	
#406-3							
Impact	98.6	71.4					
1	151.8	91.1	567.30	97.19	N	263	110.4
2	91.4	91.3	211.62	81.46	N	195	42.4
3	91.5	29.8	422.02	101.45	S	229	76.4
4	152.4	30	678.85	114.79	S	283	130.4
						152.6	
#407-1						5.23	
Impact	98.6	97.2					
1	151.8	91.1	535.49	76.91	N	282	103
2	91.4	91.3	93.09	55.81	N	194	15
3	91.5	29.8	677.73	117.06	N	305	126
4	152.4	30	860.83	128.45	N	334	155
						179	
#414-1						5.43	
Impact	99.1	38.1					
1	151.8	91.1	747.41	126.17	N	301	139.2
2	91.4	91.3	537.54	114.70	N	264	102.2
3	91.5	29.8	112.54	68.32	S	182	20.2
4	152.4	30	539.12	86.48	S	267	105.2
						Extrap event time 161.8 mus	
#414-2						Estimated wave speed 5.28 mm/mus	
Impact	99.7	38.1					
1	151.8	91.1	747.41	125.92	E	298	142.5
2	91.4	91.3	537.54	114.74	N	265	109.5
3	91.5	29.8	112.54	68.39	S	177	21.5
4	152.4	30	539.12	86.11	S	259	103.5
						155.5	
#414-3						5.12	
Impact	99.1	38.1					
1	151.8	91.1	747.41	126.17	N	414	
2	91.4	91.3	537.54	114.70	N	272	272
3	91.5	29.8	112.54	68.32	S	183	183
4	152.4	30	539.12	86.48	S	270	270
						125.1	
#414-4						3.03	
Impact	99.1	38.1					
1	151.8	91.1	747.41	126.17	N	317	154.2
2	91.4	91.3	537.54	114.70	N	261	98.2
3	91.5	29.8	112.54	68.32	S	188	25.2
4	152.4	30	539.12	86.48	S	270	107.2
						162.8	
						5.03	

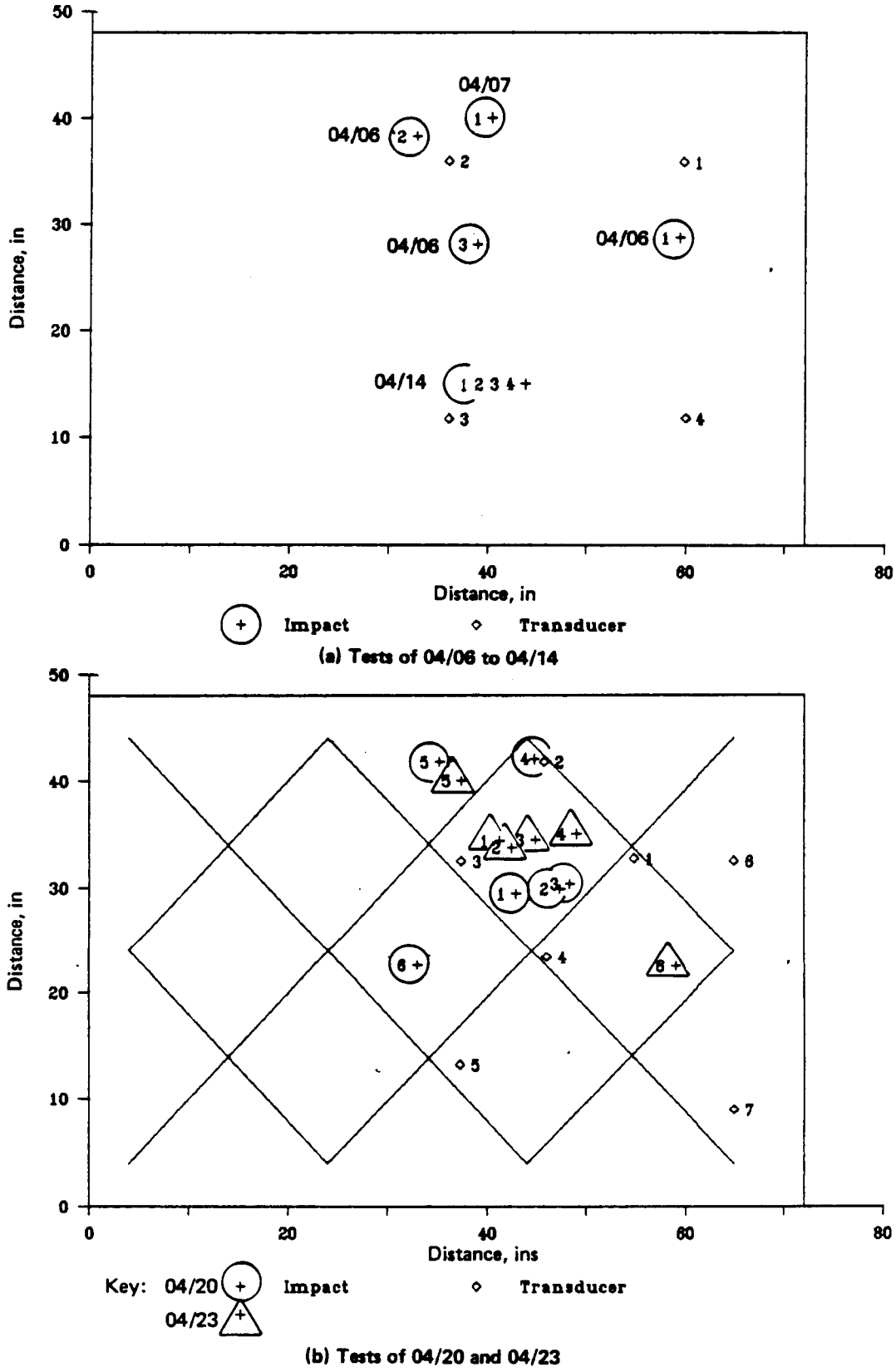

(a) Tests of 04/06 to 04/14

(b) Tests of 04/20 and 04/23

Figure 11. Schematic of Test Configurations

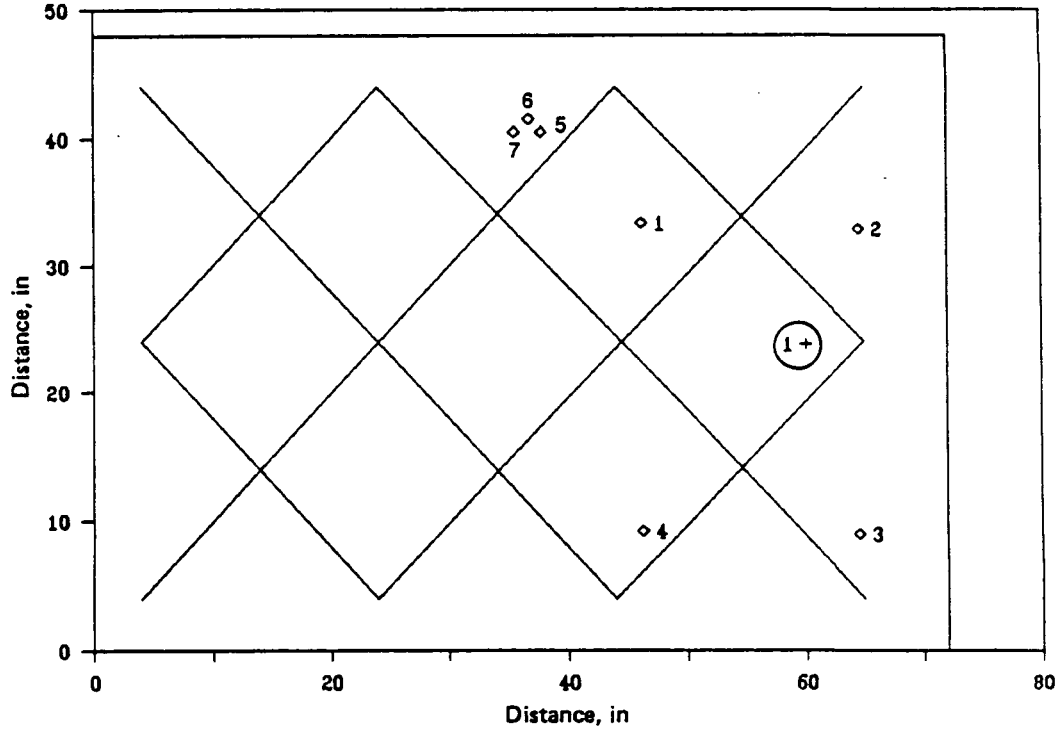

(c) First Test of 05/04

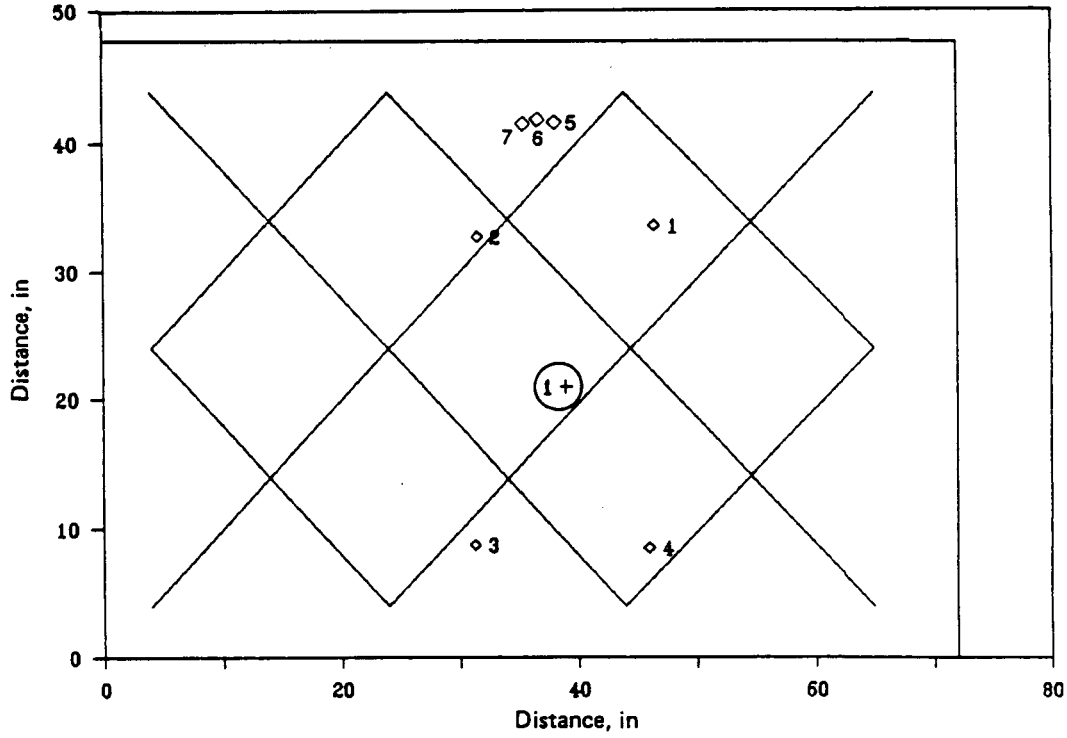

(d) Second Test of 05/04

Figure 11. Schematic of Test Configurations (Continued)

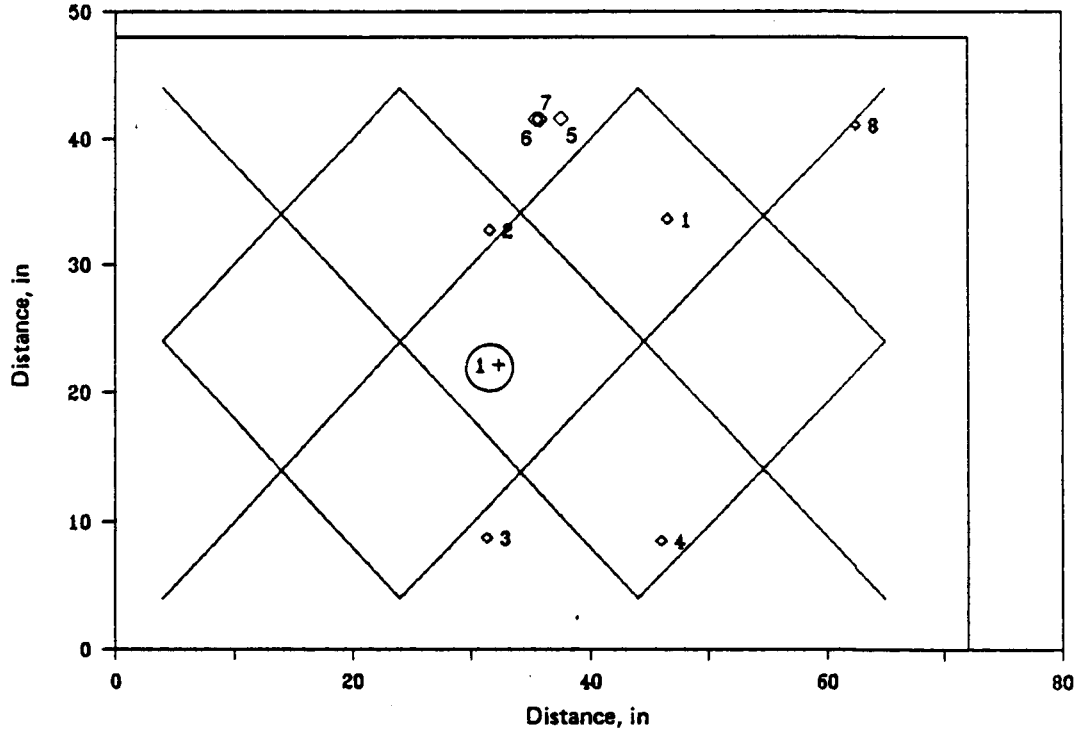

(e) Test of 05/05

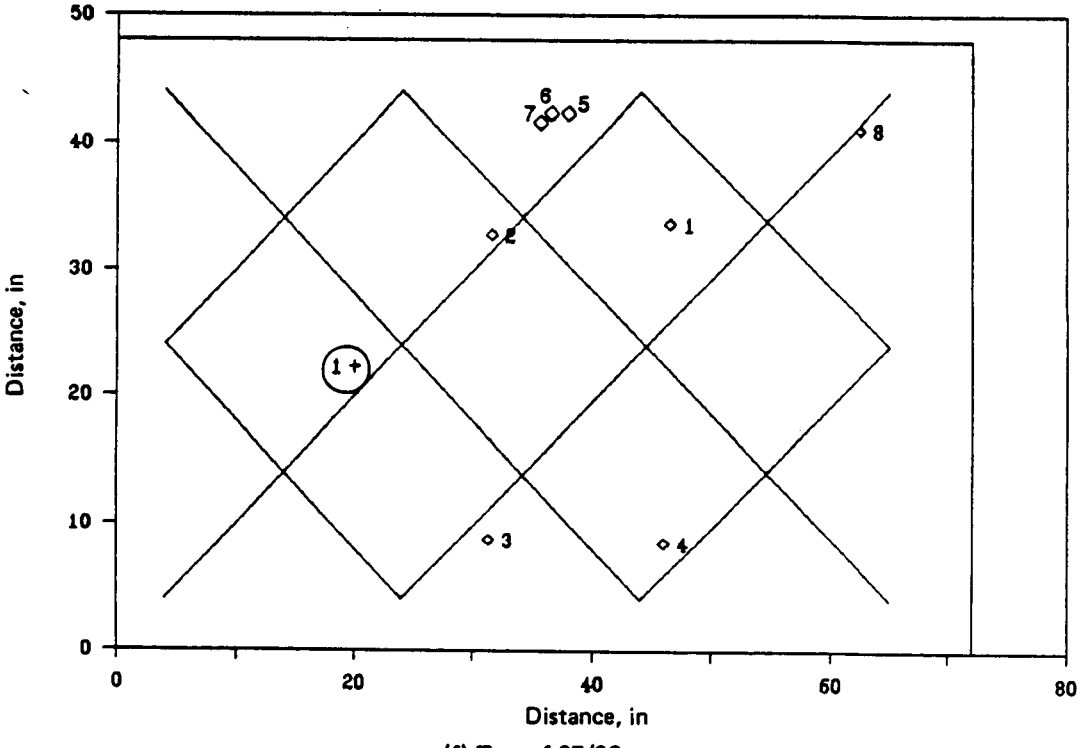

(f) Test of 05/06

Figure 11. Schematic of Test Configurations (Concluded)

The third set of three tests on 03/05 and 03/06 were instrumented for measuring the impactor velocity to determine whether this could be a source of variation from shot to shot. It was found to be quite repeatable as shown in Tables 1, 2, and 3. The waveforms at 125 mm, 178 mm, and 254 mm (5 in, 7 in, and 10 in) (figure A-4) were similar to those of the previous tests, while those at 76 mm (3 in) appeared to be somewhat similar.

Three tests of 03/20 were intended to evaluate the transducer used at 254 mm (10 in) because doubt arose as to whether its response was inverted. The onset of the high frequency perturbation in relation to the low frequency appeared to be inconsistent with that of the other tests. This was subsequently attributed to the arrival of an echo from the edge of the plate at about the same time for all transducers. Two transducers were placed side-by-side at about 305 mm (12 in.). The results (figure A-5) showed only moderate differences between them, but both sensors exhibited waveforms that were less characteristic of dispersive bending than in the previous tests. It is thought that the mass of the two together inhibited bending. It could not be clearly established whether there was a sign reversal.

A preliminary test was made on 03/25 using a multi-channel digitizer to compare the signals from four transducers at one distance. Also, a projectile timing device consisting of two screens of fine wire was placed between the gun barrel and the panel to determine whether the gun performance was repeatable. The transducers were placed next to each other on a line perpendicular to a radius from the impact. The signals (figure A-6) were quite similar to each other in the first 100 microseconds, or so, but became dissimilar after that. These waveforms exhibited little bending dispersion, again probably due to the mass of four transducers close together.

Several tests were made on 3/25, 4/1, 4/2, 4/6, and 4/7 using a configuration with four transducers placed at 45 deg. intervals around an arc of 305 mm (12 in) radius centered on the impact point. An ultrasonic transducer was used at the impact point to provide a trigger in the first two tests (though its signal was not recorded) but it was not installed for the other tests, so triggering was taken from the other transducers. The data are shown in figures A-7 to A-13. The first two of these showed that transducer #4 was still suspect, as its signals were low by a factor of 10. Indeed it was found to contain a faulty connector. Problems were encountered with the projectile timing device and were resolved during this sequence of tests. The transducer closest to the impact (no. 2) exhibited unexplained high spikes at an early time in the last three tests.

Four tests were then conducted on 04/14 to obtain data similar to those of the original IR&D effort, but now using multi-channel recording of four transducers arranged in a 305 mm (12 in) square, so that all data were simultaneous. The projectile was a 4.0 mm (5/32 in) dia. nylon sphere. The data given in figures A-14 and A-15 show lower signals than for the previous tests with the copper-clad steel BB, but apparently with a higher content of high frequency.

Six tests were made on 4/20. Additional transducers were used to investigate alternatives to the acoustic emission sensors. These included a low frequency bending sensor ("Sondicator") based on a 25 KHz crystal, and a thin piezoelectric film ("Kynar"). Data are shown in figures A-16 to A-21.

Tests on the waffle panel were begun with six low velocity (BB) shots on 4/23. The sensors were arrayed within the waffle squares to provide transmission directly within a panel as well as across the stiffener ribs. Data are given in figures A- 22 to A-27. The signals varied widely among the transducers, though all showed some of the expected features. Many included high spikes which offset the automatic scaling, but the signal appears otherwise normal. The problem is thought to lie in the digitizer which uses an interpolation procedure to fill in data between sampling times.

High velocity tests on the waffle panel were conducted on 5/4, 5/5 and 5/6 using a BAC two-stage powder gun with cylindrical aluminum pellets as illustrated in Figure 12. The installation of the shield plate and the multi-layer insulation materials is illustrated in Figure 13. These tests were designed to conform to predictions of penetration made in BAC IR&D studies (reference 5) as represented by the graph of Figure 14, showing a penetration threshold for projectile diameter and velocity. As indicated, test conditions were selected to provide some penetrating and some non-penetrating shots: one with 6.4 mm (1/4 in) dia and 6.4 mm (1/4 in) long pellet at 3 mm/microsecond onto a shield of 0.063 in aluminum; the same with 20 layers of insulation on the panel; the same at 1.5 mm/microsecond; and one with a 3.2 mm (1/8 in) dia. and 3.2 mm (1/8 in) long pellet at 3 mm/microsecond.

The first test was unsuccessful because the trigger was incorrectly timed. Further, no penetration occurred when it was expected suggesting that the fault lay in the gun firing. The remaining four shots were satisfactory. Signals for these shots are shown in figure A-28 to A-31. Photographs of the impact areas are shown in Figure 10.

Any possible effects of air-borne shock from the powder-gun were mitigated by the shield plate. Induced motions would have to propagate along the shield plate, down the support screws, and along the panel to the sensors. The propagation would attenuate and delay the motions considerably so that they would not interfere with the motions from penetration.

Two stage powder gun and waffle panel with shield attached.

Acoustic emission transducers attached to the panel on the smooth, concave side.

Figure 12. Waffle Panel Impact Test Setup for Impact Detection/Location System

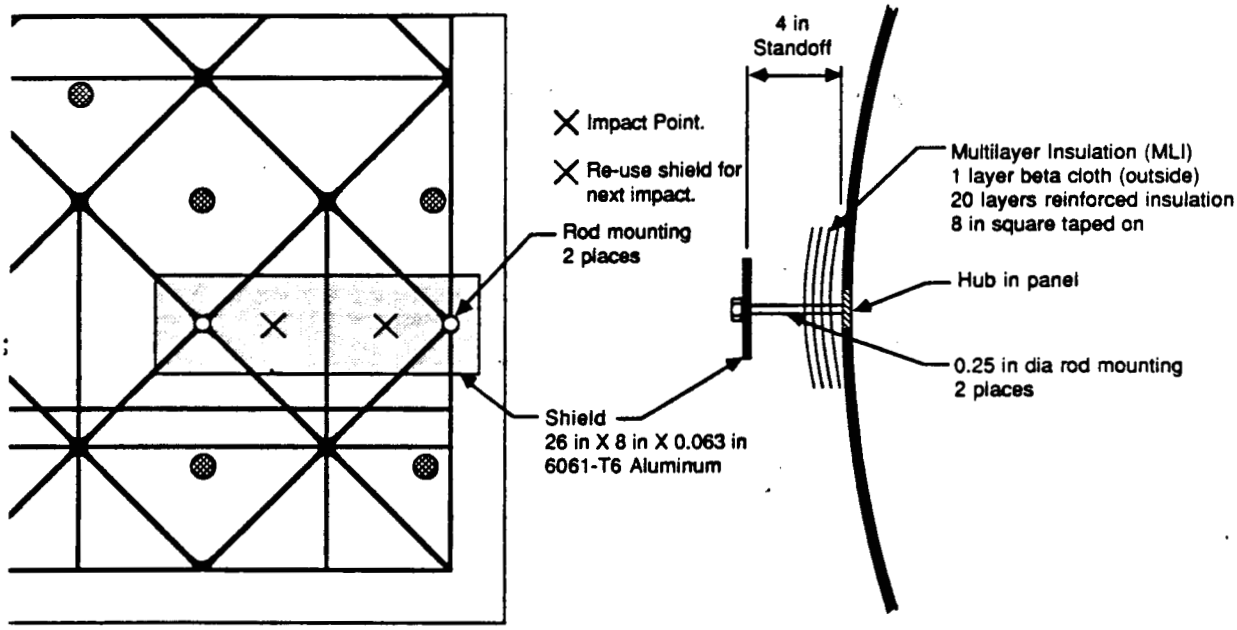

Figure 13. Installation of Shield and Insulation on Test Panel

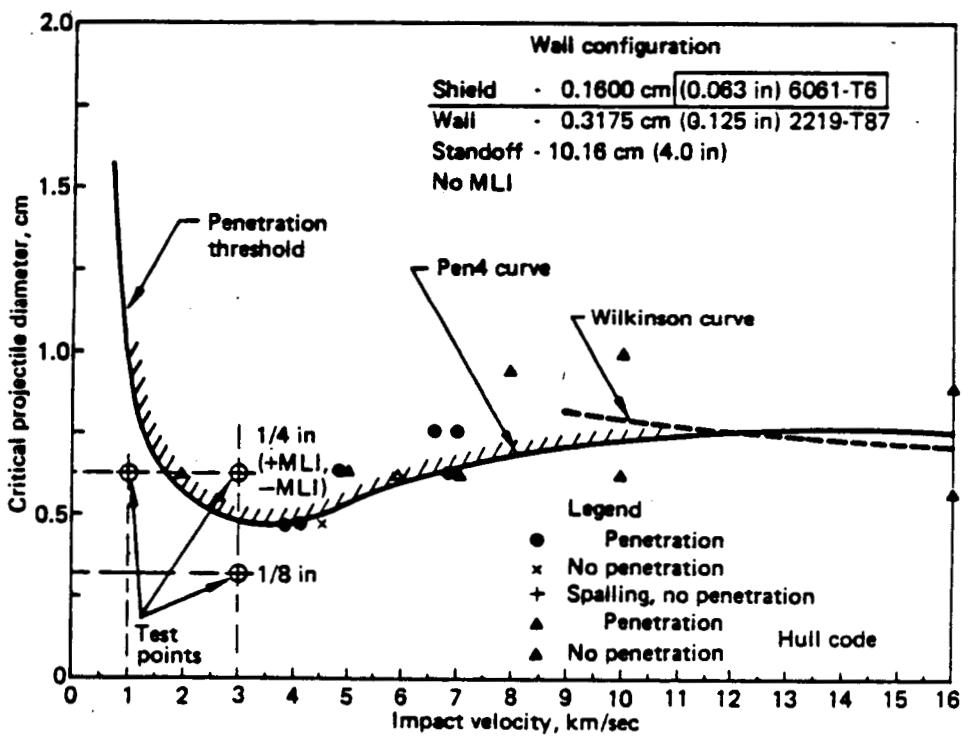

Figure 14. Selected Test Points Versus Pretest Predictions

This page left blank intentionally

4.0 THEORY

4.1 Plate Response

The dynamic response of a plate takes the form of in-plane and lateral motions. These generally occur in a wide range of modes, some propagating as waves with frequency-dependent wavespeeds and others as stationary oscillations which do not propagate. Up to moderate frequencies the in-plane response propagates by simple waves having a constant wavespeed known as the plate speed. This is typically slightly less than the dilatational (longitudinal) speed for the material, because the plane stress state caused by lateral relief of stress at the faces of the plate is less stiff than the plane strain state of a plane wave. The transverse response behaves like ordinary bending at low frequency with a diffusion-like character having an apparent[1] speed that varies with the square-root of frequency. At high frequency it behaves like independent Rayleigh surface waves on the two faces of the plate. The relative magnitudes of these various motions are dependent on the loading and the boundary conditions.

4.2 The General Solution

Solutions of the differential equations for in-plane motions, u(x,z,t) and lateral motions, w(x,z,t) of a thin plate are found (reference 6a) in the propagating exponential forms

$$u = U(z)e^{ik(x-ct)}$$

and

$$w = W(z)e^{ik(x-ct)}$$

These propagate at the wavespeed c and oscillate in time at a frequency $\omega = kc$ with spatial wavenumber k. The thickness variations U(z) and W(z) are determined by two thickness scale factors

$$q = k(1-c^2/c_1^2)^{1/2}$$

and

$$s = k(1-c^2/c_2^2)^{1/2}$$

---

[1] A motion with such wave speed dependence is not a true wave because the speed of low frequencies approaches zero, and no wave packets of similar frequency can group together as all frequencies have different speed.

with c_1 and c_2 being the longitudinal and shear speeds of the material, respectively.

These quantities are related by the two equations for:

1) in-plane motion:

$$\tanh(sh)/\tanh(qh) = 4sqk^2/(k^2+s^2)$$

and

2) transverse motion:

$$\tanh(qh)/\tanh(sh) = 4sqk^2/(k^2+s^2)$$

These are referred to as the dispersion relationships which determine the wavespeed c through q and s as functions of k and thus of ω. Graphical representations are available as illustrated in figure 15 (from reference 6a).

4.3 In-Plane Motions

Up to moderate frequencies, the in-plane motions are governed by the common wave equations, in which the wavespeed is the plate velocity

$$c_{pl} = \{E/\rho\,(1 - \upsilon^2)\}^{1/2} = \{(1 - 2\upsilon)^{1/2}/(1 - \upsilon)\}\, c_L$$

where E is Young's modulus, ρ is the density, υ is Poisson's ratio, and c_L is the longitudinal wavespeed for plane waves in unbounded media. For υ=1/3, typical of aluminum, the factor is 0.904. Since c_L in aluminum is about 6.3 mm/microsecond, then c_{pl} = 5.7 mm/microsecond.

At high frequencies where motions through the thickness become constrained by lateral inertia effects, the waves propagate slower, at the Rayleigh velocity, which for aluminum is c_R = 3.1 mm/microsecond.

From a point source, these waves propagate cylindrically, decaying, because of increased area, as the logarithm of distance. Typically this reduces amplitude to negligible levels within 20 to 100 source diameters, about 120 to 600 mm (5 to 25 in) for a 6 mm (1/4 in) impactor.

4.4 Lateral (Bending) Motions

A simplified analysis based on the Timoshenko Beam Theory (reference 6b) leads to the approximate but explicit dispersion relationship:

$$k = (\omega/\sqrt{2}c_{pl})\{1 + a \pm [(1-a)^2 + (2c_{pl}/r\,\omega)^2]^{1/2}\}^{1/2}$$

where a is the ratio of Young's modulus to a factored shear modulus, E/fG, (conveniently taken to

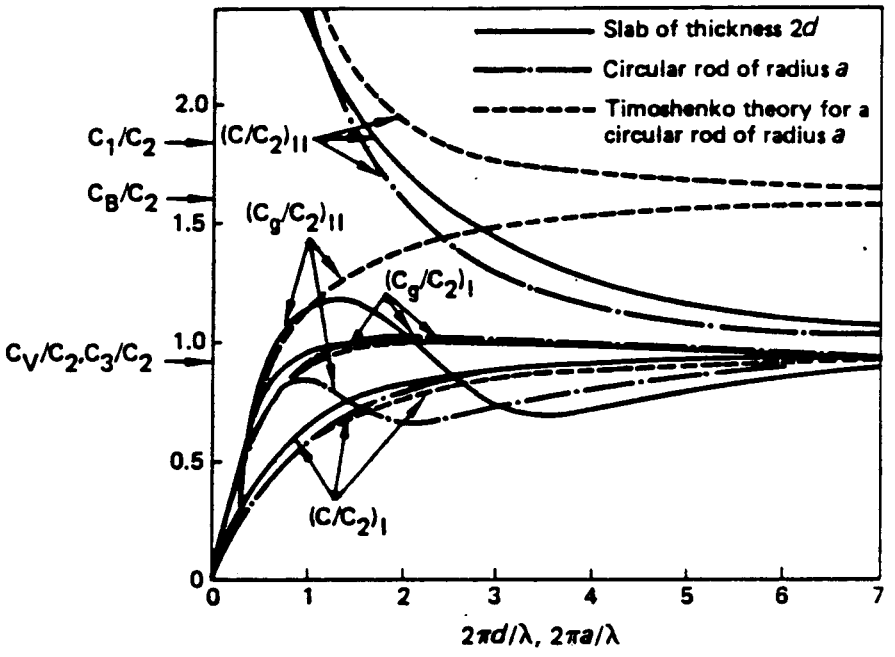

Dispersion curves for the Timoshenko theory and for the two lowest transverse modes in a slab and in a circular rod (Poisson's ratio $\nu = 0.29$)

Figure 15. Calculated Dispersion Curves for a Plate

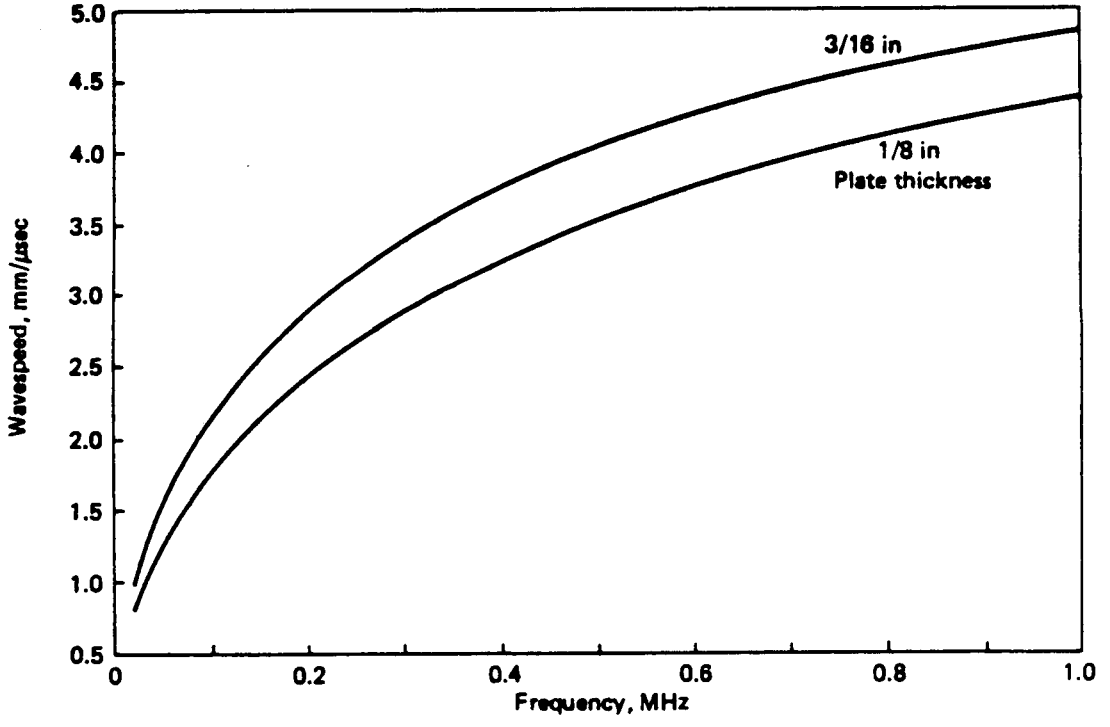

Figure 16. Calculated Dispersion Curves for Bending of Aluminum Plates of Two Thicknesses

be the square root of the ratio of longitudinal to Rayleigh wavespeeds), and r is the radius of gyration of the plate, $r = h/\sqrt{12}$ with h the thickness. This has two modes, one for the positive and one for the negative radical sign. At low frequencies, the positive mode gives imaginary wavenumbers, so that these modes do not propagate. Above a certain cut-off frequency, however the wavenumbers are real and a high speed propagation develops.

From this formula the wavespeed $c = \omega/k$ can be written as

$$c = \sqrt{2}c_{pl}/\{1 + (c_{pl}/c_R)^2 \pm \{[1 - (c_{pl}/c_R)^2]^2 + 4(c_{pl}/c_b)^4\}^{1/2}\}^{1/2}$$

where c_b is the bending speed $(Eh^3/12\,\mu)^{1/4}\,\omega^{1/2}$, and $\mu = \rho b$ is the plate areal mass density. The coefficient in this formula is equivalent to the vibrating beam stiffness coefficient (EI/μ). The dispersion formula thus has three parameters, c_{pl}, c_R (or their ratio which depends only on Poisson's ratio), and h.

At low frequencies, the negative mode reduces to $c = c_b$, which is 0 at 0 frequency, and at high frequencies to $c = c_R$. The positive mode is usually of small magnitude and so is not considered further here, though it should not be dismissed.

A graph showing the dispersive wavespeed for 3.2 mm (1/8 in) and 4.8 mm (3/16 in) thick aluminum plates is given in Figure 16.

4.5 Transient Motions

The motions controlled by these dispersion relations can be expressed by Fourier Integrals as superpositions of all frequency components. Thus, the response at the impact point can be written as

$$u(t) = \int U(\omega) \exp(i\,\omega t) d\omega$$

where $U(\omega)$ is the transform of the motion, a complex variable, and can be written as

$$U(\omega) = A(\omega) \exp[i\theta_O(\omega)]$$

A is the amplitude of each frequency component, and θ_O is the phase. For an impulsive source, all components start as maxima at the same phase $\pi/2$. When these components propagate, each at a different speed, the signal is given by the Fourier Integral with shifted time $t' = t - x/c(\omega)$:

$$u(x,t) = \int U(\omega) \exp[i\ \omega(t-x/c)]d\omega$$

so that the apparent phase of the transform of u(x,t) is

$$\theta(\omega) = \pi/2 - x/c(\omega)$$

Since the time of impact is not generally known, an unknown time-shift through t_o occurs in the data, resulting in a spectral change. The measured waveform then has the spectral phase

$$\theta_m = \theta + \omega t_o = \pi/2 - \omega x/c + \omega t_o$$

This formula shows that the phase spectrum contains the distance and time shift explicitly. Since the frequency dependence of the terms is known, it should be possible to use a regression analysis on measured spectra to obtain these. However, the phase varies as $\omega^{1/2}$ (since the speed c varies as $\omega^{1/2}$ and this leads to an infinite slope at zero frequency. Thus, the phase spectrum changes fast near zero. For a numerically-derived spectrum at discrete frequencies, the change between each point can be larger than 2π.

Numerical analysis can only evaluate the principal phase between say π and $-\pi$ so that uncertainty arises at the low frequency end of the spectrum.

4.6 Determining Location

Measurements of motion at several places provides data on time of propagation at a known speed from the unknown impact point to several known places, but with an unknown time shift common to all sensors. There are three unknowns: the time of impact, and the two coordinates of the impact. Two methods are available for determining the unknowns: a minimization of the squared error, and the intersection of difference hyperbolae. The former is useful for many sensors, and the latter for few.

a.) Minimized Error Method

For a known point (x,y) the travel time relative to an arbitrary time with the unknown shift t_o is t. For a wave travelling with a speed c from the impact point (x_o,y_o), these are related by

$$r = \{(x-x_o)^2+(y-y_o)^2\}^{1/2} = c(t+t_o)$$

Any error in this determination can be written as

$$e = r - c(t+t_o)$$

and a least squares definition of best fit defined as

$$\Sigma e^2 = \text{Min}$$

The variables in this minimization are the unknown impact position (x_o,y_o) and the time shift t_o. The minimization leads, by differentiation, to the equations

$$\Sigma e(\partial e/\partial x_o) = \Sigma e(\partial e/\partial y_o) = \Sigma e(\partial e/\partial t_o) = 0$$

which can be written as the following implicit equations

$$x_o = \{\Sigma ex/r\}/\{\Sigma e/r\}$$

$$y_o = \{\Sigma ey/r\}/\{\Sigma e/r\}$$

$$t_o = \Sigma r/c - \Sigma t$$

An iteration scheme based on these equations serves to determine x_o, y_o, and t_o from several waveforms.

(b) Difference Hyperbola Method

Since the unknown impact time is common to all sensors, it can be eliminated by considering the differences in time of arrivals between two sensors. Consider the time of arrival at sensors i and j:

$$\Delta_{ij} = t_i - t_j$$

The locus of all points for which the difference in distances to the two sensors is the hyperbola:

$$ax^2 + by^2 + cxy + dx + ey + f = 0$$

with

$$a = (x_i - x_j)^2 - \Delta_{ij}^2$$

$$b = (y_i - y_j)^2 - \Delta_{ij}^2$$

$$c = (x_i - x_j)(y_i - y_j)$$

$$d = (x_i - x_j)(x_i^2 - x_j^2 + y_i^2 - y_j^2) - \Delta_{ij}^2 (x_i - x_j)$$

$$e = (y_i - y_j)(x_i^2 - x_j^2 + y_i^2 - y_j^2) - \Delta_{ij}^2 (y_i - y_j)$$

$$f = (x_i^2 - x_j^2 + y_i^2 - y_j^2 - \Delta_{ij}^2)^2 - \Delta_{ij}^2 (x_i^2 - y_i^2)$$

Two such hyperbolae, constructed from two pairs of sensors, will define a unique intersection point from which the distances to the four sensors satisfy the observed differences. It is thus a matter of solving simultaneously two such hyperbolic equations.

This page left blank intentionally

5.0 TEST RESULTS

The recorded waveforms have been analyzed to evaluate four factors: 1) the accuracy of defining time-of-arrival of the signals; 2) the accuracy of impact position estimates; 3) the relationship of the Fourier transform to impact characteristics; and 4) feature analysis as a means of determing impact characteristics.

5.1 Time Of Arrival (TOA)

The onset of motion (or time-of-arrival (TOA), or first break in the signal) is needed to estimate wave travel time for determining impact position and for isolating the various response pulses for Fourier analysis. It is defined as the time at which the signal exceeds a threshold. The practical problem is to distinguish between signal, early or late, and noise, since the first motion is small and larger motions represent modes at varying wavespeeds. The fastest waves are the in-plane motions which decay rapidly with distance, followed by the high frequency Rayleigh waves. Trailing these at ever lower speeds are the bending waves, which can be the largest.

A typical waveform (from the sensor at 254 mm (10 in), file IMP2.DAT of 1/21) is shown, together with early details on enlarged time scales, in Figure 17. The earliest pulse train, amplified at the lower left of the figure, appears to have a slight inverse dispersion, with frequency decreasing along the pulse from a period of about 3.5 microsec for a half wave (i.e. at a frequency of 0.14 MHz) to about 1.5 microsec (0.3 MHz). The large later pulse train shown at the lower right is strongly dispersive with the frequency increasing steadily by a factor of ten or so from 3 microsec per half wave (0.16 MHZ) to about 30 microsec (16 KHZ) after about 0.3 milliseconds. The clipping of this waveform does not affect these features. This behavior, which represents slower propagation as frequency decreases is characteristic of bending motions. The increasing separation of the early and late pulses with distance is illustrated in Figure 18 for traces from the tests of 02/10.

Details of four different waveforms all at one distance (sensors 1 to 4 from 0325_1.AE) are shown on an exaggerated time scale in Figure 19 displaying measurement repeatability to within a few microseconds. For wavespeeds up to 6 mm/microsecond, however, this represents a propagation distance uncertainty of up to 20 mm.

Waveforms from all tests for which signals were recorded from two sensors in line with the impact have been analyzed for arrival time using a sequence of thresholds. For each waveform, the baseline of the recordings was found for the first 100 points, and then the data were shifted to this baseline and smoothed by forming moving averages over 7 points. The time of first occurrence of a signal above each of five levels in a doubling sequence of thresholds were then found.

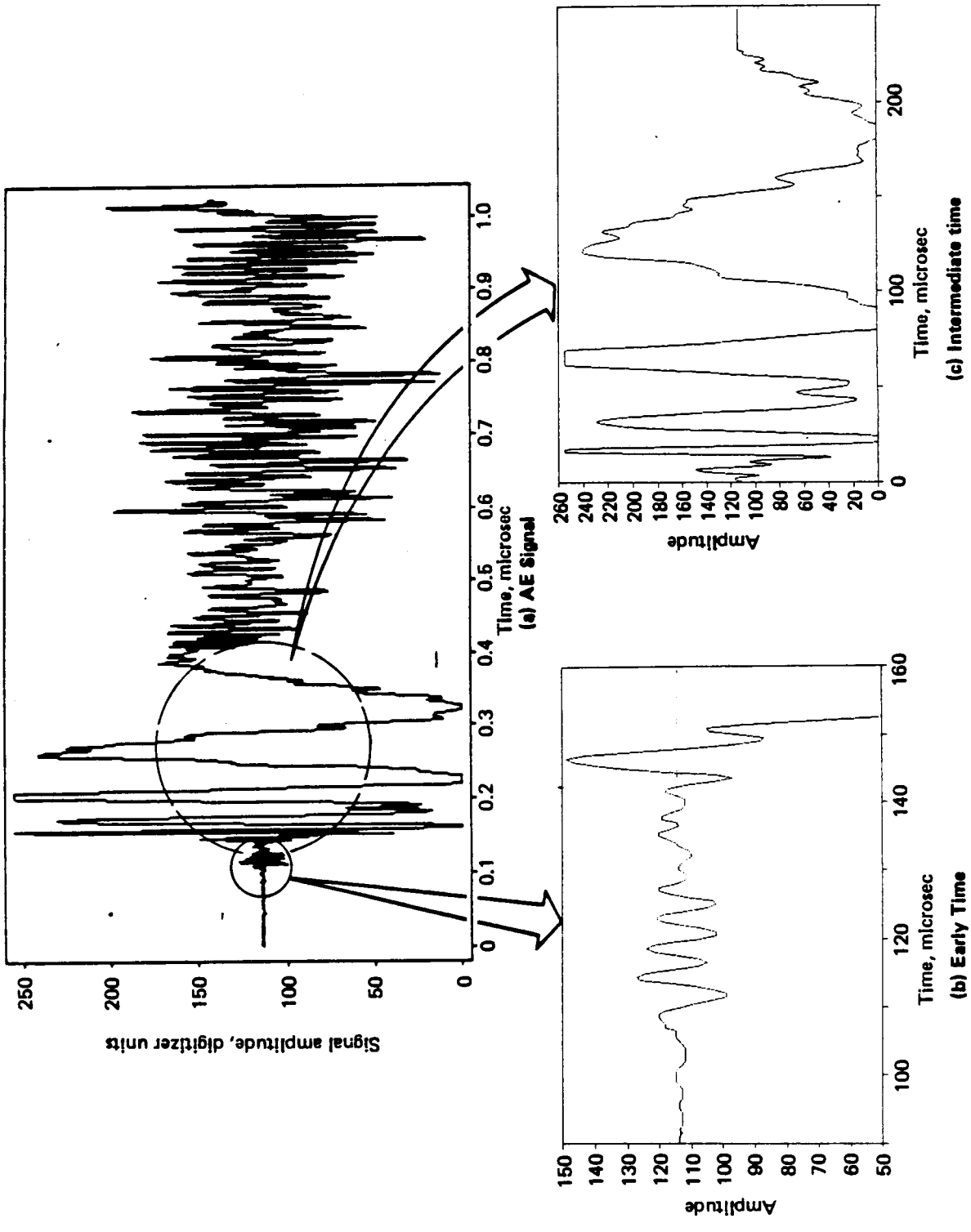

Figure 17. Details of a Typical Recorded Waveform

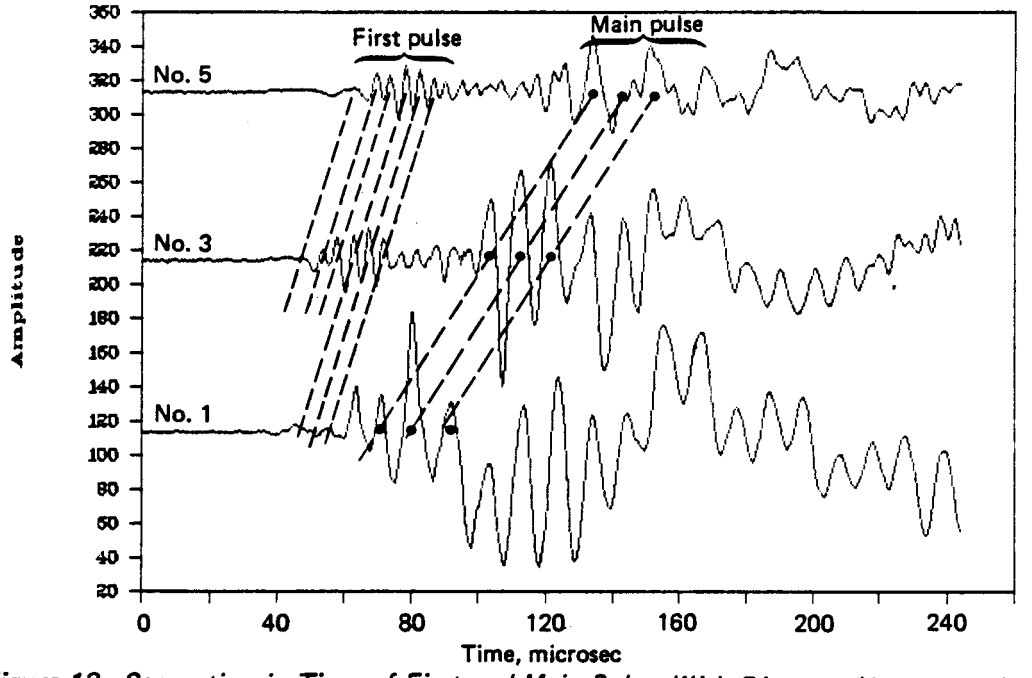

Figure 18. Separation in Time of First and Main Pulses With Distance (Test of 02/10)

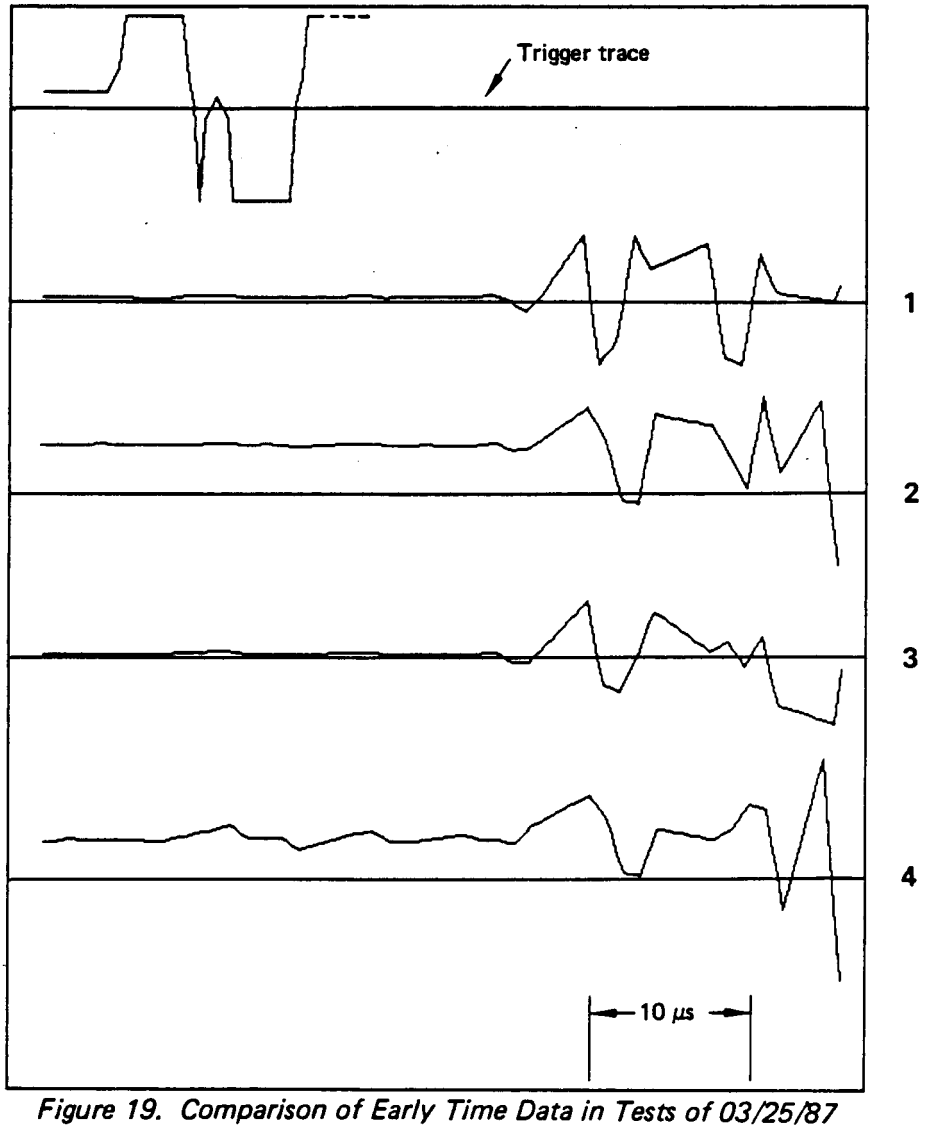

Figure 19. Comparison of Early Time Data in Tests of 03/25/87

The increments of distance and time between pairs of waveforms for two in-line sensors are given in Table 4a of Sect 3 above for the six tests of 0325-1 and -2 (excluding the waveforms from sensor #4 which had low signals) are plotted against threshold level in Figure 20. They show that for a threshold below about 5 volts the arrival time increment is between 60 and 65 microseconds, implying a wavespeed of 4.7 to 5.1 mm/microsecond, whereas above 7 volts, the times are between 105 and 120, for speeds of 2.5 to 2.9 mm/microsecond.

For an automated system and for a more precise measure, the TOA must be determined from some threshold criterion independent of sensor calibration or characteristics. Several such methods were tested, and one based on signal-to-noise ratio as described below was selected.

An algorithm was set up to the determine the point at which the signal exceeds the noise floor. The noise baseline was defined by a running sequence of least-squares fits to the transducer readings for times ranging from the start of recording and extending, in turn, to each subsequent measured data point.

Each such fit was extrapolated to the next data point at which the signal was defined as the magnitude of the difference between the measured value and the baseline extrapolation. The noise level was taken to be the standard deviation of the fit. The signal-to-noise ratio (SNR) was then used to determine the arrival of the signal as the point where it exceeded a threshold.

An example of this determination of the SNR for four records in the test of 04/01 is shown in Figure 21. The sensors were all on an arc at the same distance from the impact. The figure shows the coincidence of the first arrivals at about 205 microsecs, with an SNR of about 5, and the main pulses at about 255 microsecs, with SNR exceeding 30. For most cases a value of 5 for the SNR was found to be sensitive to the first arrival and 10 for the main pulse. The method does not work for low-level data from large distances where the data was essentially noise, as could be expected.

TOA values were determined for the first and the main pulse from each sensor in each test from 04/06 to 04/14 as listed in Table 4. Using the known impact positions distance-time regression fits were made for the groups of four in each test, to allow the event time of that test to be determined as the intercept time. The data for all sensors from all tests were then corrected to these zero-times, and plotted together in one graph as in Figure 22. The data fall closely on one line, whose slope (by a regression fit) is 5.26 mm/microsec for the measured speed of the first wave.

5.2 Position Location Estimates

Using an iterative algorithm that minimizes the squared error in distance-time estimates, the time-of-arrival of 04/06 and 04/07 have been analyzed to find impact positions. The results are plotted in Figure 23. Accuracy of location is within about 75 mm (3 in).

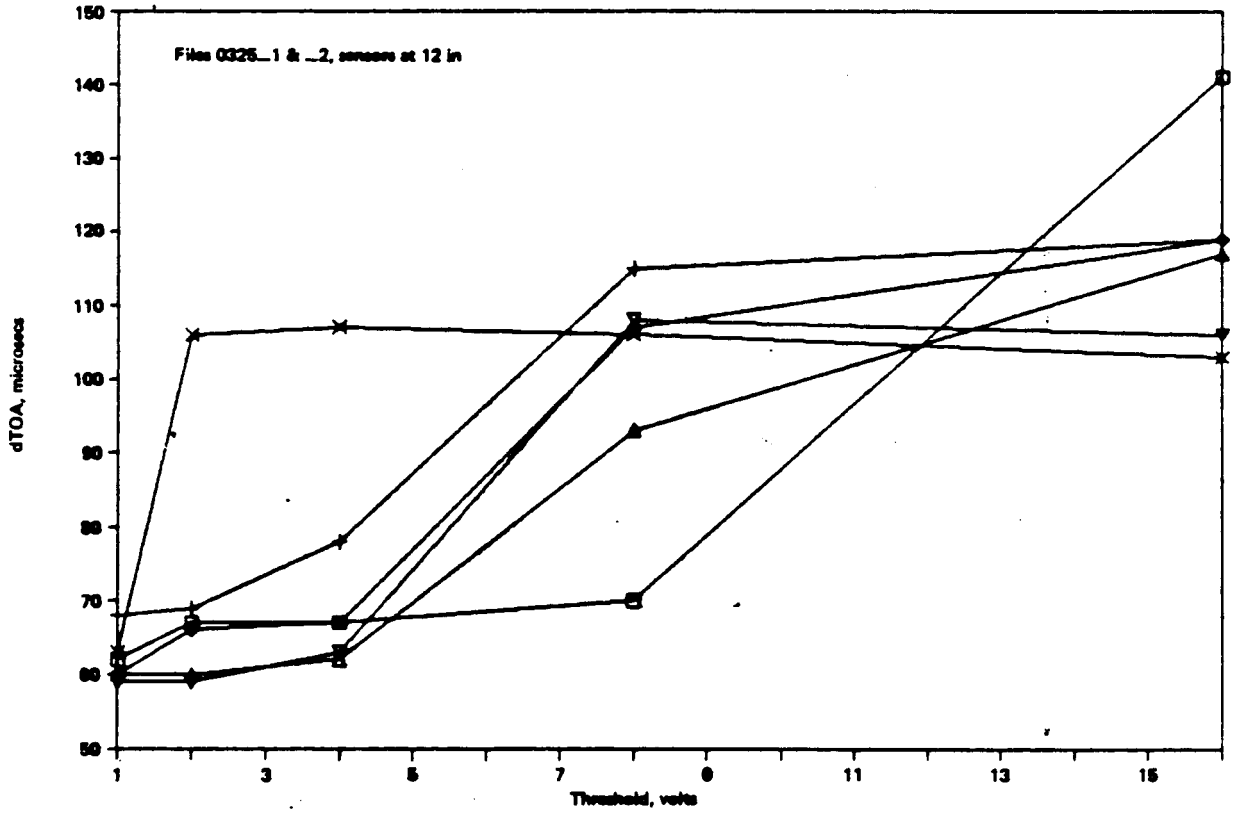

Figure 20. Differential Time-of-Arrival Data

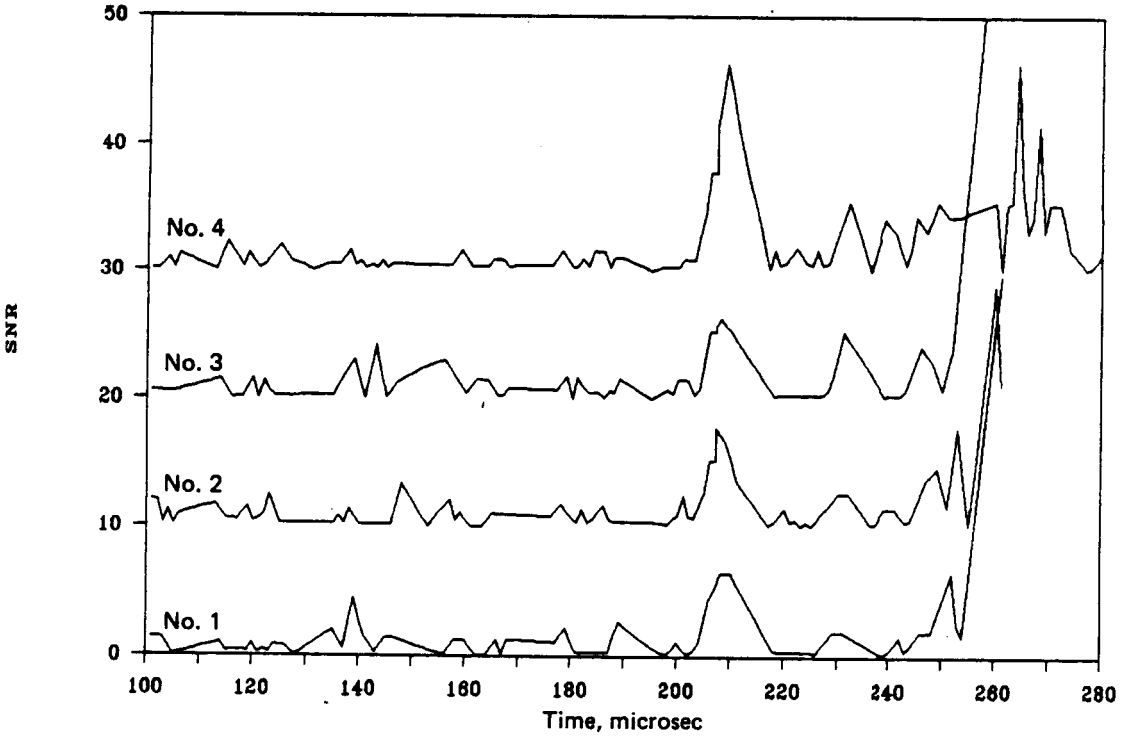

Figure 21. Signal-to-Noise Ratio, (Sensors 1 to 4 of 04/01)

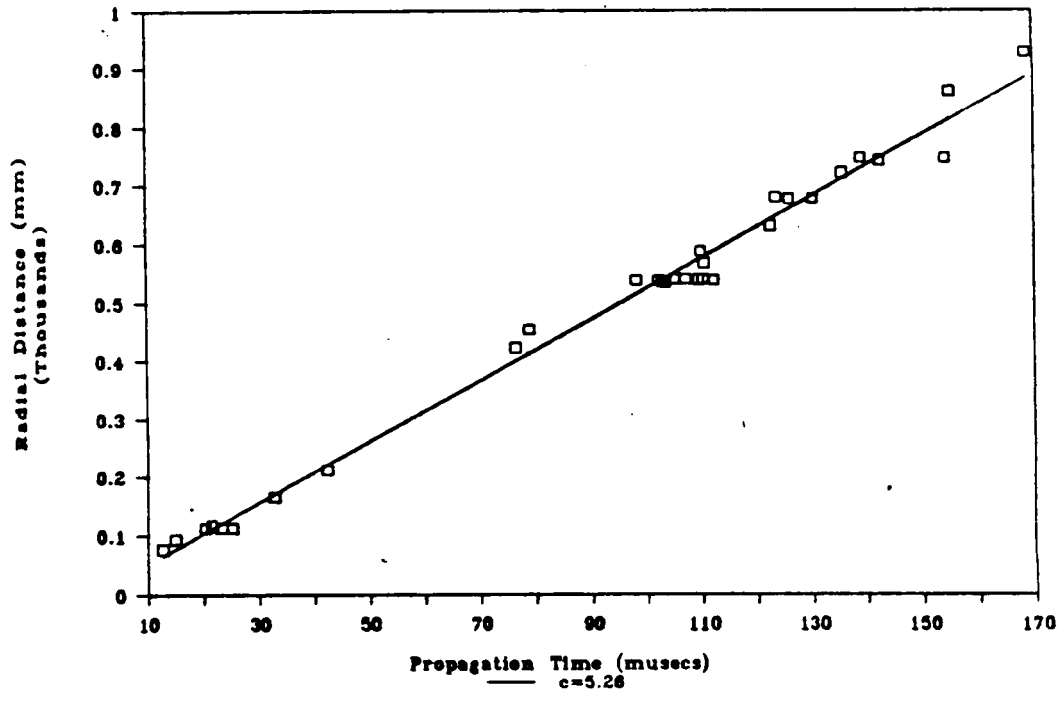

Figure 22. Time of Arrival Data (Corrected for Event Time From Fits)

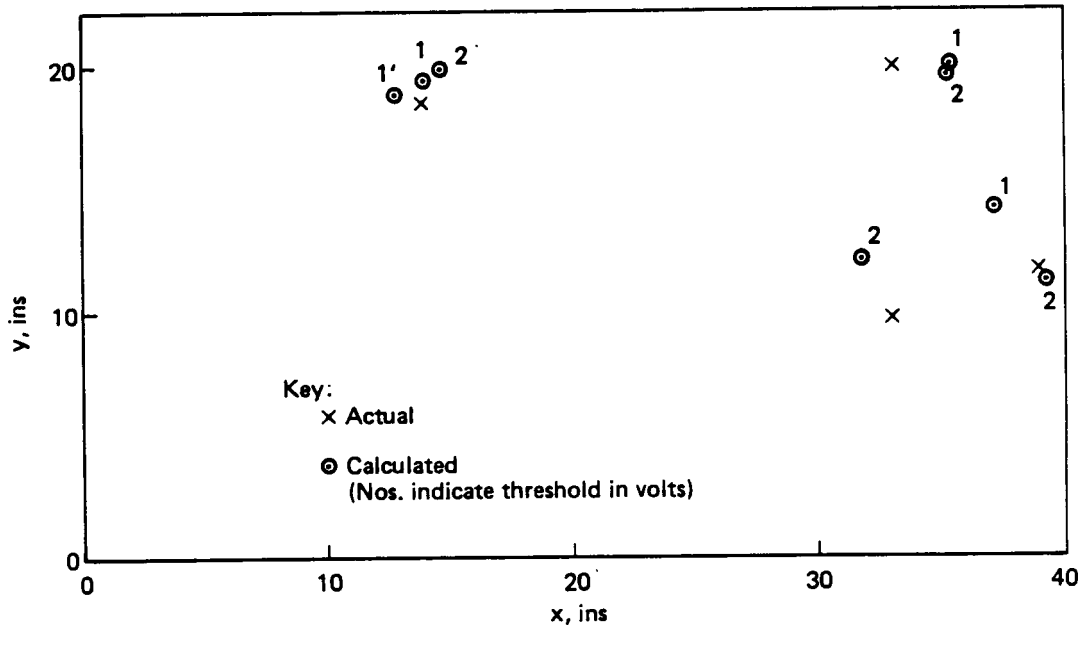

Figure 23. Comparison of Calculated and Actual Impact Positions

5.3 Fourier Spectral Analysis

Spectral analysis was made by two methods: the simple zero-crossings technique and the Fast Fourier Transform (FFT) technique. The zero crossing method provides a simple evaluation of the phase spectrum from which the requirements for the FFT can be deduced.

5.3.1 Zero-Crossing Analysis

The recording IMP2 of 1/21 was analyzed by first establishing a baseline and then finding times at which the signal crossed this baseline. These times were used to calculate frequencies and group velocities.

Between each pair of zero-crossings, the signal pulse can be approximated by a sine-wave whose half period is the difference of the times, so that

$$t_{p,i} = 2(t_{x,i} - t_{x,i-1})$$

where $t_{p,i}$ is the period of the signal at the i-th pair

$t_{x,i}$ is the time of the i-th zero crossing.

The frequency is then

$$f_i = 1/2(t_{x,i} - t_{x,i-1})$$

Such a pulse is formed by the coincidence at that time and place of all waves near this frequency having the same phase. That is, the variation of phase with frequency is zero, which is the definition of a group whose velocity is the group velocity, $c_g = d\omega/d\kappa$ where ω is the angular frequency and k is the wave number, used in the solution form exp $i(kx-\omega\tau)$. The pulse is centered on the transducer at a known distance x at the time $1/2(t_{x,i} + t_{x,i-1})$ so that the group velocity is

$$c_g = 2x/(t_{x,i} + t_{x,i-1})$$

Thus, determination of the zero-crossing times allows derivation of the group velocity as a function of frequency. The wave number k is then obtained by the integral

$$k = \int d\omega / c_g$$

and the phase distribution is then

$$\theta = kx - \omega t$$

The phase velocity is $c = \omega/k$.

The phase spectrum calculated by this method for the main pulse of IMP2 is shown in Fig. 24a. The phase velocity is shown in Fig. 24b; where it is compared to the theoretical dispersion curve. There is close agreement. This method is not satisfactory for noisy data, however.

The phase spectrum shows that the main pulse is a bending motion and that its frequency range is from about 0.01 MHz to 0.2 MHz. The spectrum of the first pulse spans from about 0.1 to 0.5 MHz.

5.3.2 Fast Fourier Transform (FFT)

To calculate the FFT of a signal it is necessary to select the data sampling period dt and the duration of the signal tmax. These are determined by the maximum frequency and frequency step in the FFT by the formulae (Ref. 7)

$$dt = 1/f_{max}\ ,\ t_{max} = 1/df = 1/f_{min}$$

For the frequency ranges given above, these are

for the main pulse: $dt = 5$ microsec $t_{max} = 100$ microsec
for the first pulse: $dt = 2$ microsec $t_{max} = 10$ microsec

The frequency ranges, and hence the times, are bounds only, and wider ranges may be more practical.

The superposition of multiple modes is compounded by the arrival of echoes off the edges of the test panel. These echoes have a similar magnitude spectrum, but with a time shifted phase. To minimize this problem, the time of arrival of the first echo (TFE) was determined, and all FFT's were made with data for times shorter than TFE.

To determine the TFE, impact-to-sensor distances on echo paths represented by oblique distances to the nearest edge, were calculated and are given in Table 4 above. A wavespeed of 5.2 mm/microsec was then used to determine the echo time of the first pulse.

The data are further prepared for the FFT algorithm by smoothing, by applying a triangular-weighted moving average to the time series data and then detrending by a regression fit. This re-

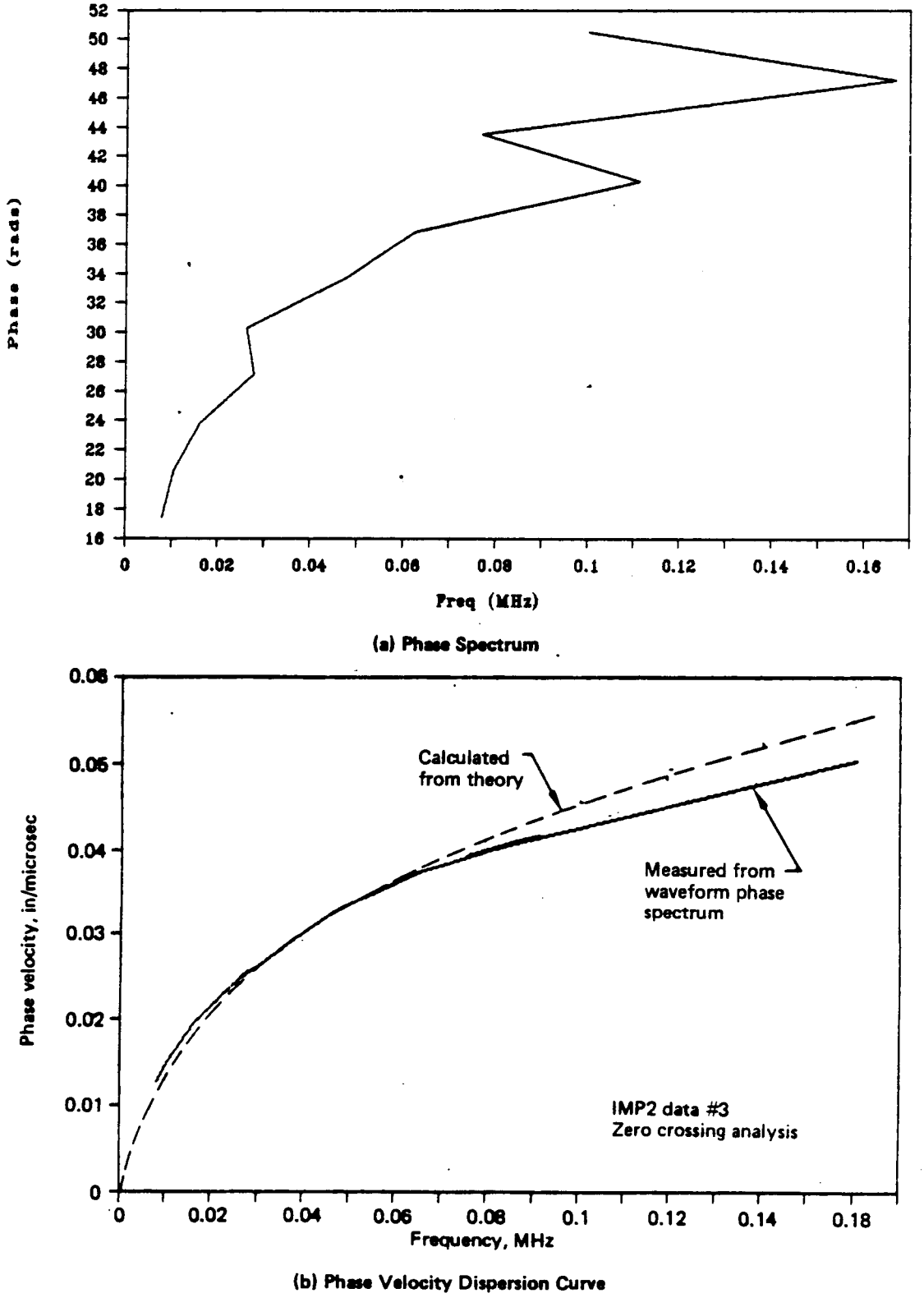

Figure 24. Phase and Phase Velocity by Zero-Crossing Analysis

moves the static and very low frequency components of the spectrum which arise from drift and not from the signal.

The magnitude and cumulative phase spectra derived from FFT's of the first and main pulses of IMP2 are shown in Figure 25 and 26. The magnitude spectrum of the first pulse peaks at an angular frequency of about 0.7 rads/microsec i.e. at a frequency of about 0.1 MHz, lower than 0.3 given by the zero crossing analysis. The main pulse peaks at about 0.1 rads/microsec, or 0.02 MHz, in general agreement with the zero-crossing result. The phase spectra of the two are lower by a factor of two and four respectively than that of the zero crossing analysis, and are reversed. Note that there is a difference in scales by a factor of 2*pi between frequency and angular frequency in Figures 24 and 26. Since the zero-crossing result was shown above to correspond to the theory, the cause of the discrepancy lies in either of two problems: the calculation of phase from the real and imaginary parts of the FFT; or the phase shift in the FFT caused by the uncertain time origin.

The analysis of the phase spectrum uses an arc-tangent algorithm to derive the principal value of phase (between -pi and +pi) from the calculated real and imaginary parts of the FFT. This principal value phase, as illustrated by curves for sensor No. 4 of Test 03/06 in Figure 27(a) is discontinuous, taking occasional jumps by about 2*pi. An algorithm is appended to remove such jumps, converting the phase into a continuous curve as in Fig. 27(b). The accuracy of the algorithm rests on a criterion for defining the jumps. The simplest and most effective sets a threshold on the difference in two adjacent phase values: theoretically such a difference should be less than 2*pi, but in practice a value of about 4 is best. Nonetheless, as seen at high frequency for the 120 microsec curve, spurious discontinuties can be introduced. For very noisy phase data, the procedure can give in erroneous results.

The second factor (time shift) subtracts from the phase a term linear in frequency and proportional to the time shift:

$$\Delta\theta = -\omega\Delta t$$

At an angular frequency of 1 rad/microsec, a time shift of 30 microsecs produces a phase change of 30 rads, which is of the order of the discrepancy. The curves of Fig. 27(b) which show the spectra for several time segments all 350 microsecs long but starting at different times, do not exhibit this effect, possibly because there are two pulses within the selected time segments, as shown by the magnitude spectra given in Fig. 28 for the same segments. Above 70 microsecs, the low frequencies dominate the spectrum, but both high and low components are present.

By contrast, the phase spectra for a fixed time segment from a few different sensors (at different distances from the impact) are shown in Fig. 29 (a) and (b) for Tests 04/06-3 and 04/14-3,

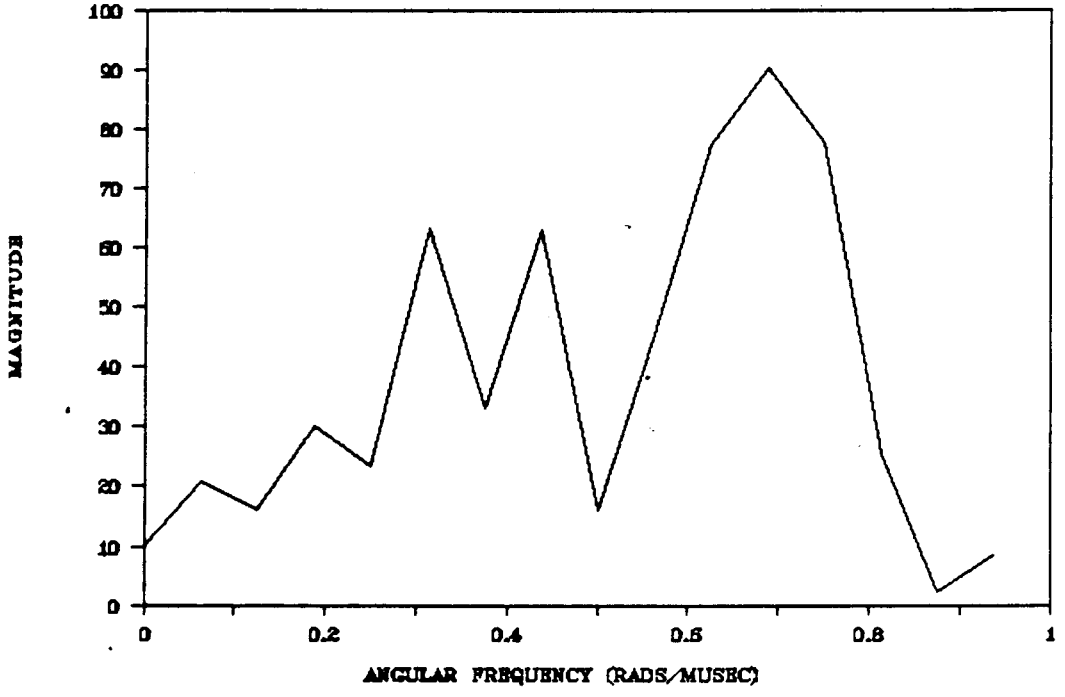

(a) First Pulse (50 - 150 microsec)

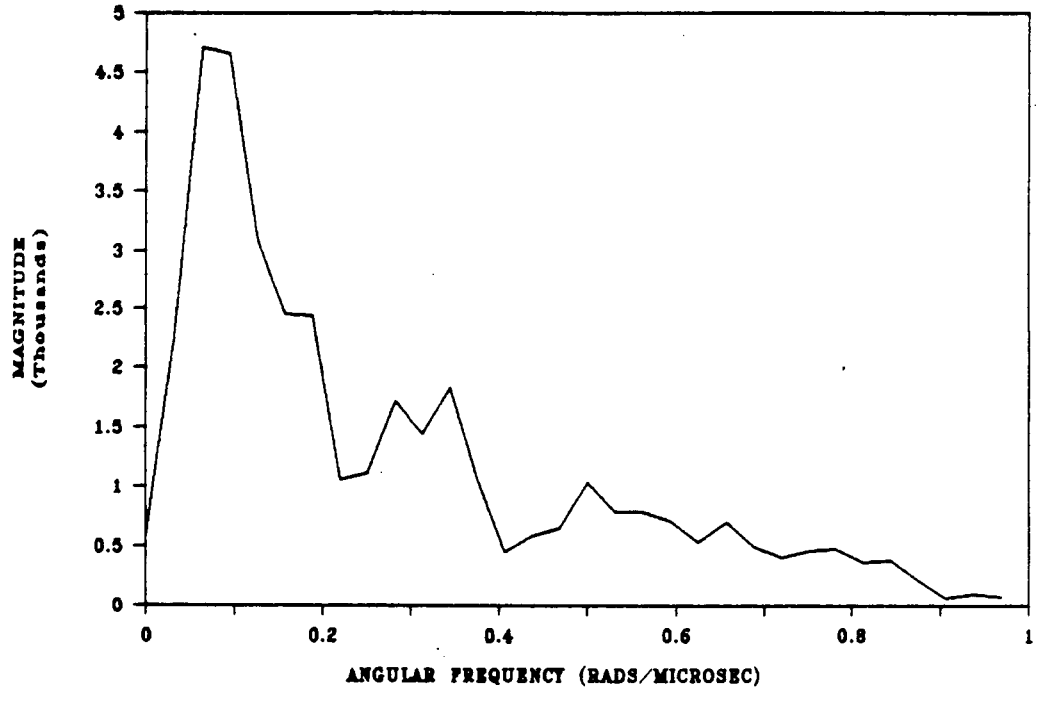

(b) Main Pulse (150 - 250 microsec)

Figure 25. Comparison of Magnitude Spectra for First and Main Pulses

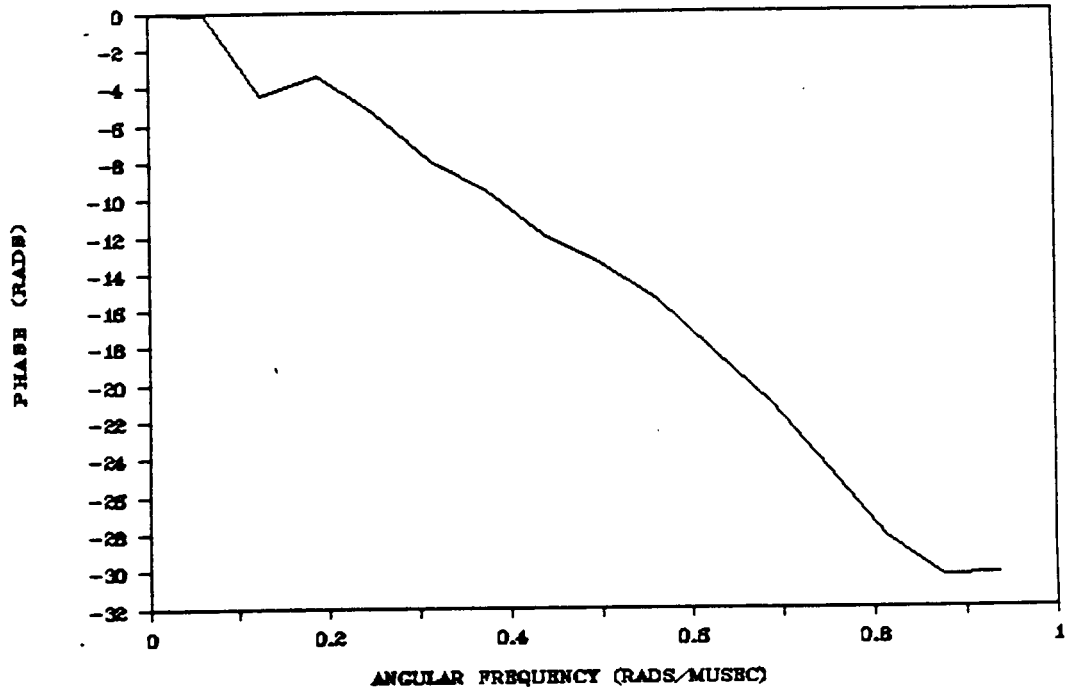

(a) First Pulse (50 - 150 microsec)

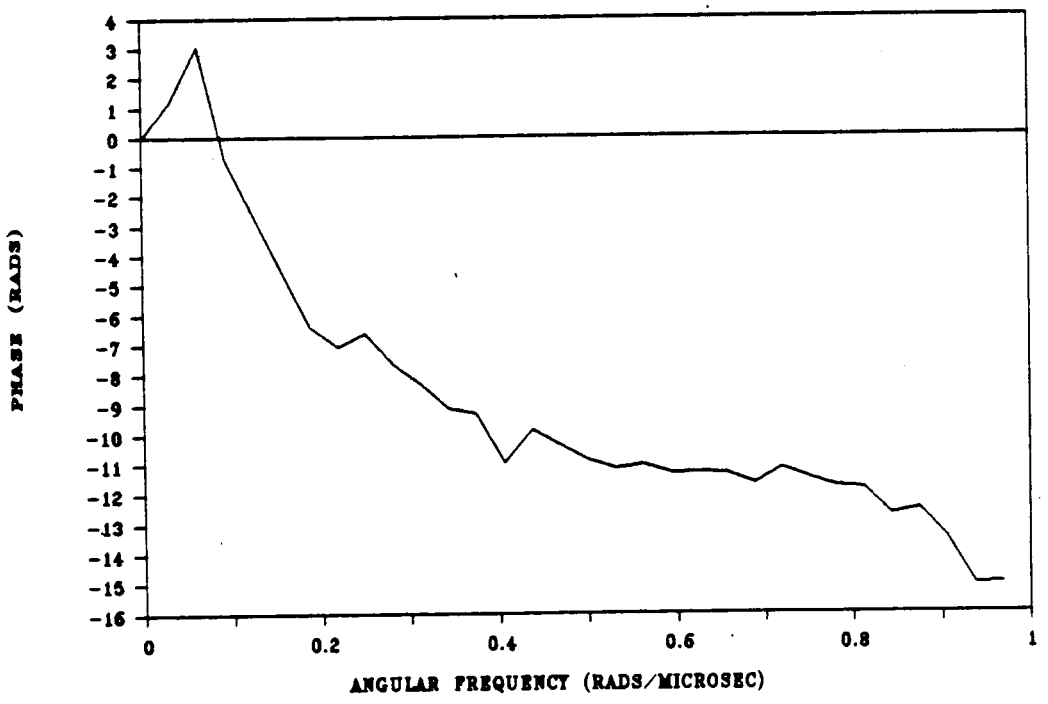

(b) Main Pulse (150 - 250 microsec)

Figure 26. Comparison of Phase Spectra for First and Main Pulses

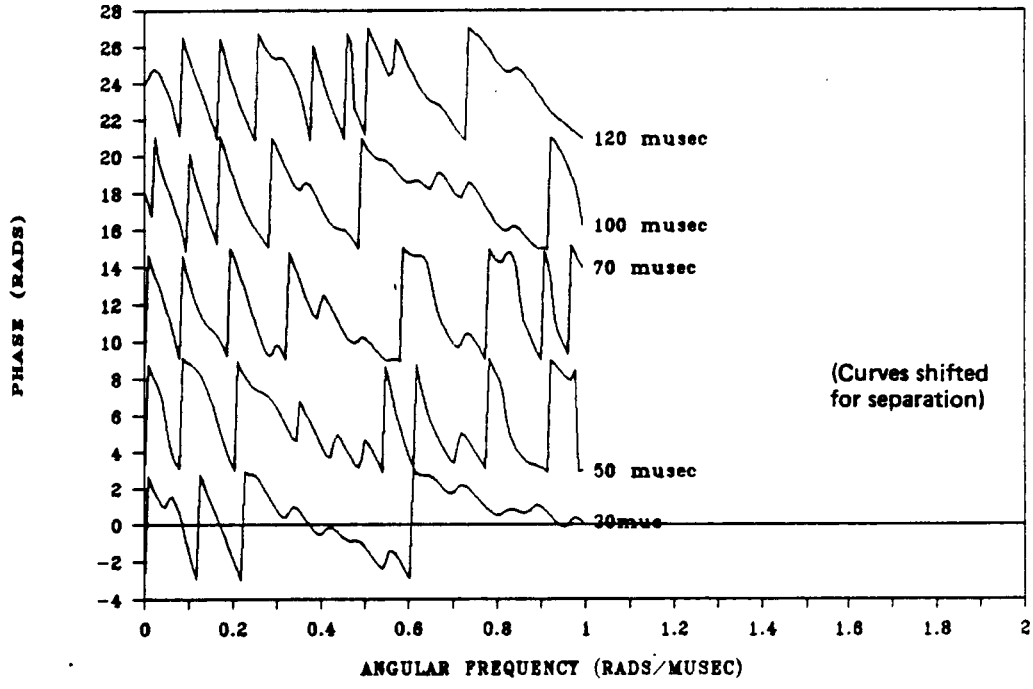

(a) Phase calculated by Principal Values of Arc Tangent

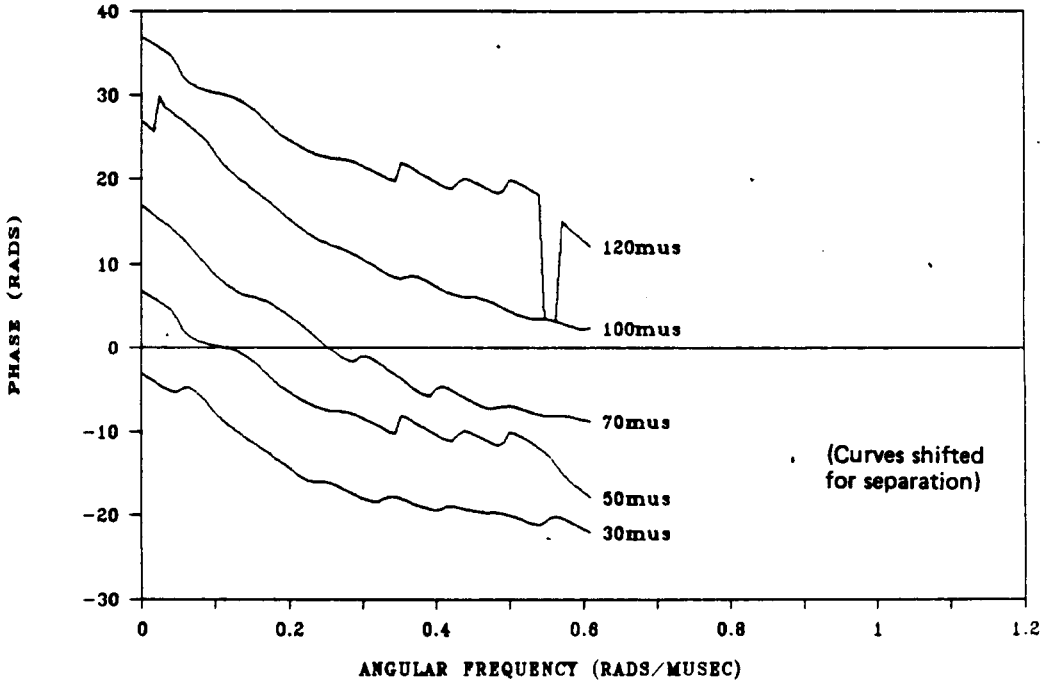

(b) Continous Phase Calculated by Eliminating Jumps

Note: Frequency scales are different in (a) and (b)

Figure 27. Illustration of Continous Phase Calculation for Several Time Segments (Test 03/06, Sensor No. 4)

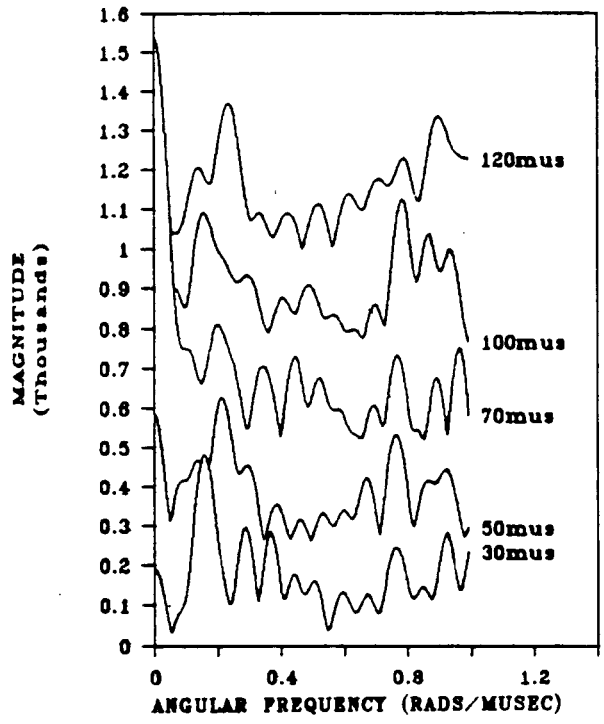

Figure 28. Magnitude Spectra of Several Time Segments (Test 03/06, Sensor No. 4)

respectively. The slopes of these spectra are related to the distance of the sensors from impact, as shown in Fig 30. The frequency derivative of phase is determined by the group velocity, since

$$d\theta/d\omega = (dk/d\omega)\, x - t_o = (1/C_g)\, x - t_o$$

From the figure the data fit moderately well to a line drawn with a group velocity of 5.2 mm/microsec, which is the velocity of the first wave. Since this is essentially non-dispersive, the group and phase velocities are the same.

The magnitude spectra for two different impactors, a steel BB (Test 04/06-3) and a nylon sphere (Test 04/14-1) are shown in Fig. 31. Sensors no. 1 in (a) and no. 2 in (b) are at about the same distance of 540 and 570 mm. These two spectra show that the nylon produces higher frequencies than the steel. This is expected on the basis of elastic impact theory, since the nylon sphere would bounce off early, after only one wave reflection, being of lower accoustic impedance then the aluminum, whereas the steel BB would remain in contact for a long time. The other spectra in the two tests somewhat confirm this.

5.4 Feature Analysis

Another step in analysing the data was the use of Feature/Cluster Analysis for pattern recognition. The intent was to evaluate the potential use of the method for discriminating types of impact, and possibly for quantitative measures such as impact speed. A software package for extracting features from waveform data, the 4060 System (reference 8) developed by General Research Corp. for their ALN 4060 Flaw Discriminator, was used to analyze some of the waveforms.

The software produces numerical values of 89 quantities such as peak amplitudes, total energies, times between peaks, spectral maxima, and statistics of peaks. In evaluating its usefulness for this application, the definition of the features extracted from an input signal have been reviewed, and collected into groups considered appropriate, as given in Table 5.

Some features, such as times of certain events, should be dependent on sensor position and some should not. Others should depend on impactor characteristics including speed or on plate response such as perforation. The features for sensors at three distances in Test 2/10 were reviewed briefly for correlation to sensor position, and 6 have been identified as plotted in Figure 32. These are described as:

No. 37 (ALN F1) - 25-90% rise time
No. 54 (ALN F13) - Phase coherence
No. 55 (ALN F14) - Phase coherence
No. 64 (ALN F34) - Power in first 1/8 of power spectrum
No. 60 (ALN F42) - Power in first 1/4 of power spectrum

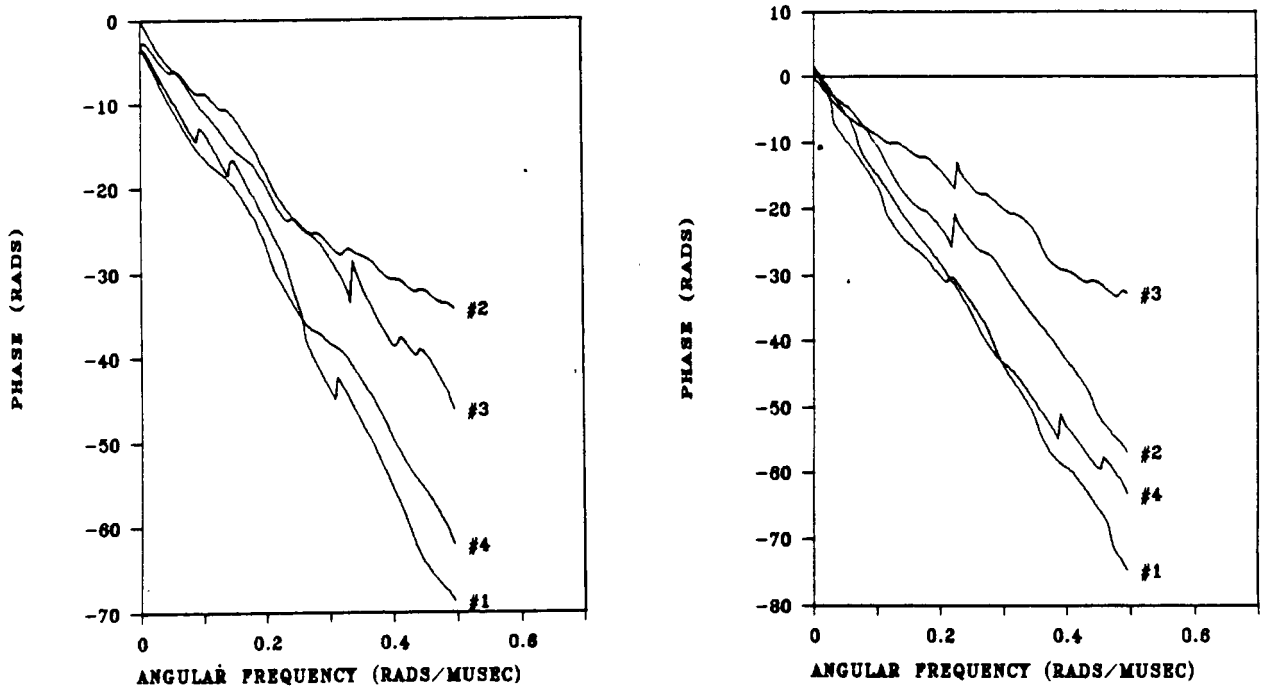

Figure 29. Phase Spectra for Several Sensors at Different Distances in Two Tests

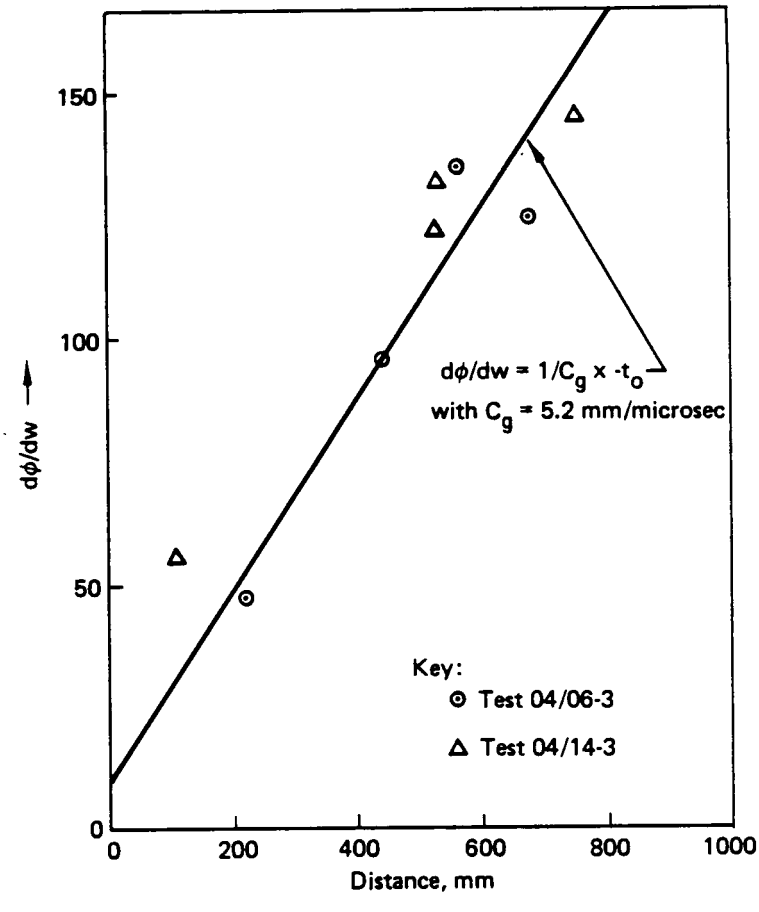

Figure 30. Slopes of Phase Curves for Two Tests as a Function of Distance

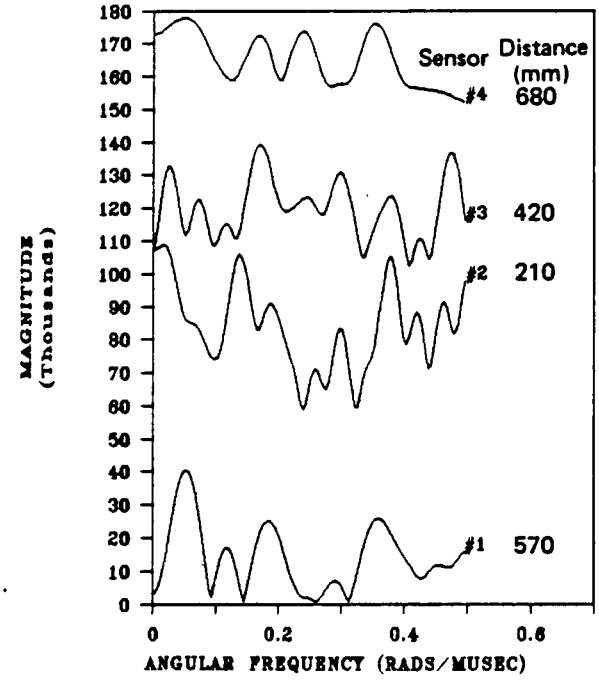

(a) Spectrum for Steel Impactor (Test of 04/06-3)

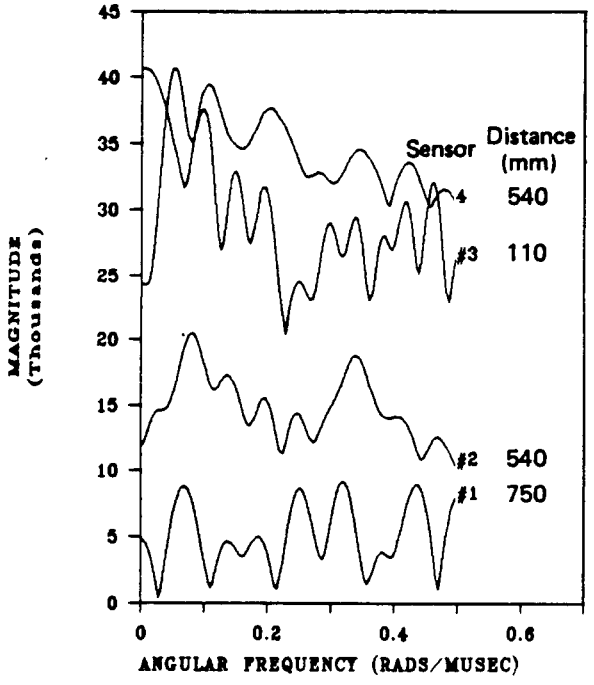

(b) Spectrum for Nylon Impactor (Test of 04/14-3)

Note:
Spectra shifted vertically to separate curves

Figure 31. Comparison of Spectra for Two Different Impactors—Steel and Nylon

Table 5. Definition of ALN Features and their Values for 2 Sensors in ALN Features for 04/06-3 No. 2 and 3

Name	ALN No	Ranges Inputs	Test No. 4063/2	Sensor No 4063/3
1 Pk amp	57	0-2048	9507	6168
2 Pk amp in W3	78	(0-200)	9507	4426
3 Pk amp in W4	79	(507-2048	973.6	895.5
4 Mean Amp	59	0-2048	1383	994.9
5 " " in W1	68	0-210	319.1	84.89
6 " " " W2	72	190-2048	1500	1087
7 " " " W4	82	(507-2048	6364	2672
8 Std Devn	60		1075	789.5
9 " " in W1	69		386.2	11.28
10 " " " W2	73		1060	770.6
11 " " " W4	83		1330	921.5
12 Ratio of 2 pks	61		0.6693	0.717
13 " """ in W1	71		0.1044	0.5153
14 " """ in W2	75		0.599	0.4178
15 " """ in W3	81		4	61
16 " """ in W4	85		84	29
17 No pks above thld	67	30	121	125
18 " " " frac 1	65	10%	100	103
19 " " " frac 1 in W1	70	"	1	0
20 " " " frac 1 in W2	74	"	100	103
21 " " " frac 1 in W3	80	"	1845	720.7
22 " " " frac 1 in W4	84	"	819.9	581.6
23 " " " frac 2	66	35%	14	22
24 A1/(A1+A2) in entire wfm	62		0.599	0.4178
25 Aw1/(Aw1+aw2)	77		0.1921	0.0173
26 Aw3/(Aw3+aw4)	89		0.599	0.624
27 Env time integ	26		1920000	1440000
28 Avg bef pk * avg aft pk	32		0.338	0.433
29 ditto shifted	33		12	16
30 Time at main pk	58		235	1495
31 Time betw 2 large pks	63		1176	1175
32 Time betw pk in W1 & W2	76		29	1447
33 Time betw pk in W1 & W3	86		0	1175
34 Time betw pk in W1 & W4	87		1176	462
35 Time betw pk in W3 & W4	88		1176	1637
36 t1/(t1+t2)	64		0.1428	0.8237
37 Rise time	1		2	7
38 Fall time	4		13	23
39 Pulse width @ .25 of pk	3		18	34
40 " " " .6 of pk	2		6	14
41 Centroid of entire wfm	27		1041	1115
42 2nd mom (Std Dev)	28		587.6	540.2
43 3rd mom (Skewness)	29		0.0318	-0.0933
44 4th mom (Kurtosis)	30		1.742	2.06
45 Effec pk curv	31		0.354	0.451

Table 5. Definition of ALN Features and their Values for 2 Sensors in ALN Features for 04/06-3 No. 2and 3 (Continued)

Name	ALN No.	Ranges Inputs	Test No. 4063/2	Sensor No. 4063/3
46 Time Phase @ .25 of pk	5		-0.816	2.236
47 Time Phase @ .6 " "	6		-0.698	2.971
48 Time Phase @ .9 " "	7		-0.934	-1.233
49 Time Phase @ peak	8		0.1258	-0.0065
50 Ph rate betw .25 up & dn	9		0.427	0.473
51 Ph rate betw .6 up & dn	10		0.59	0.64
52 Ph rate betw .9 up & dn	11		0.977	0.672
53 Ph coherence betw .25 u/d	12		-1.883	0.311
54 Ph coherence betw .6 u/d	13		20.34	14.08
55 Ph coherence betw .9 u/d	14		0.29	-0.0082
56 DC power sm/rect env	47		3.81E-06	0.00E+00
57 DC power analytic env	15		3.69E+12	2.08E+12
58 Power above DC s/r env	46		7.29E+12	3.65E+12
59 Power above DC anal env	16		3.64E+12	3.13E+12
60 Power in 1st 1/4	42		6.66E+12	3.42E+12
61 Power in 2nd 1/4	43		3.53E+11	1.60E+11
62 Power in 3rd 1/4	44		1.51E+11	3.90E+10
63 Power in 4th 1/4	45		1.33E+11	3.20E+10
64 Power in 1st 1/8	34		5.58E+12	2.70E+12
65 Power in 2nd 1/8	35		1.08E+12	7.20E+11
66 Power in 3rd 1/8	36		3.05E+11	1.54E+11
67 Power in 4th 1/8	37		4.80E+10	5.00E+09
68 Power in 5th 1/8	38		4.27E+10	2.30E+09
69 Power in 6th 1/8	39		1.08E+11	3.71E+10
70 Power in 7th 1/8	40		9.73E+10	3.12E+10
71 Power in 8th 1/8	41		3.53E+10	9.00E+08
72 Centroid of sm env PSD	53		113.70	97.50
73 " " pk 1/4 sm env	49		75.91	74.30
74 2nd moment of PSD	54		155.10	124.60
75 " " of pk 1/4	50		65.09	69.18
76 3rd moment of PSD	55		3.12	3.22
77 " " of pk 1/4	51		0.64	0.96
78 4th moment of PSD	56		14.28	17.14
79 " " of pk 1/4	52		2.53	2.83
80 Phase coh over pk 1/8	48		0.30	-0.20
81 1st decile of Anal Env PS	17		1.00	1.00
82 2nd " " " " "	18		1.00	1.00
83 3rd " " " " "	19		1.00	1.00
84 4th " " " " "	20		1.00	2.00
85 5th " " " " "	21		1.00	38.00
86 6th " " " " "	22		15.00	128.00
87 7th " " " " "	23		78.00	338.00
88 8th " " " " "	24		183.00	569.00
89 9th " " " " "	25		585.00	786.00

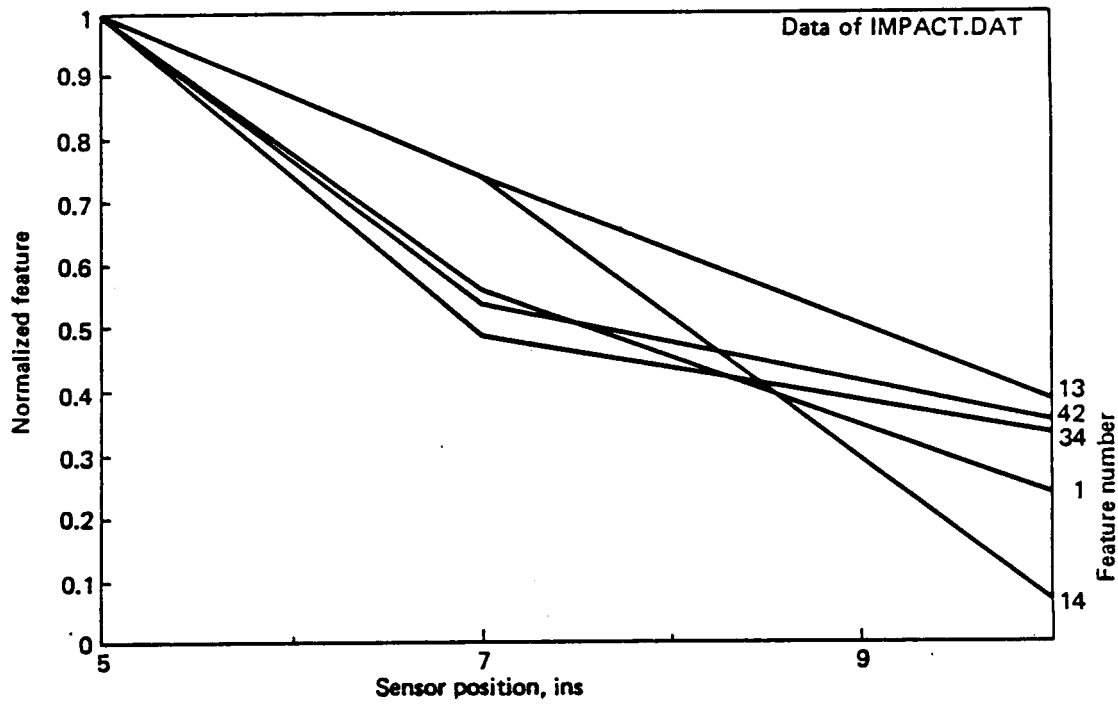

Figure 32. Correlating Features of Waveforms

6.0 CONCLUSIONS

The potential of a space debris measuring system, based on collecting panel response data from particle impacts, has been evaluated from two major points of view: the statistics of the space debris environment were analyzed to determine the probability of success of the system, and experimental data from impact tests were used to determine the usefulness of the measurements of the system.

Particle flux data for space debris and data on its velocity distribution were combined to produce probability data for momentum of impacts. These were then applied to the panels of the Space Station Logistics Module showing that for a typical impact detection sensitivity of 0.1 g.m/sec, the probability of an event occuring in the six months that the module is in orbit is about 0.3 for each panel of about 1.4 sq.m. For all the panels on the entire module the measurement system will then produce a marginal amount of data. Increased sensitivity of the detector system is certainly possible, and no attempt has been made to improve it. New sensor susytems, such as embedded acoustic waveguides currently being developed offer such improvement.

The waveforms from impact tests have been analyzed to evaluate two factors: the potential accuracy of locating the impact point and the feasibility of extracting impact characteristics from the waveforms.

The accuracy of measuring arrival times is within about 3 microsecs., which represents 15 mm of propagation at the wavespeed (about 5mm/microsec) of the first in-plane wave motions. This leads to an accuracy of location of about 75 mm through the use of the location algorithm using 4 waveforms. Repeatability from test to test and between tests is within the same tolerance.

The response data is shown, by analysis of the spectrum of the response, to be separable into the two modes of plate response: in-plane and transverse (bending) motions. The spectral magnitude is concentrated at high frequency for the first waves and at low frequency for the bending.

The in-plane response is the faster and arrives first, and at almost constant wavespeed. It is therefore well suited for use in the location algorithm. Methods for automatically identifying the arrival of this motion were developed.

The bending motion is slower, and highly dispersive: the wavespeed increases with frequency so that the high frequency components arrive first followed by low frequency motions later, stretching the pulse in time. The spectral behavior of the phase of these motions was shown to be predicted by plate bending theory and to be related to the propagation distance. This data could be used in the location algorithm or in a procedure for determining the propagation wavespeed.

Analysis of two waveforms taken at approximately the same distance from the impact in two tests, one with a steel BB and one with a nylon sphere, showed that the latter had a higher frequency spectrum as expected from impact rebound theory.

Preliminary use of feature analysis showed that waveforms could be distinguished on the basis of statistical analysis when distinct characteristics existed, such as the distance of the sensors. The data set, developed initially for evaluating location procedures, was inadequately varied with regard to impact parameters such as mass, velocity, or momentum to evaluate the ability to determine these quantities.

The conclusions reached are that the use of sensors to measure the motions of a panel after impact can produce data on the location and characteristics of the impact, and that the Logistics Module panels provide a possible application for detecting the low probability events of concern. The Method requires further development of data processing, and, to extend the range of detection requires the use of more sensitive sensors.

REFERENCES

1. "Spacecraft Strain and Acoustic Sensors", Joseph S.Heyman, NASA/LaRC, TDMX 2072.

2. "Task 4 - Impact Detection/Location system, Space Station Integrated Wall Design and Penetration Damage Control", J. M. Nelson and B. M. Lempriere, Boeing Aerospace Co. Final Report D180-30550-3, Contract NAS8-36426, July 1987.

3. "Orbital Debris Environments for Space Station", D. J. Kessler, JSC 20001.

4. "Trajectory Determinations and Collection of Micrometeoroids on the Space Station", Ed. by F.Horz, Lunar Planetary Institute Report LPI 86-05, Dec 16 1985.

5. PEN 4 Version 8 Hypervelocity Impact Analysis, Boeing Aerospace Company IR&D Doc. No. D180-29230-1, M.D. Bjorkman and J.D. Geiger, 2/27/86.

6(a) Handbook of Engineering Mechanics, W. Flugge Editor, McGraw-Hill, Book Company, 1962, p64-16, Vibrations/Propagation of Elastic Waves, by E. E. Zajac.

6(b) ibid, p61-14, Vibrations/Continuous Systems, by D. Young

7. Applied Time Series Analysis, vol. 1, Basic Techniques, R.K. Otnes amd L. Enochsen, John Wiley & Sons, NY, 1978.

8. User's Guide and Technical Reference, 4060 Software System - Version 1.0, General Research Corp., Dec 1984.

This page left blank intentionally

Appendix A

Waveforms for All Tests

PRECEDING PAGE BLANK NOT FILMED

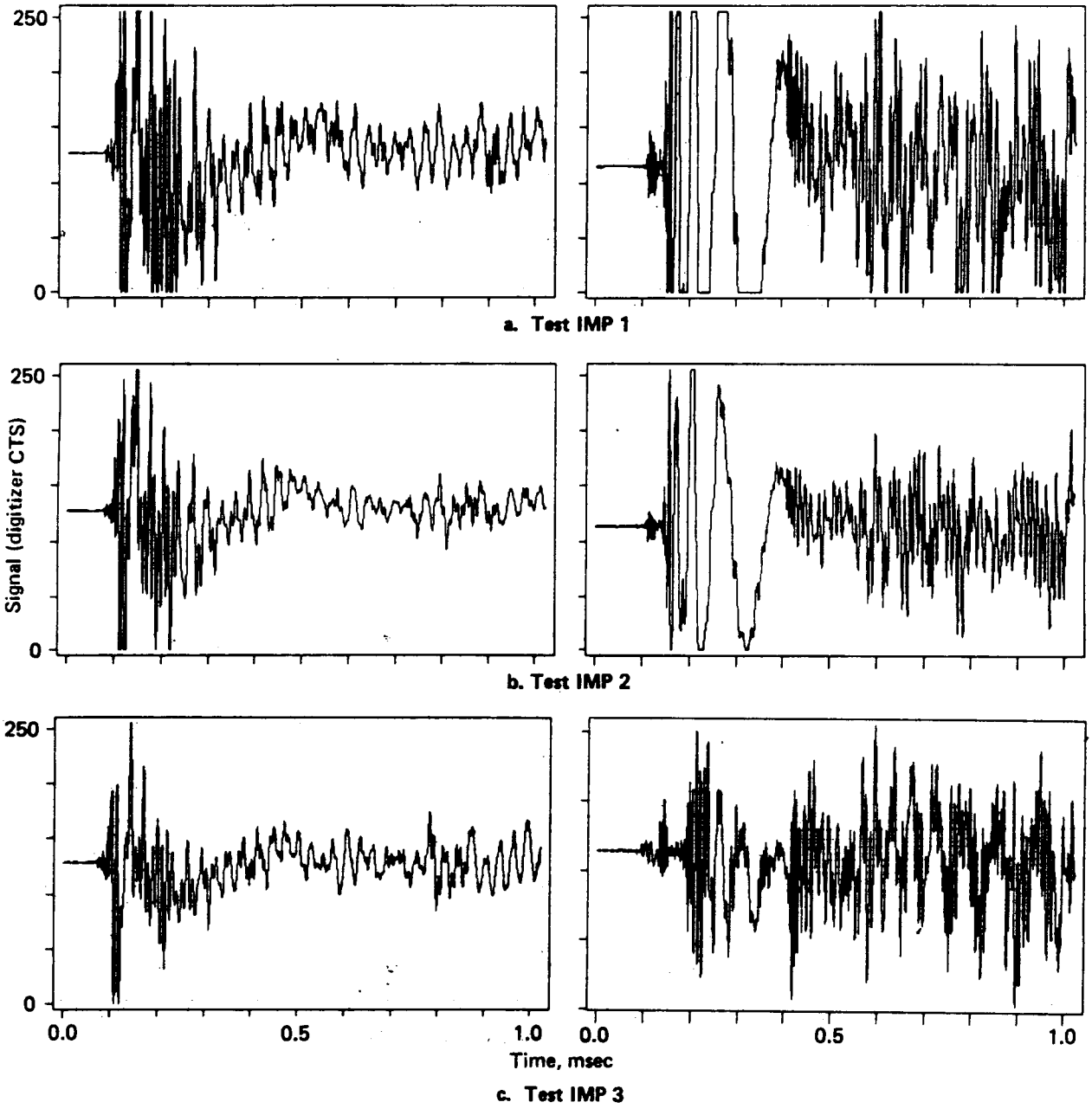

Figure A-1. Tests of 01/21/87: Three Repeats at 4 in and 10 in

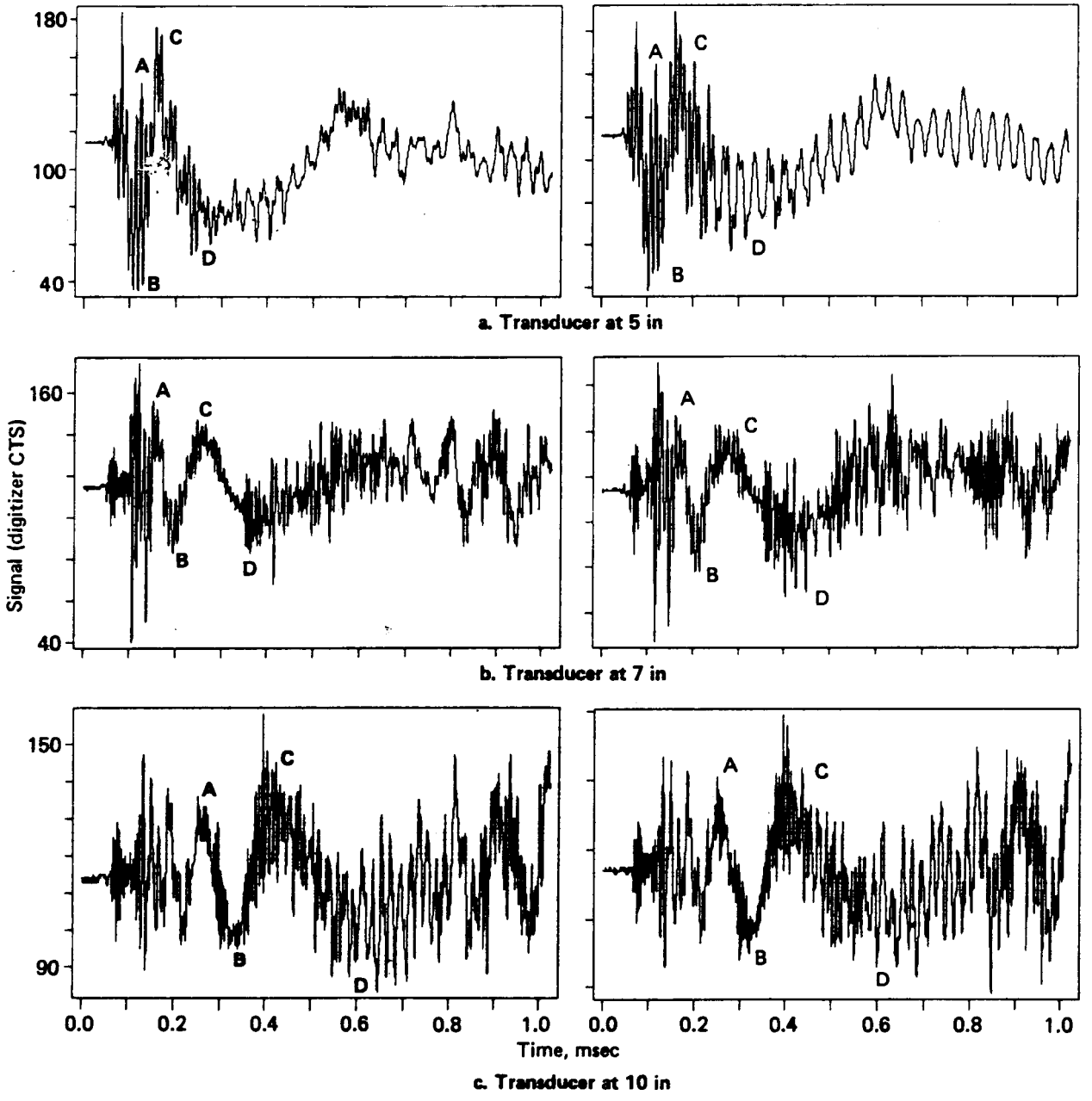

Note: A, B, C, and D denote four identifiable propagating peaks/troughs

Figure A-2. Tests of 02/10/87: Two Repeats at 5 in, 7 in, and 10 in

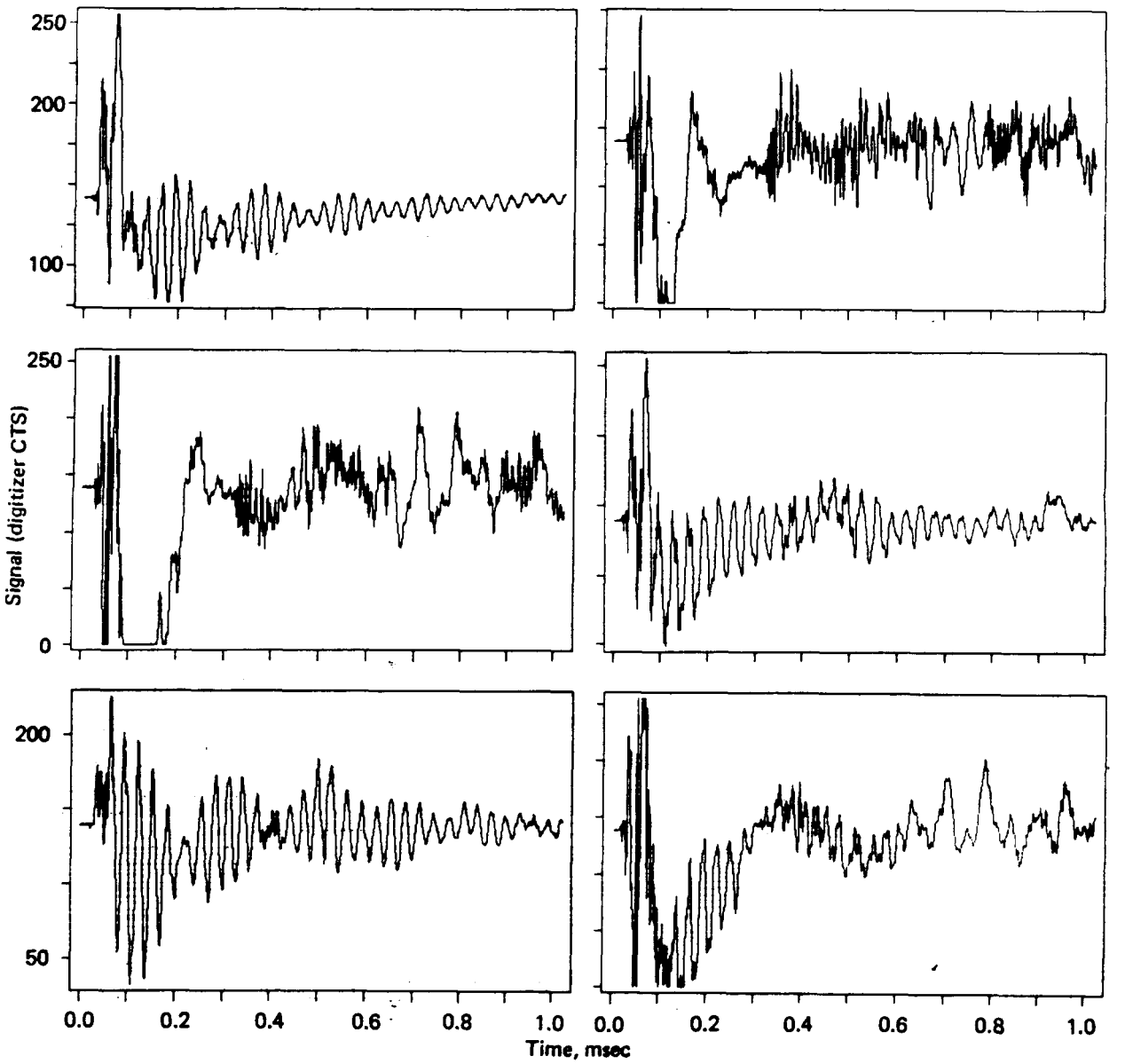

Figure A-3. Tests of 02/10/87: Six Repeats of Reference Transducer at 3 in

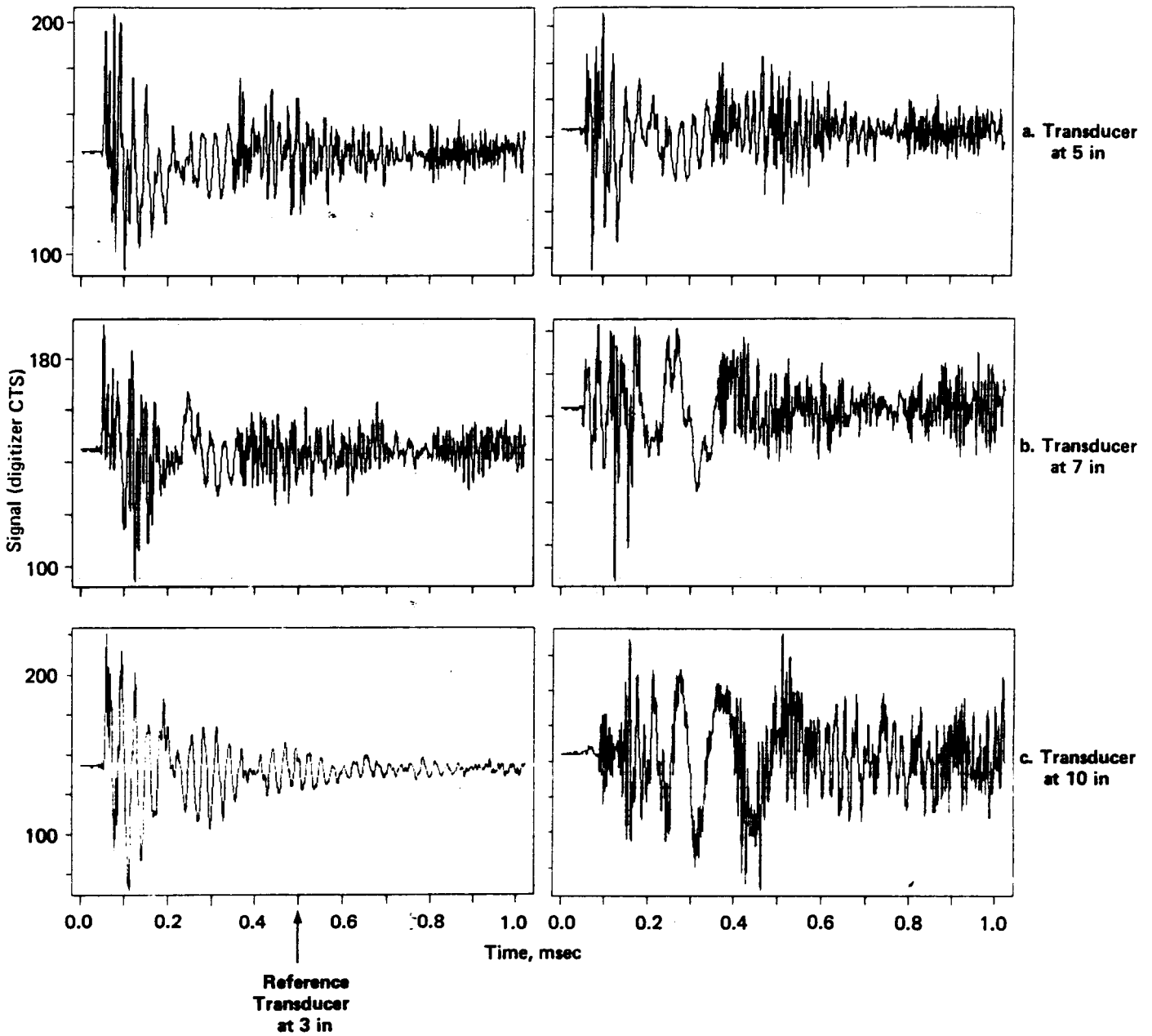

Figure A-4. Tests of 03/05, 06/87: Transducers at 5 in, 7 in, and 10 in Together With Reference at 3 in

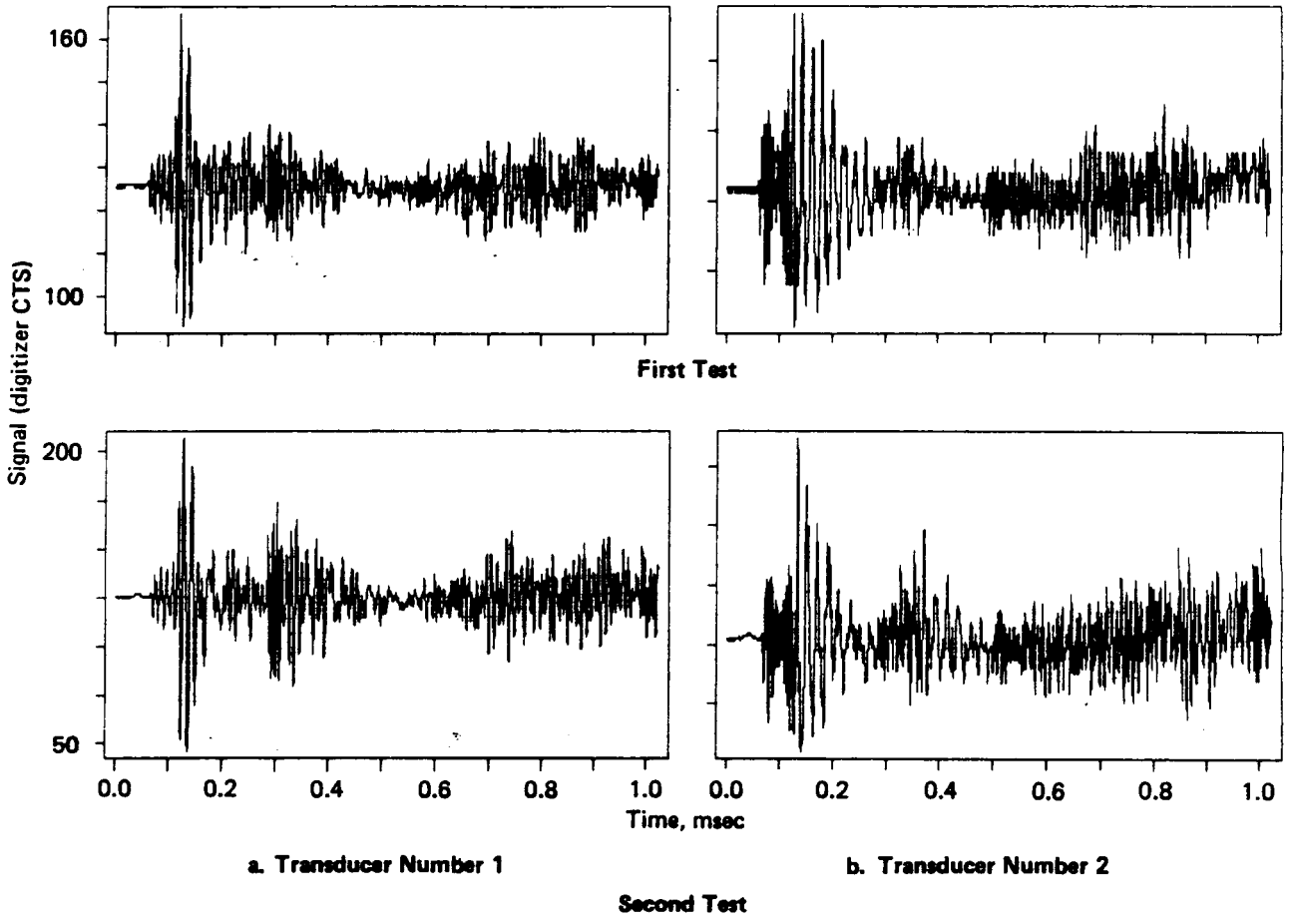

Figure A-5 Tests of 03/20/87: Two Repeats With Two Sensors at 10 in

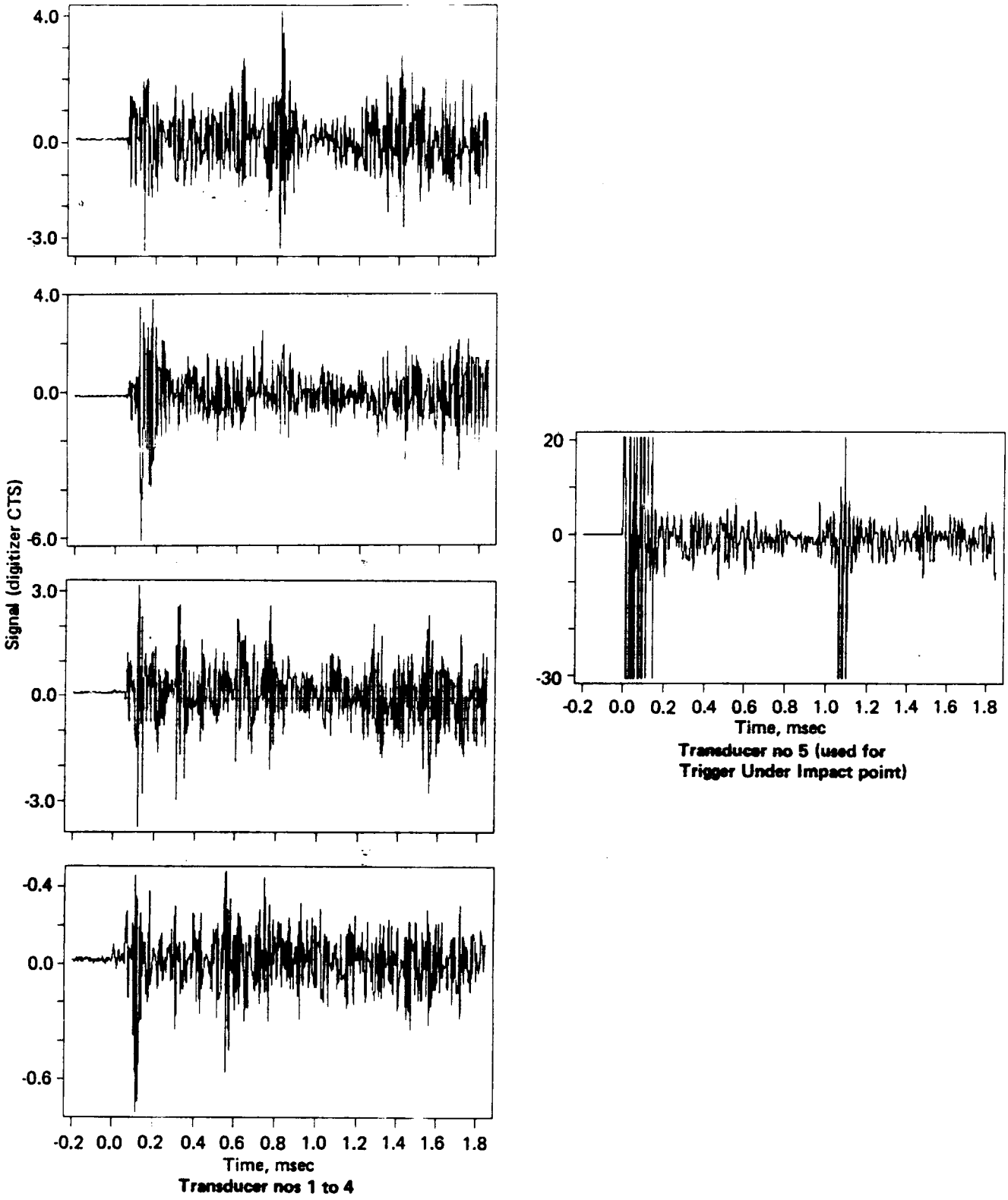

Figure A-6. First Test of 03/25/87: Four Transducers Close Together at 12 in and Trigger Transducer at 0 in

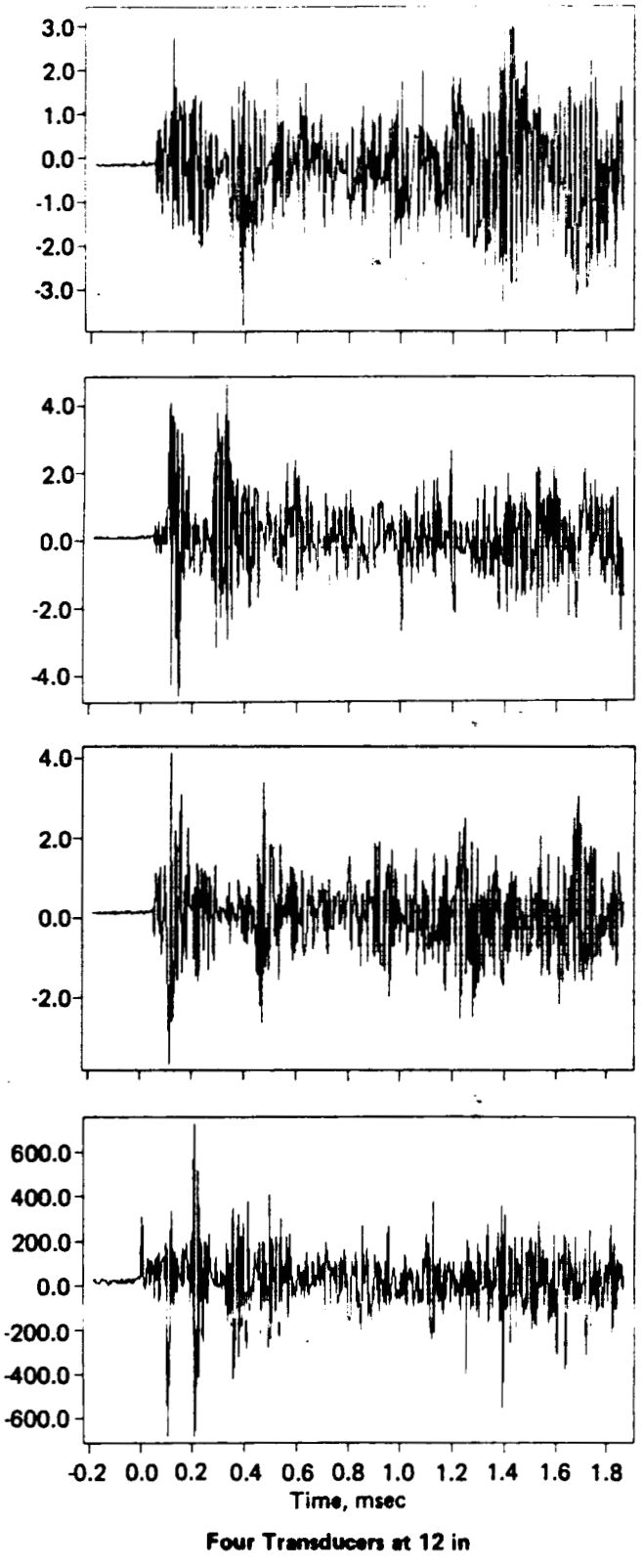

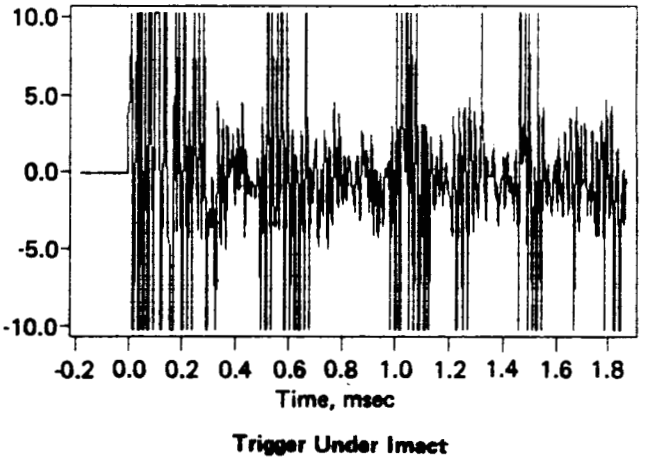

Figure A-7. Second Test of 03/25/87: Four Transducers at 45^{O} Separations on 12 in Circle and Trigger Transducer at 0 in

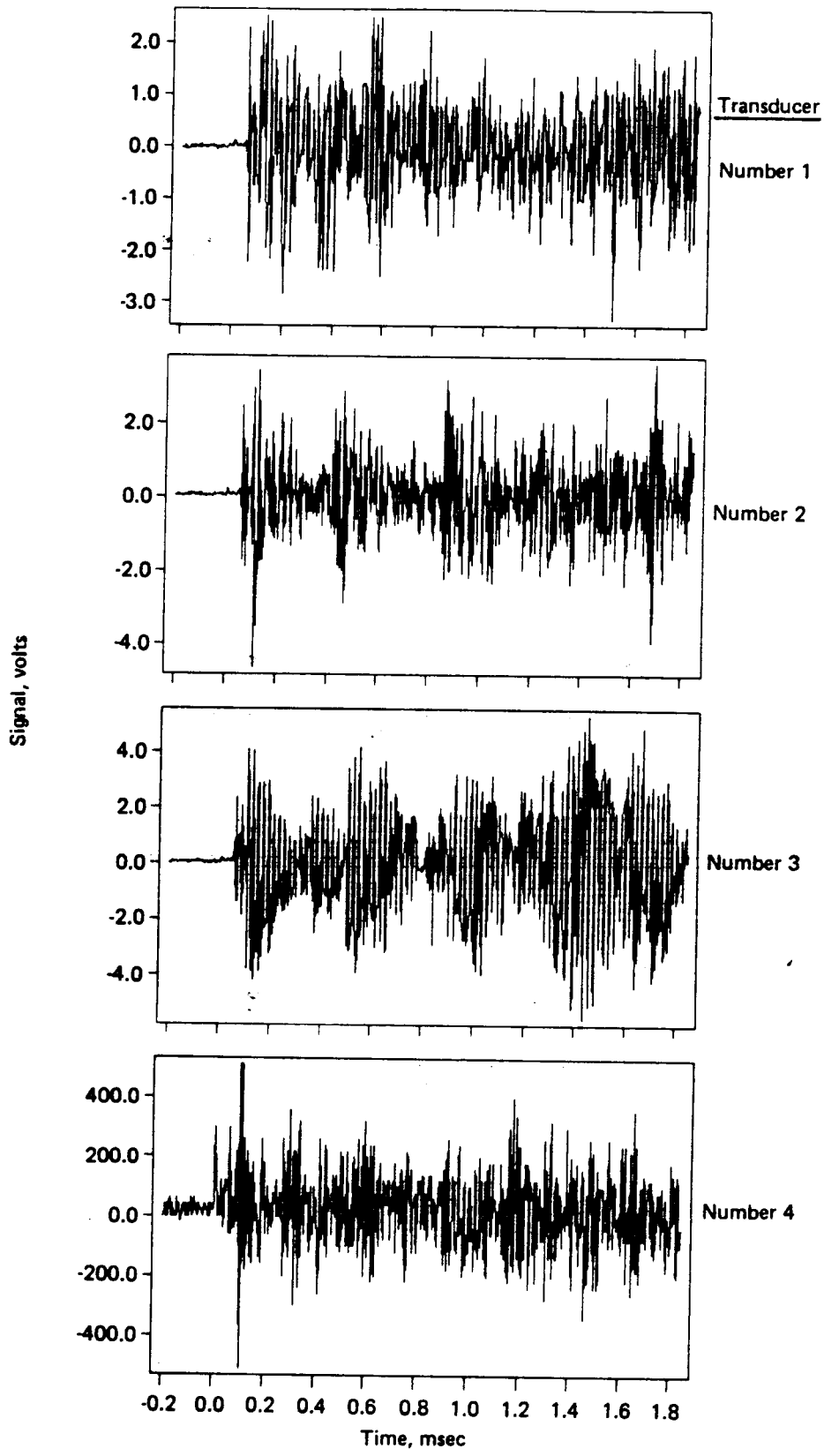

Figure A-8. Test of 04/01/87: Four Transducers at 45° Intervals on 12 in Radius

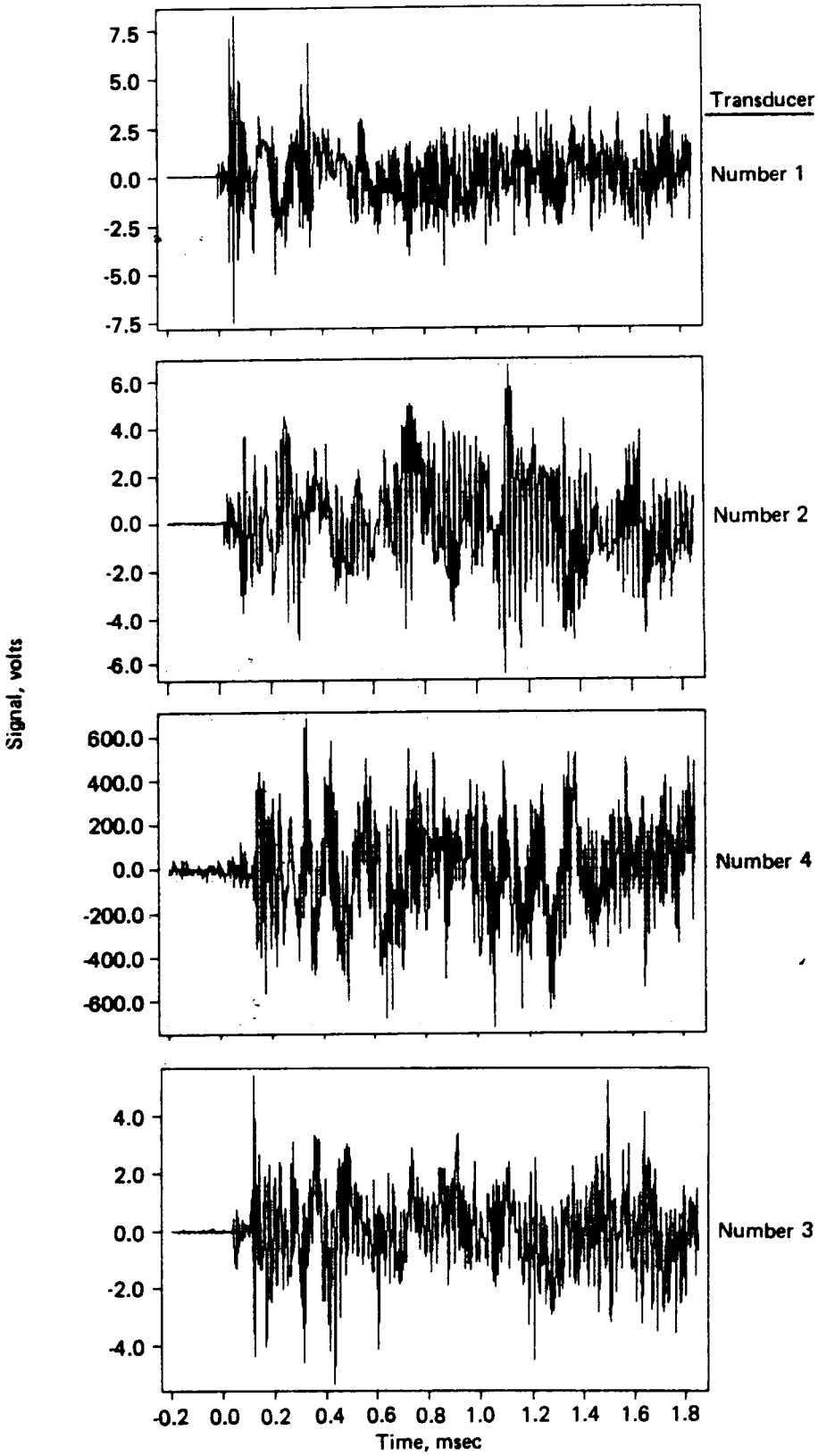

Figure A-9. Test of 04/02/87: Four Transducers at 45^{O} Intervals on 12 in Radius

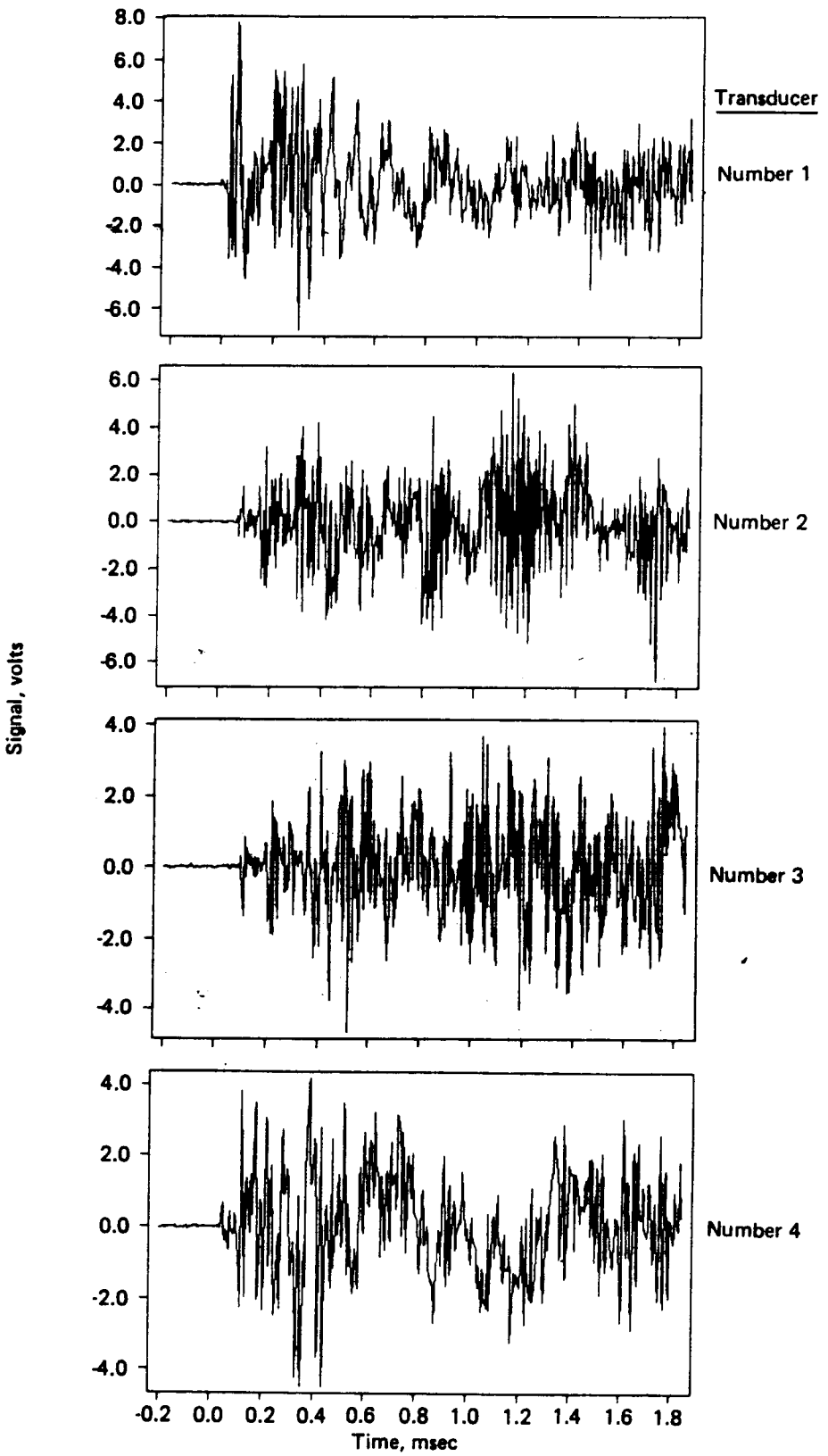

Figure A-10. First Test of 04/06/87: Four Transducers at 45° Intervals on 10 in Radius

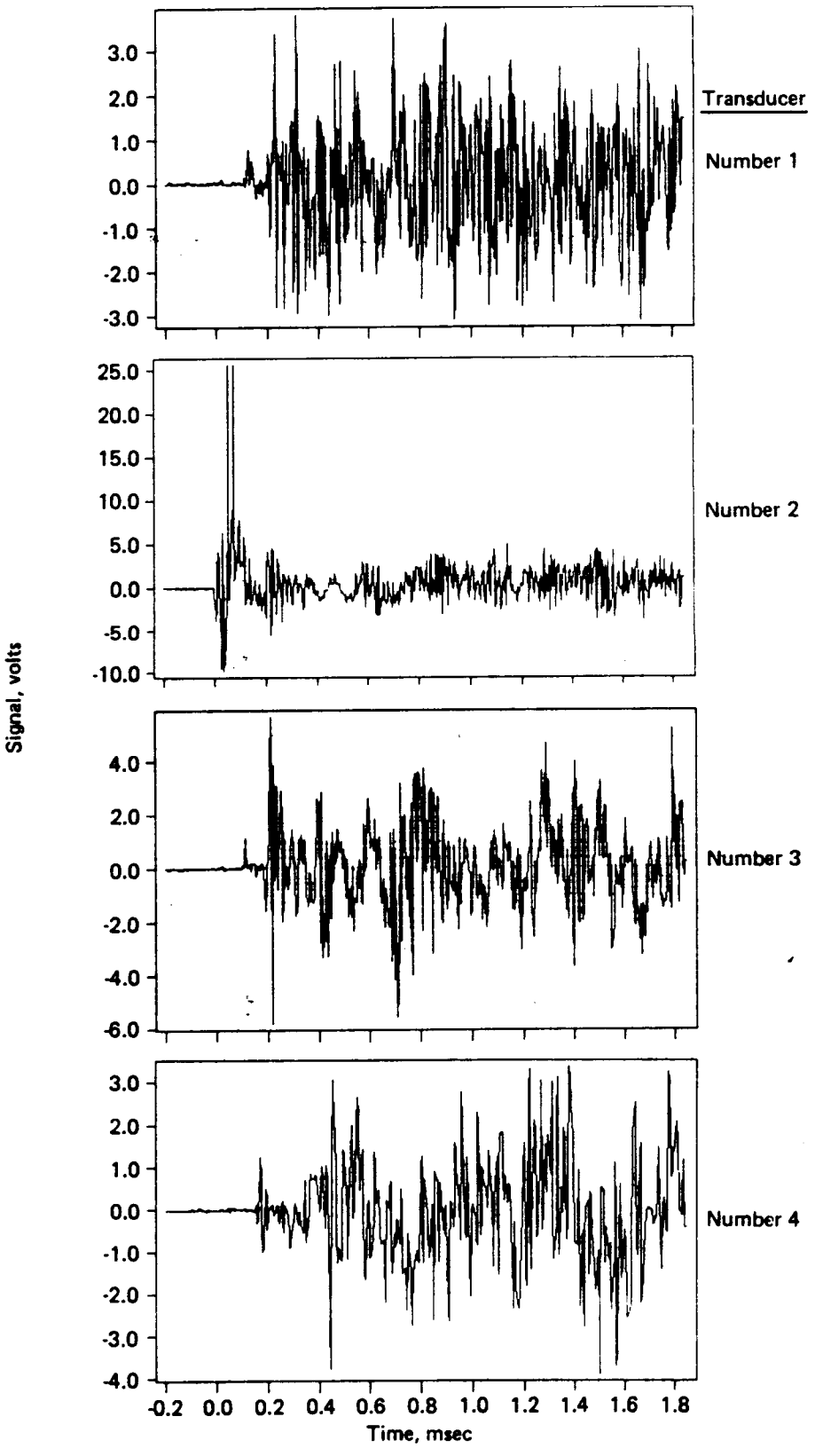

Figure A-11. Second Test of 04/06/87: Four Transducers at 45^{o} Intervals on 10 in Radius

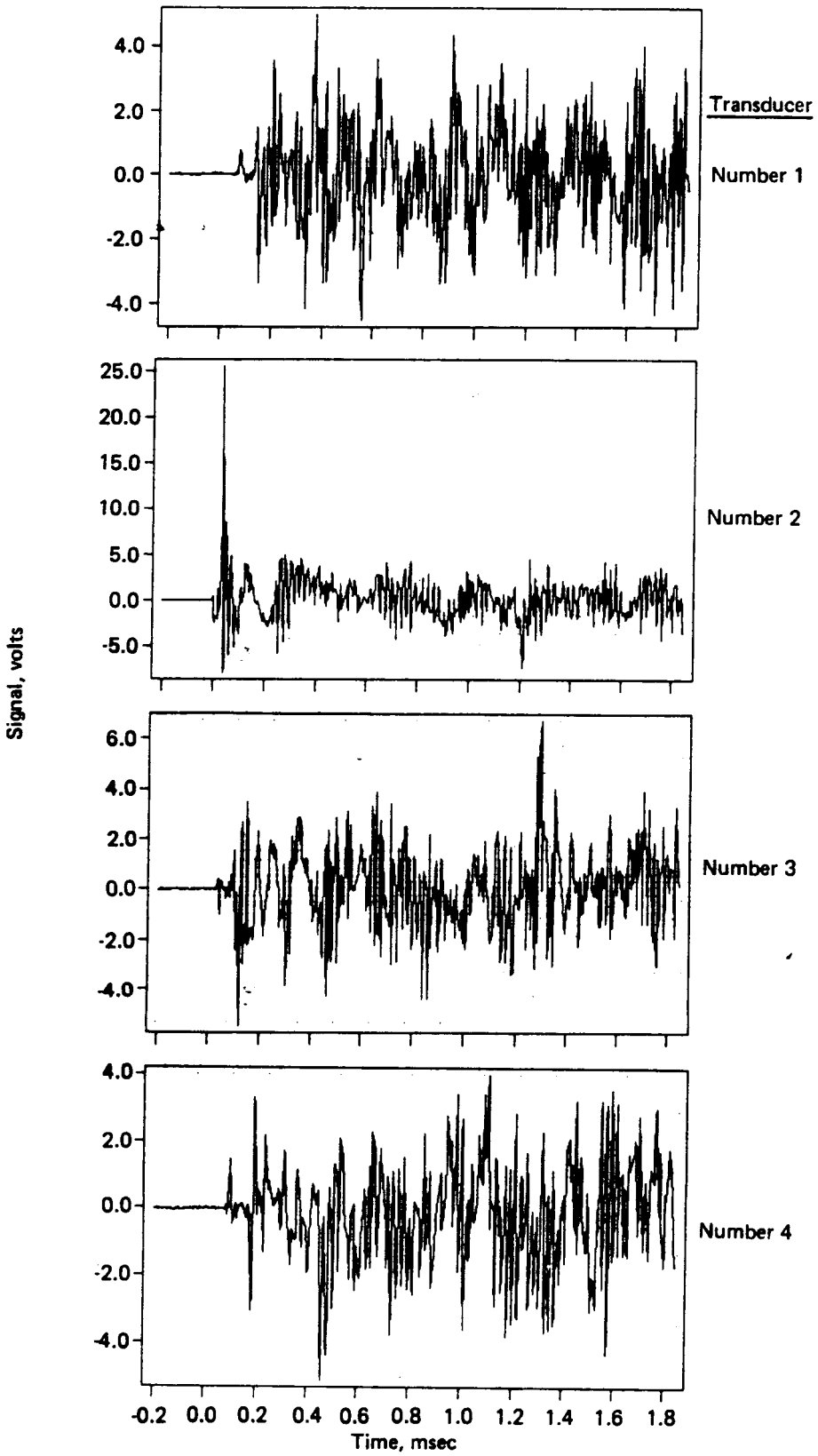

Figure A-12. Third Test of 04/06/87: Four Transducers at 45^{0} Intervals on 10 in Radius

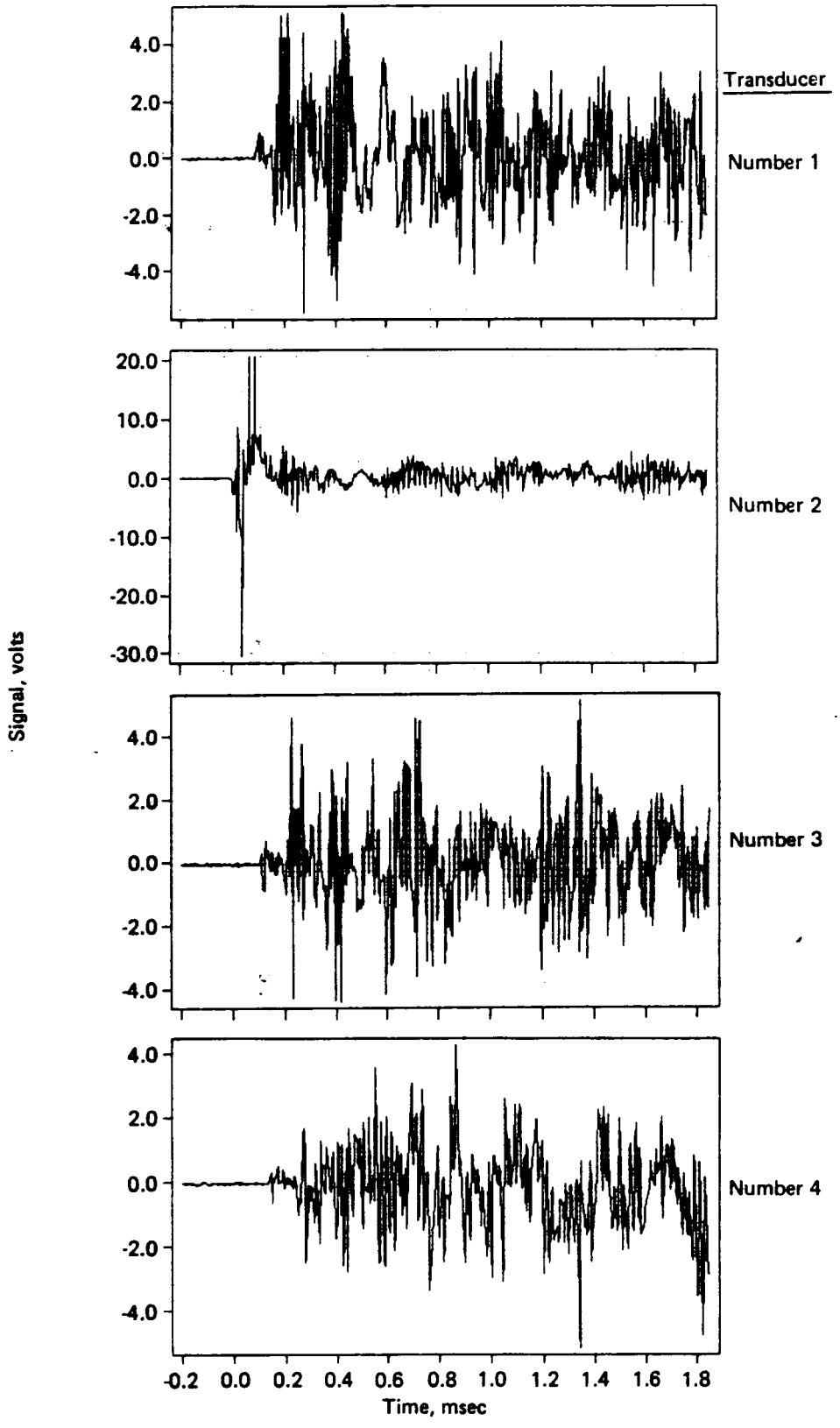

Figure A-13. Test of 04/07/87: Four Transducers at 45° Intervals on 10 in Radius

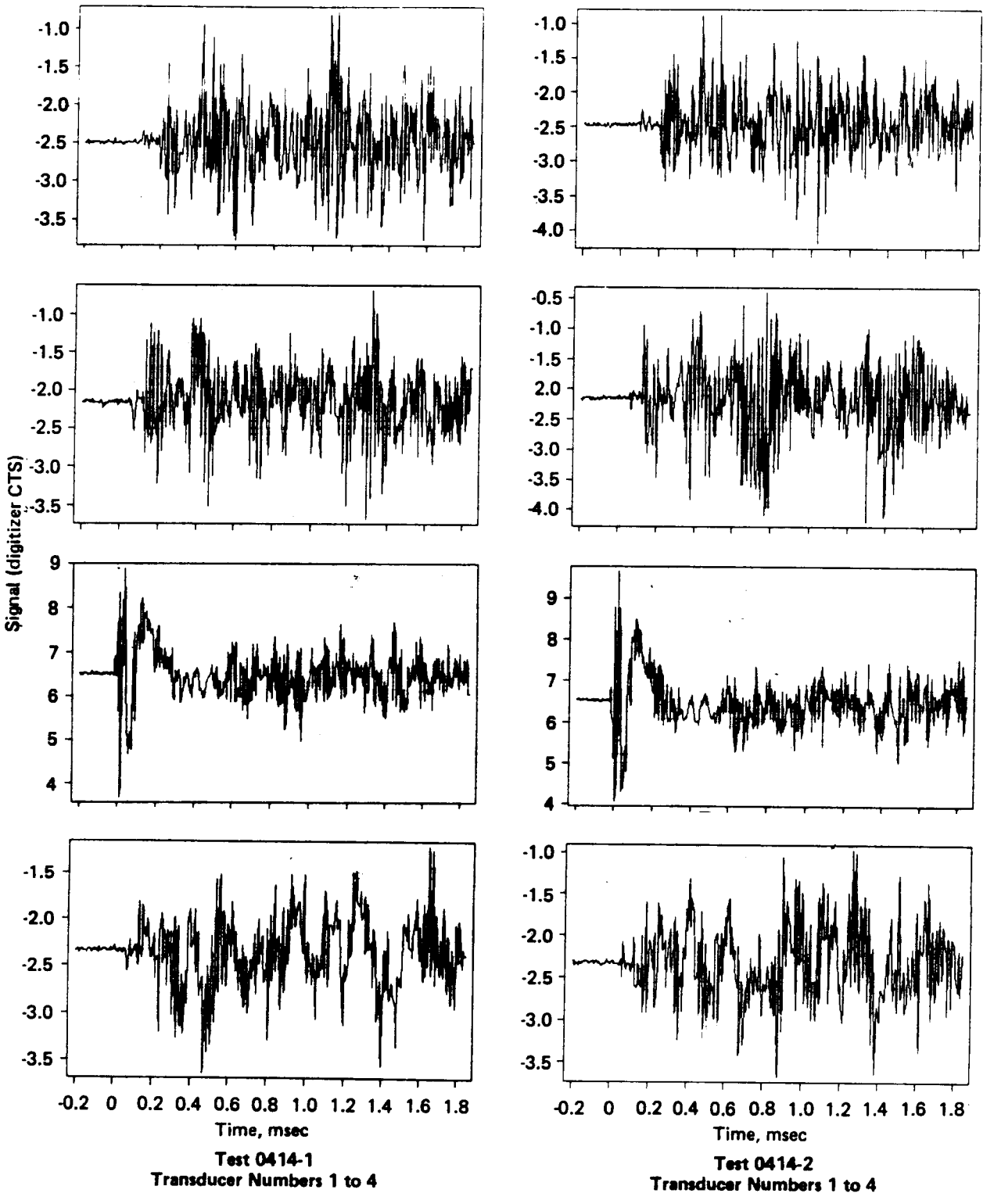

Figure A-14. First Two Test of 04/14/87.

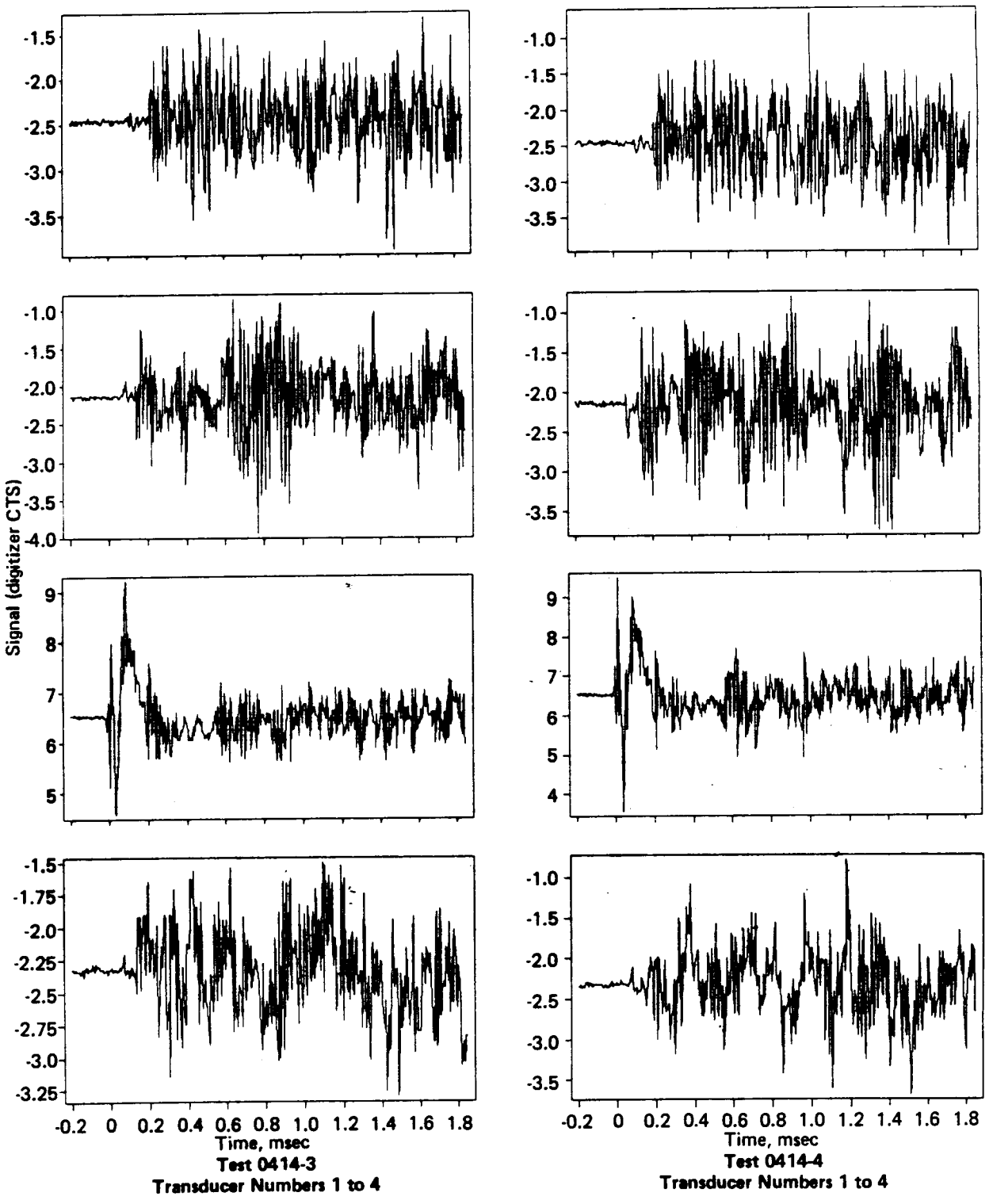

Figure A-15. Last Two Tests of 04/14/87

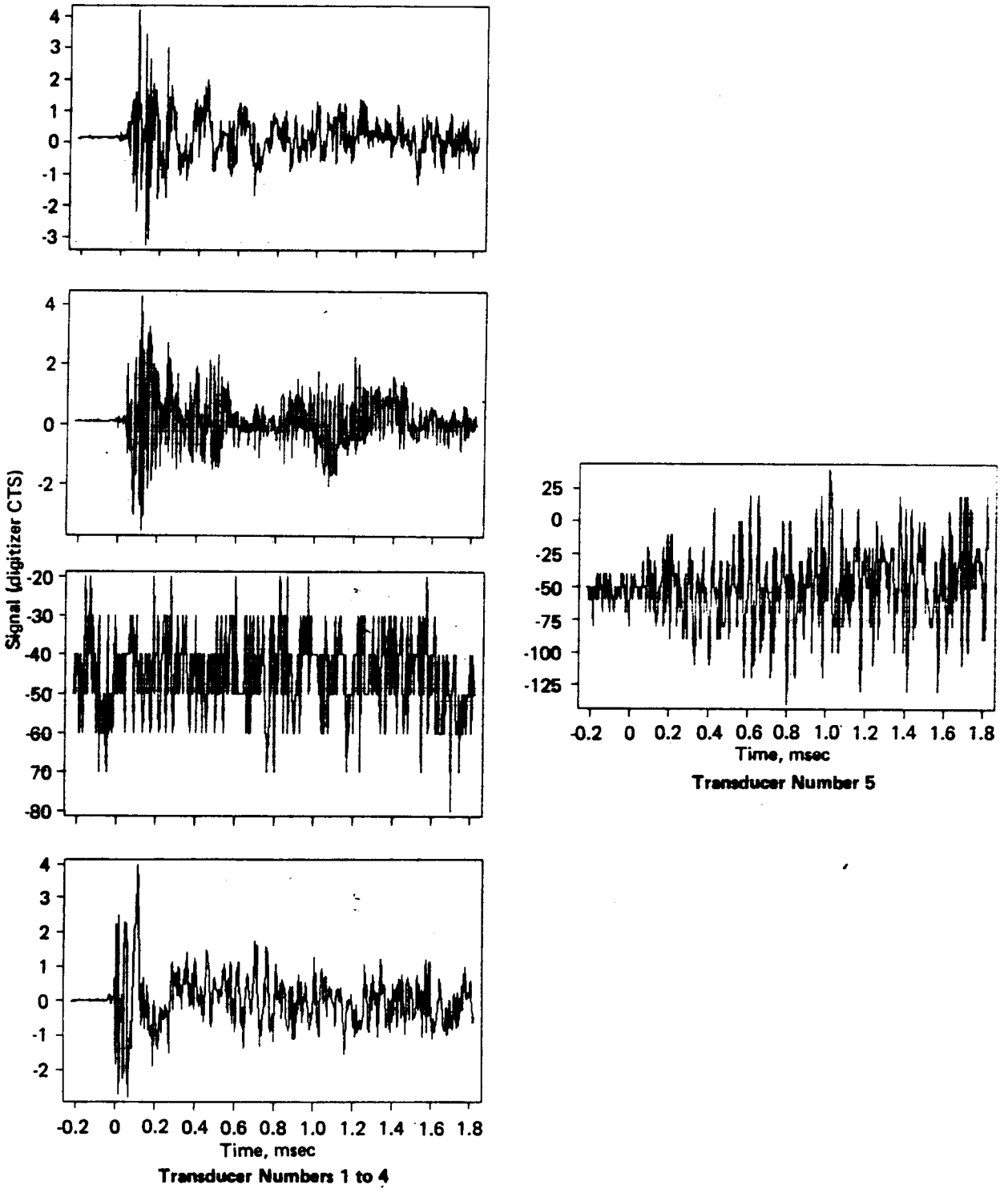

Figure A-16. First Test of 04/20/87

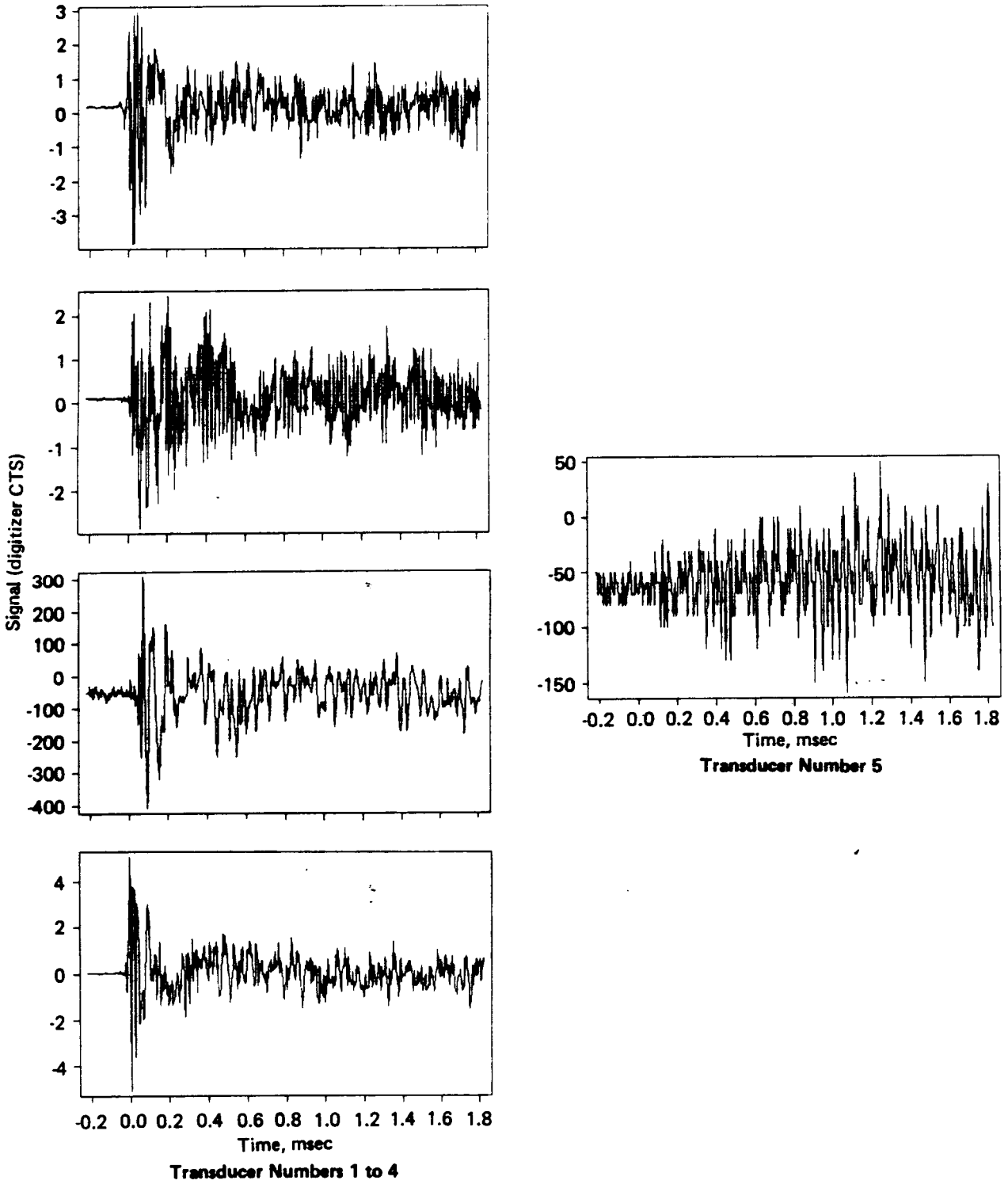

Figure A-17. Second Test of 04/20/87

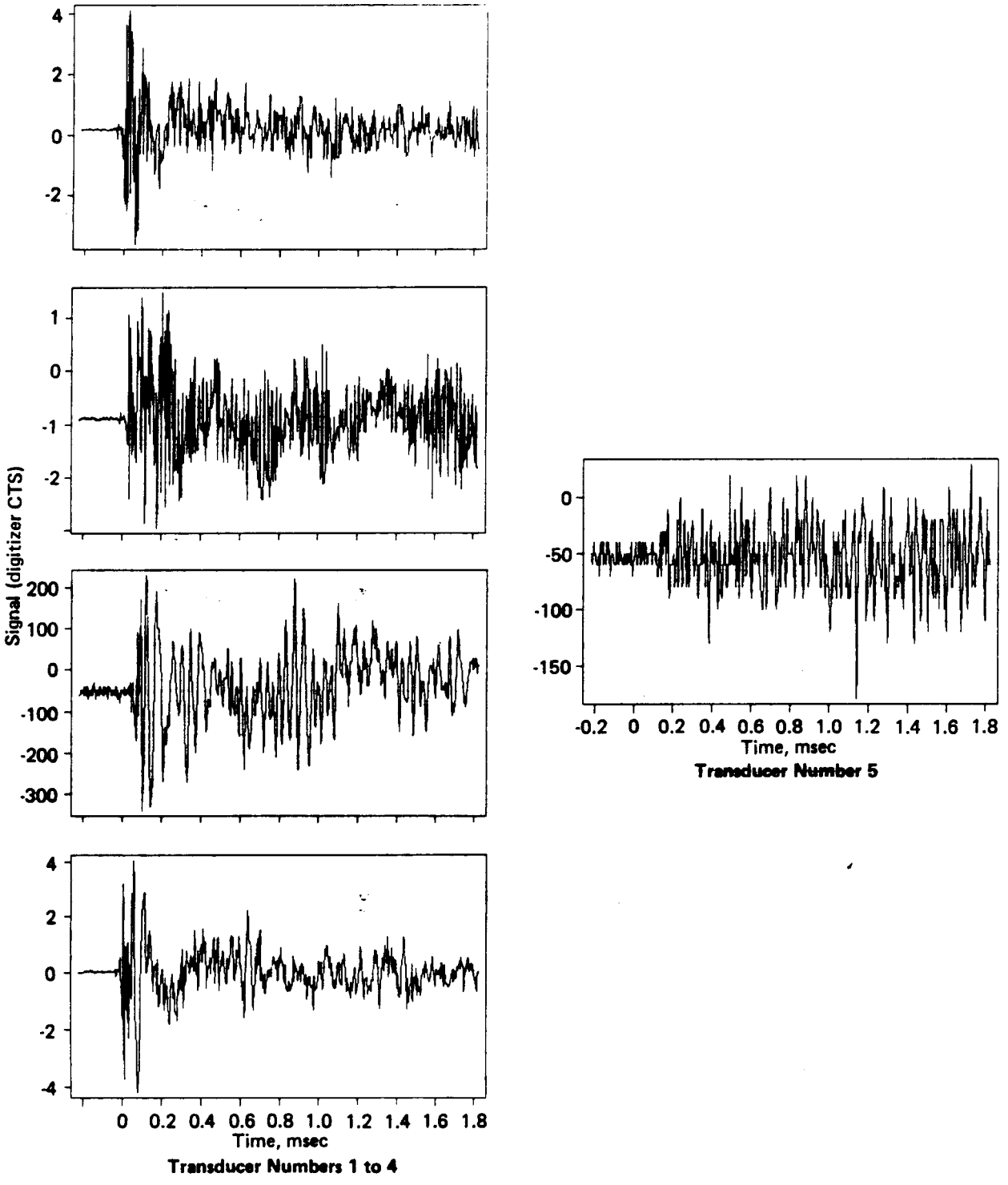

Figure A-18. Third Tests of 04/20/87

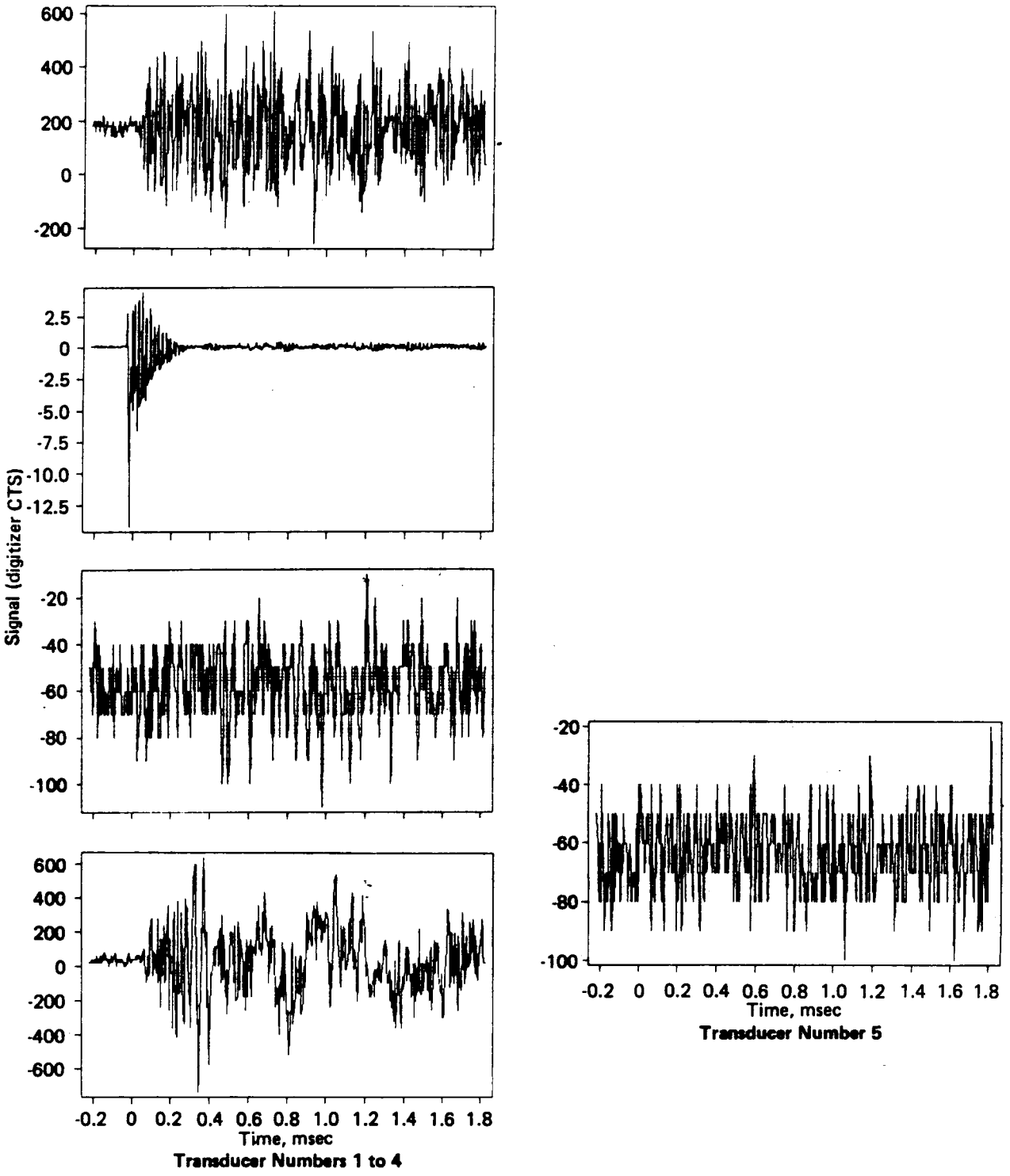

Figure A-19. Fourth Test of 04/20/87

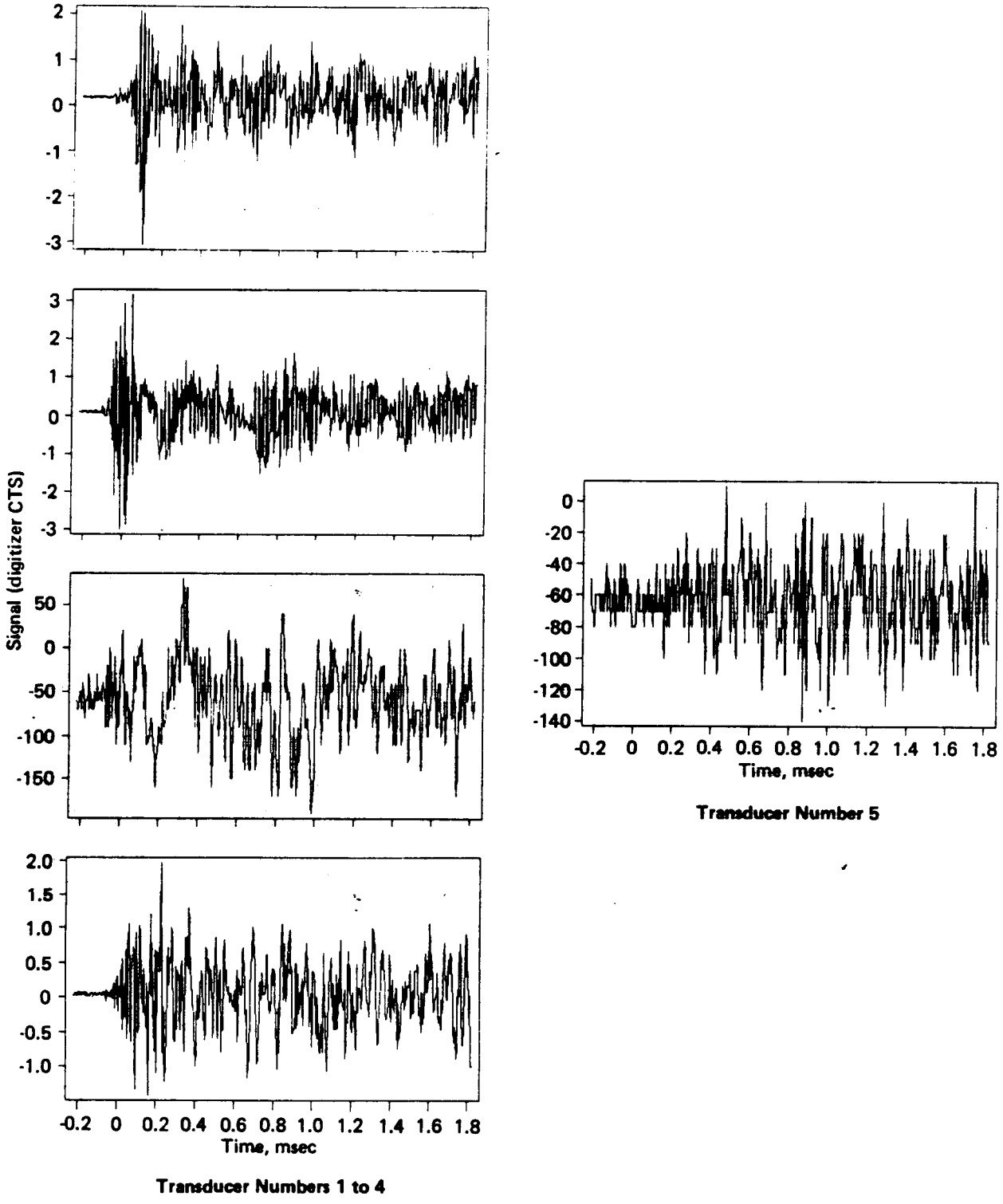

Figure A-20. Fifth Test of 04/20/87

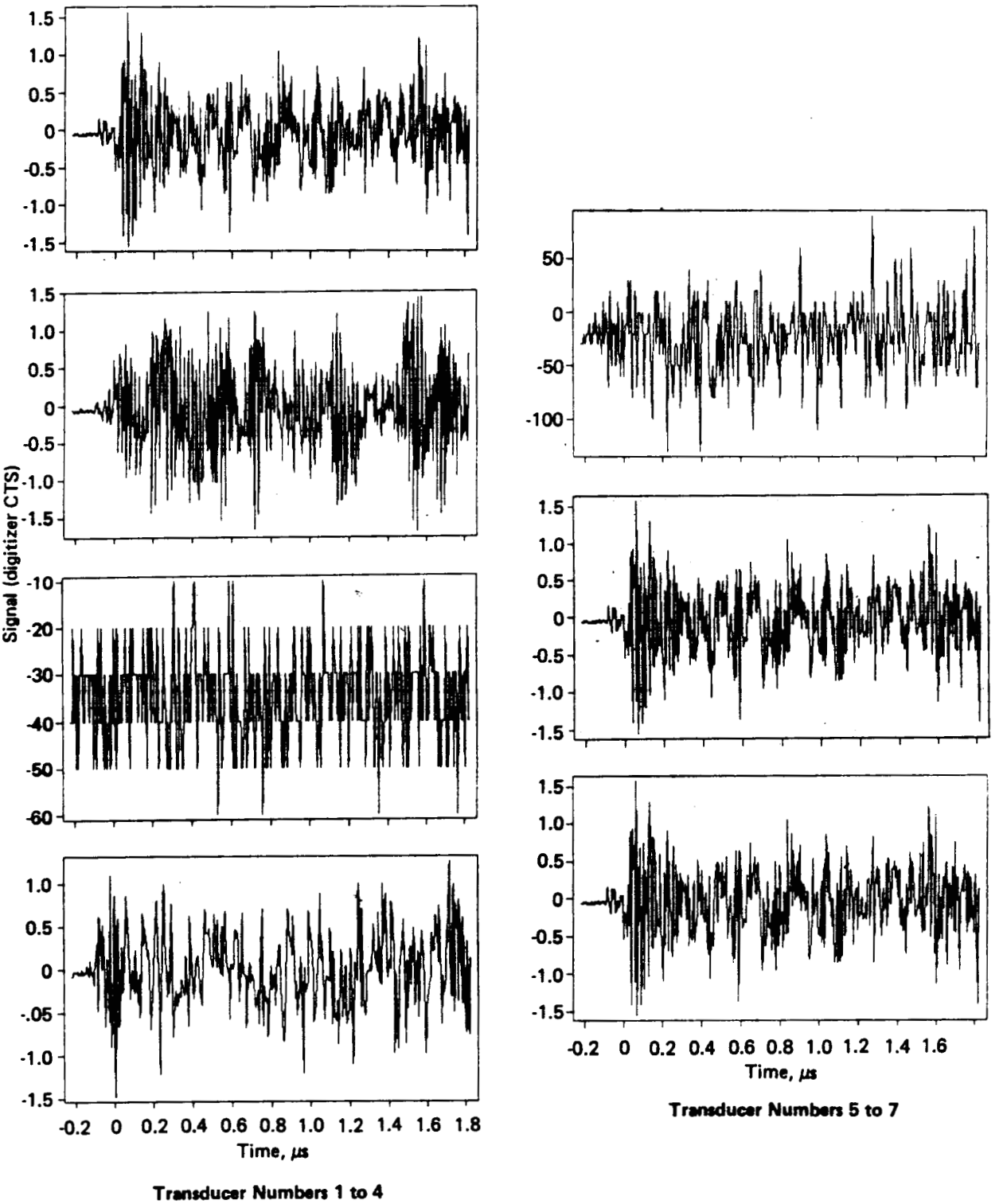

Figure A-21. Sixth Test of 04/20/87

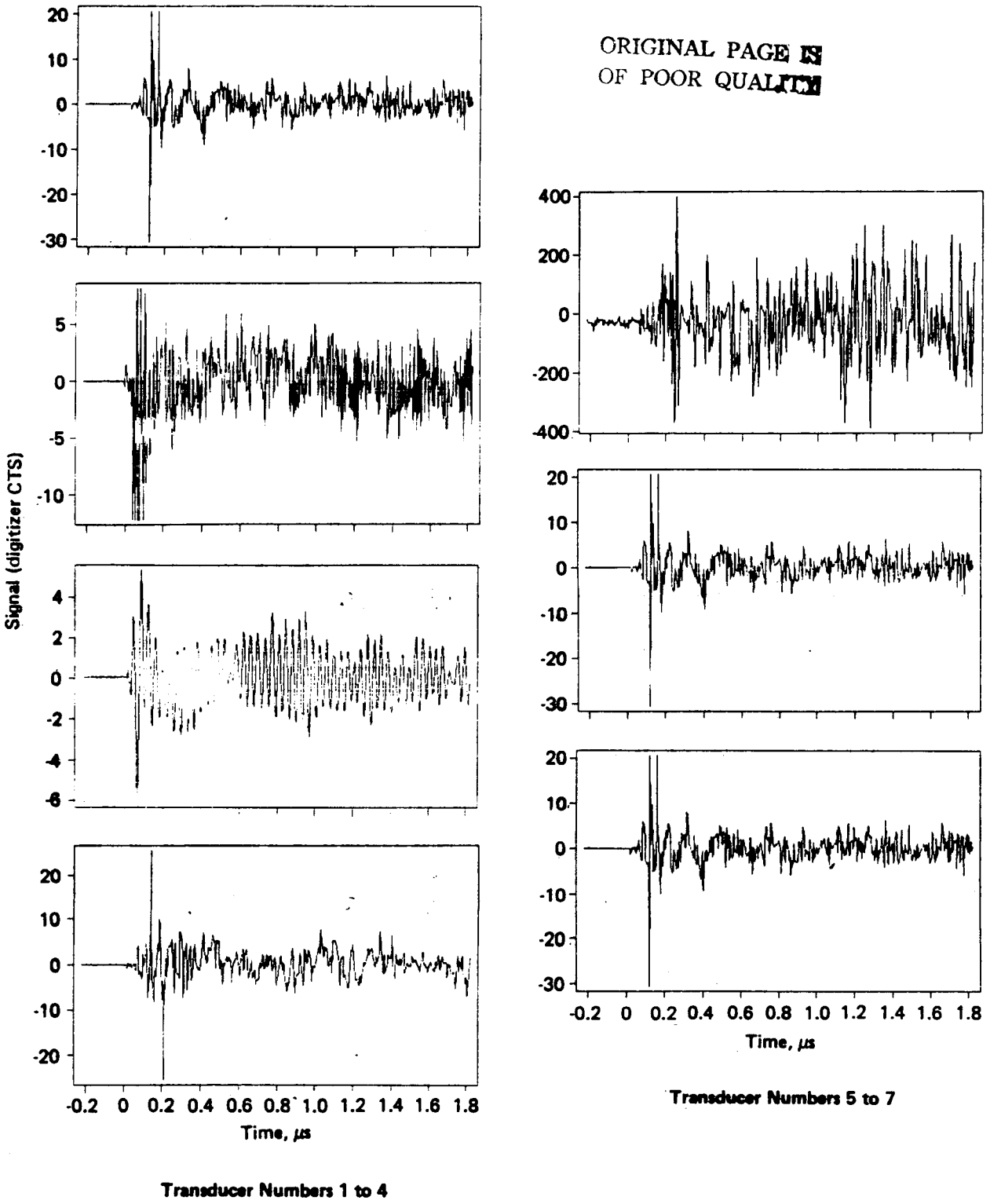

Figure A-22. First Test of 04/23/87

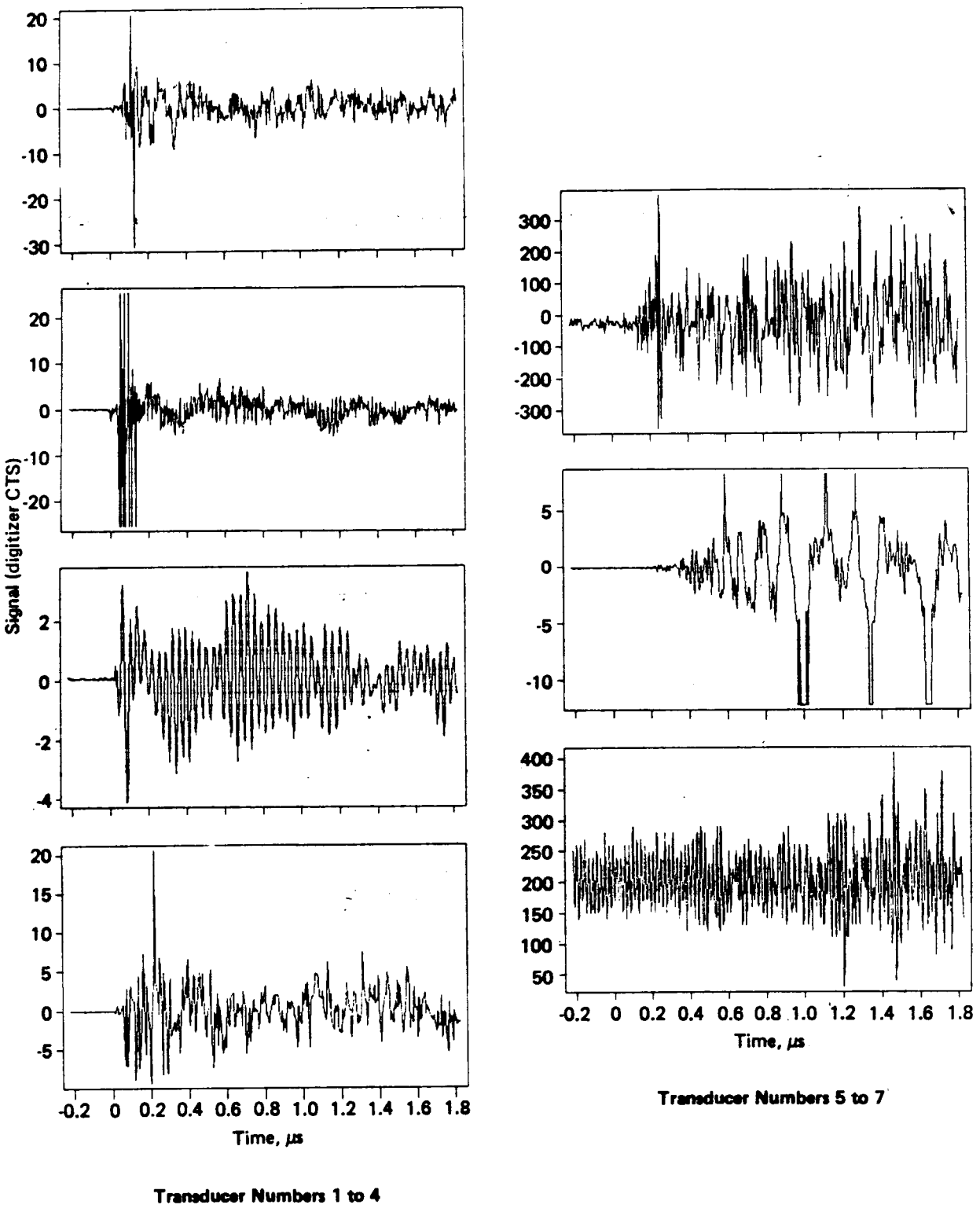

Figure A-23. Second Test of 04/23/87

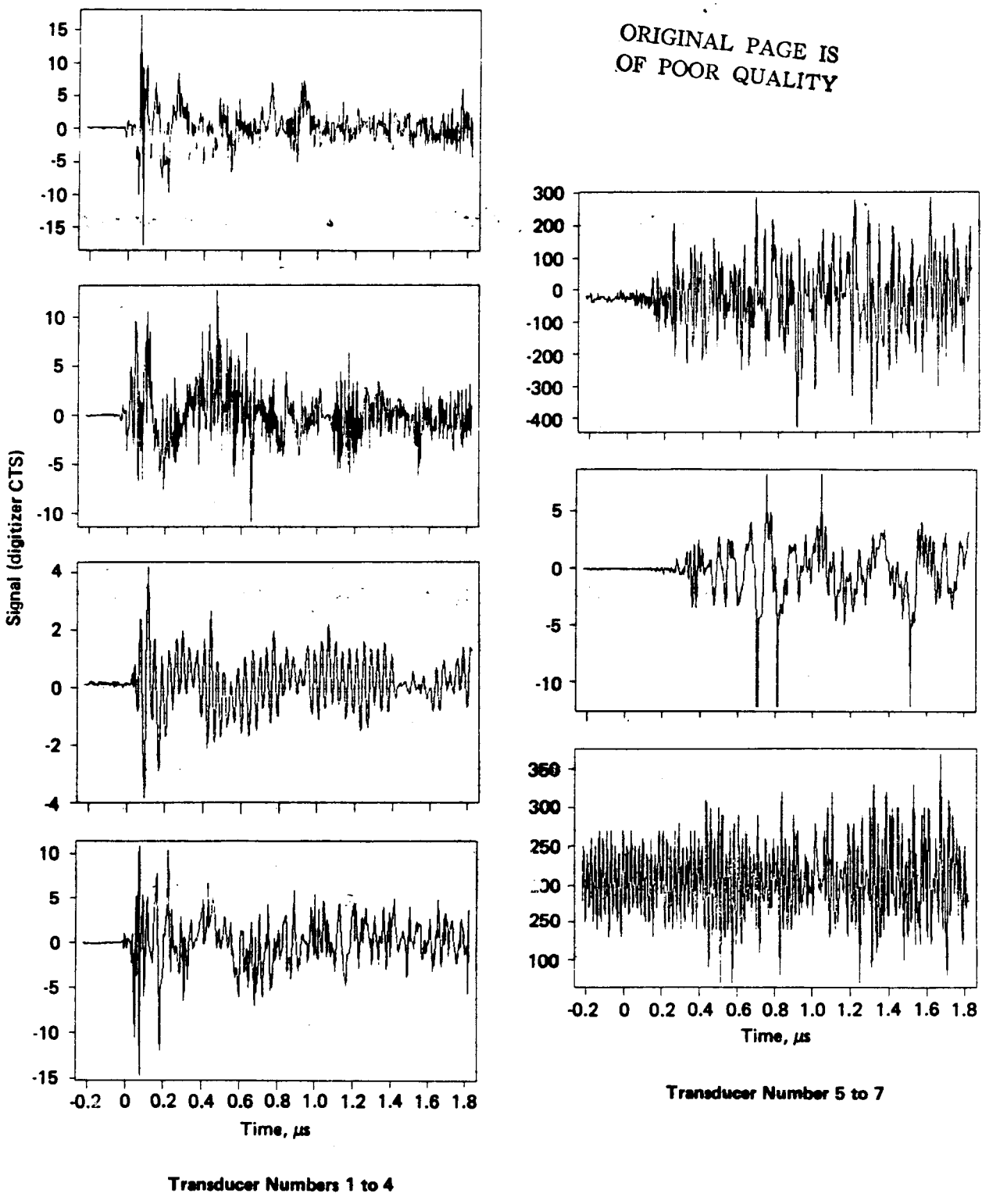

Figure A-24. Third Test of 04/23/87

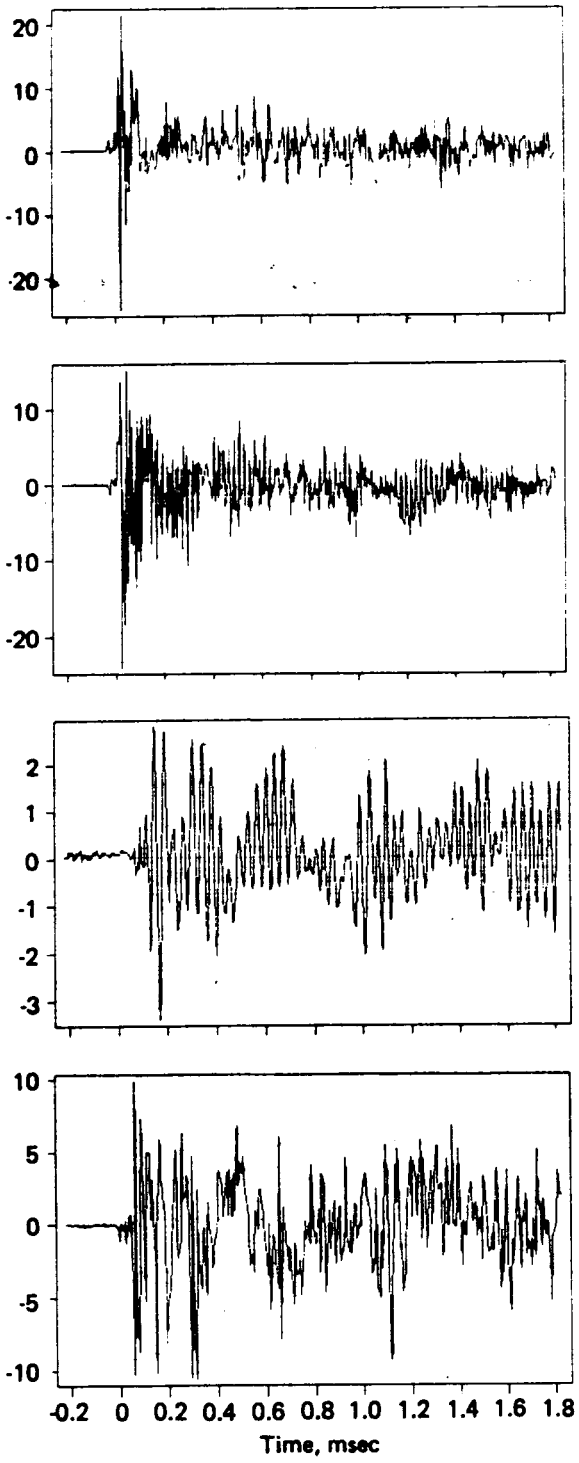

Transducer Numbers 1 to 4

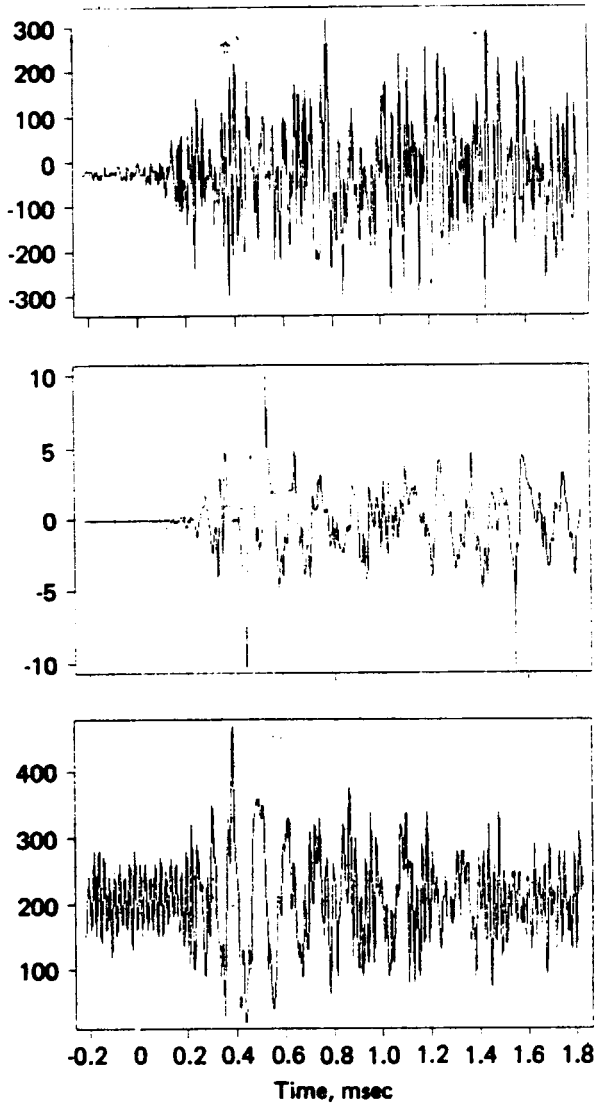

Transducer Numbers 5 to 7

Figure A-25. Fourth Test of 04/23/87

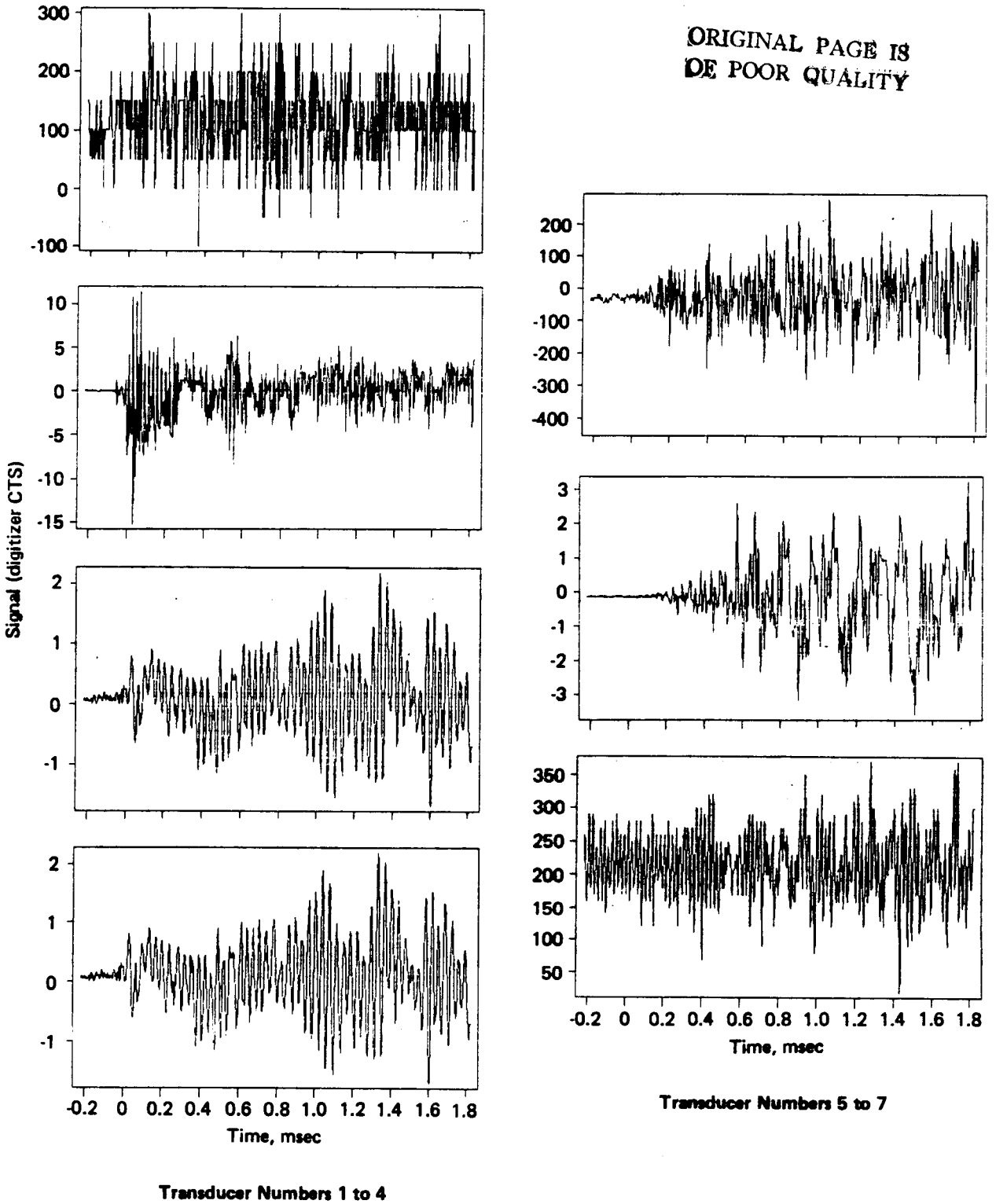

Figure A-26. Fifth Test of 04/23/87

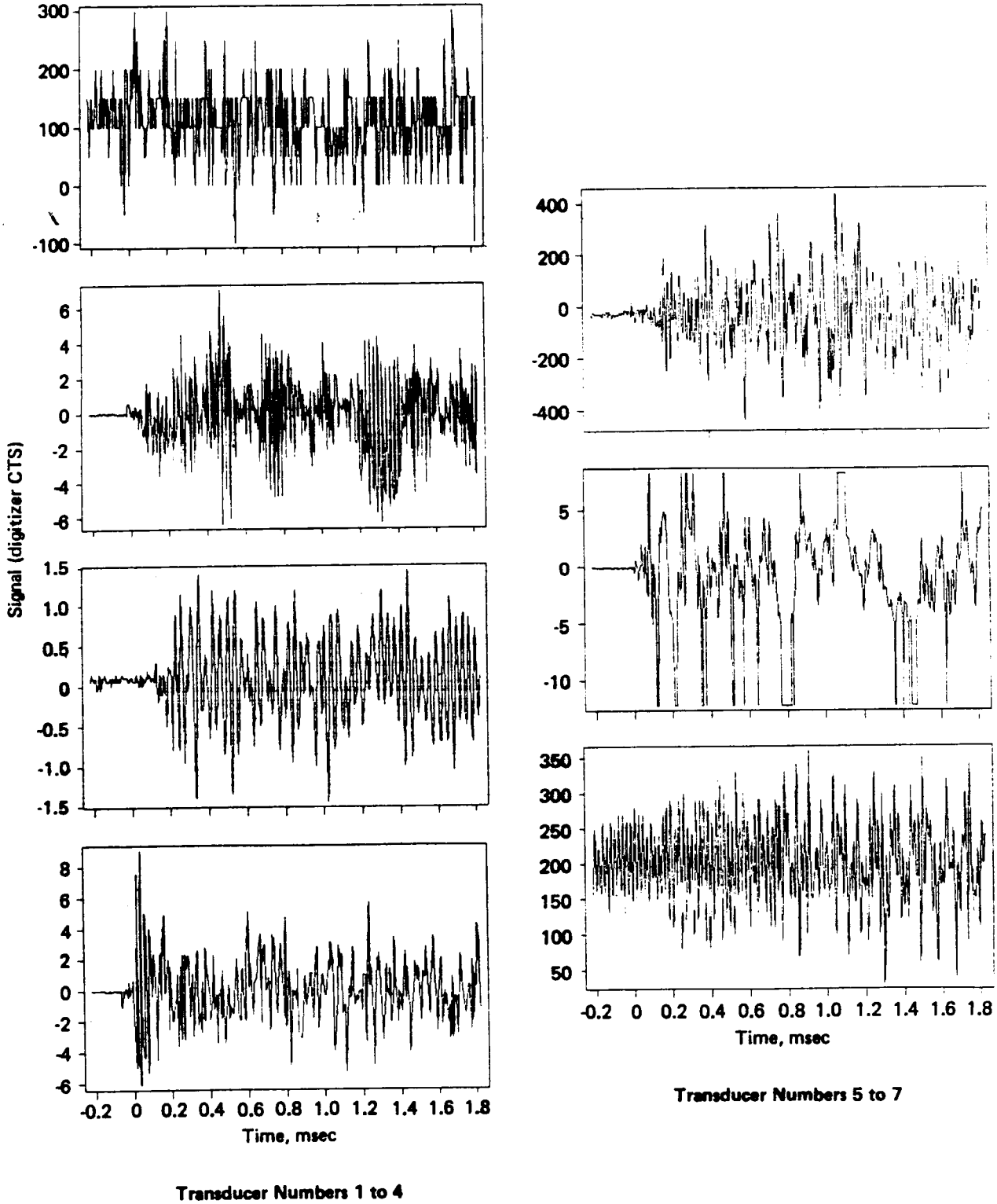

Figure A-27. Sixth Test of 04/23/87

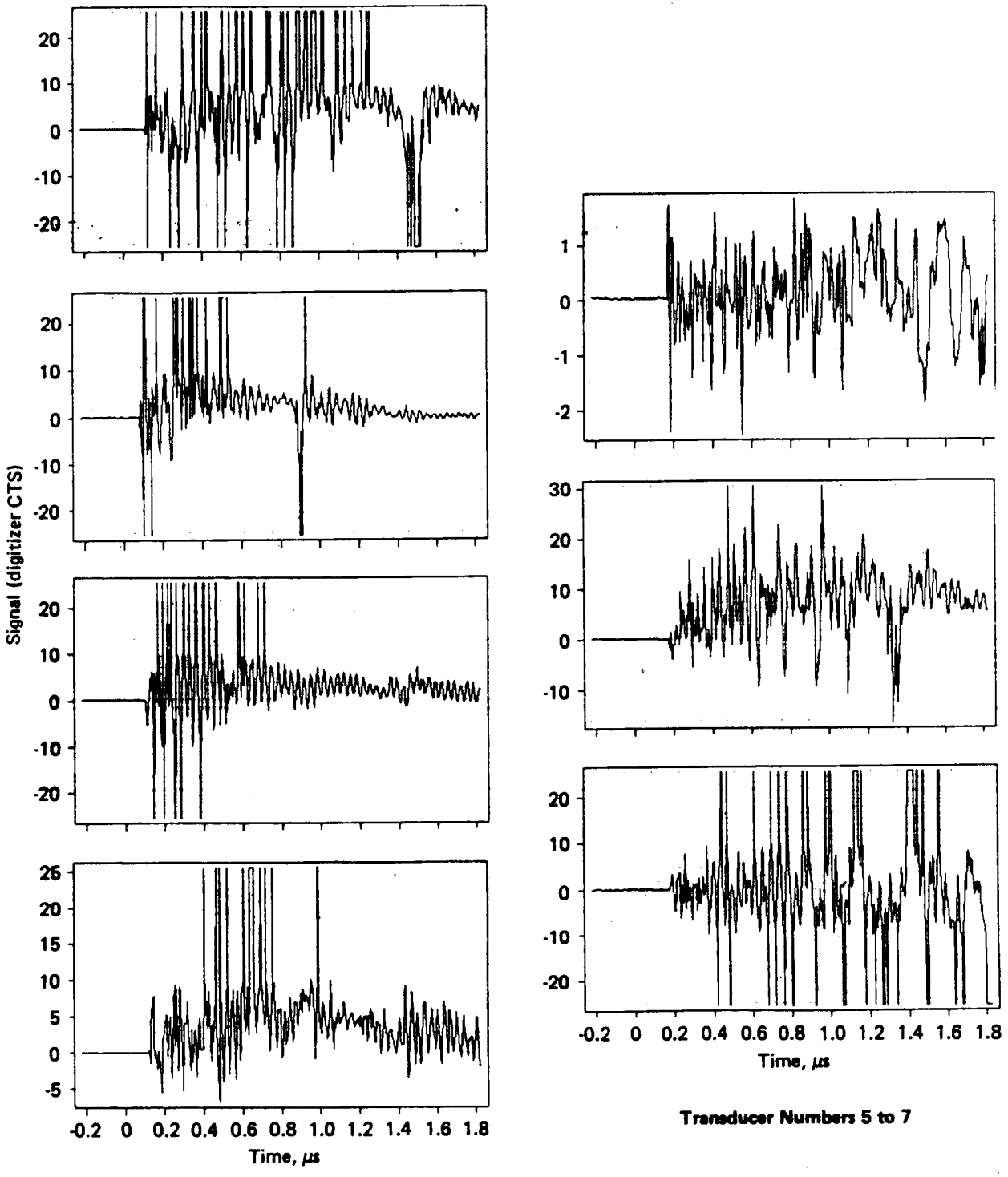

Figure A-28. First Test of 05/04/87

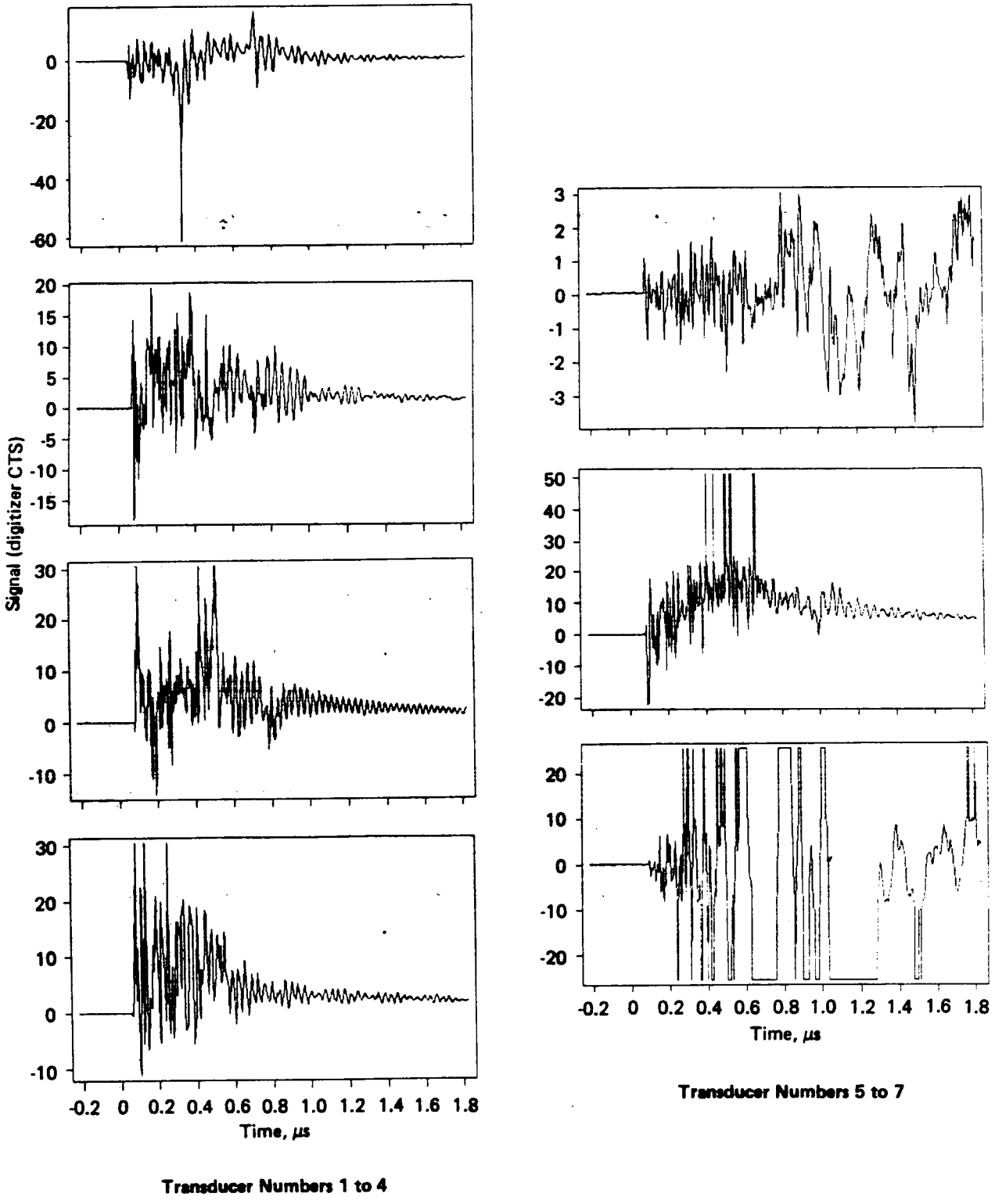

Figure A-29. Second Test of 05/04/87

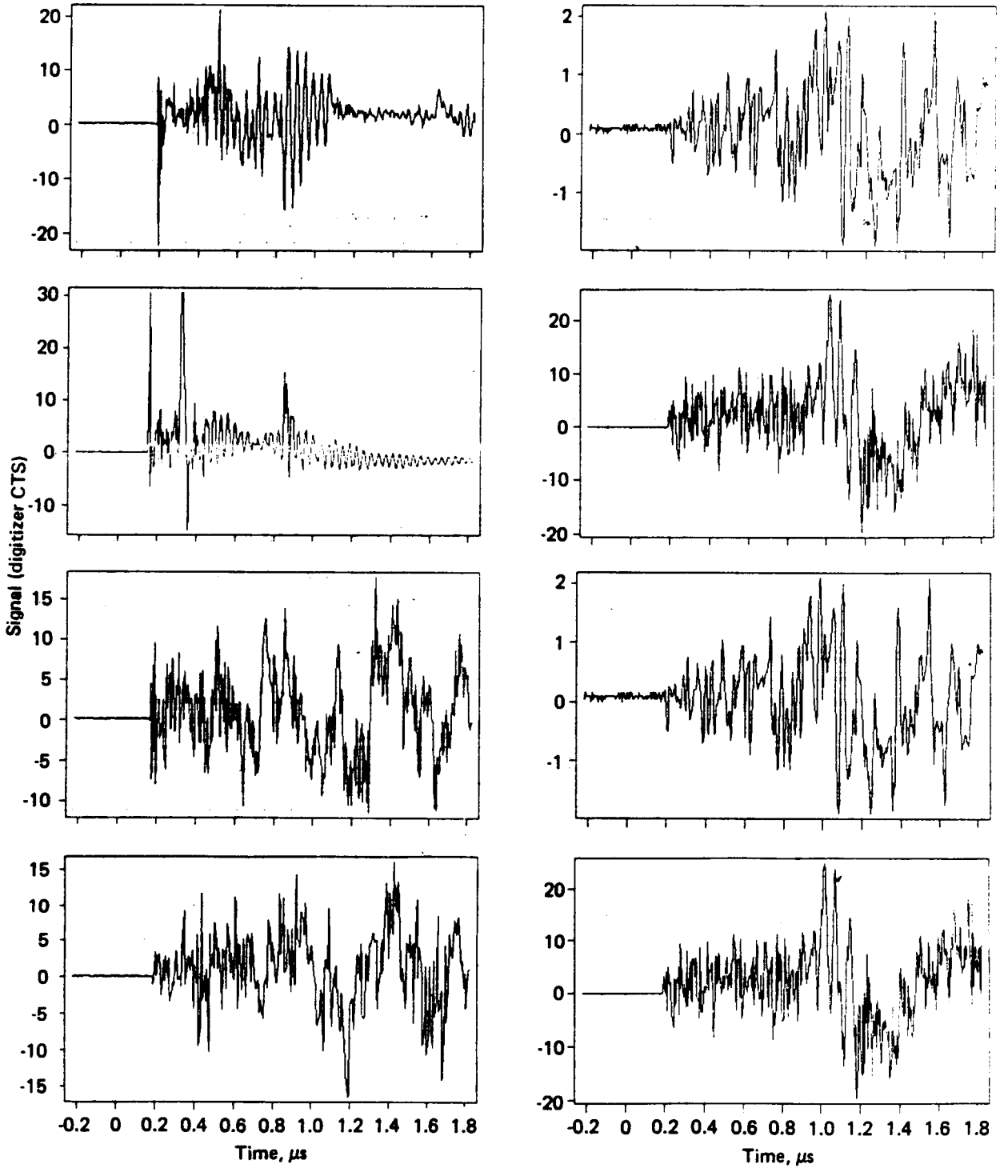

Figure A-30. First Test of 05/05/87

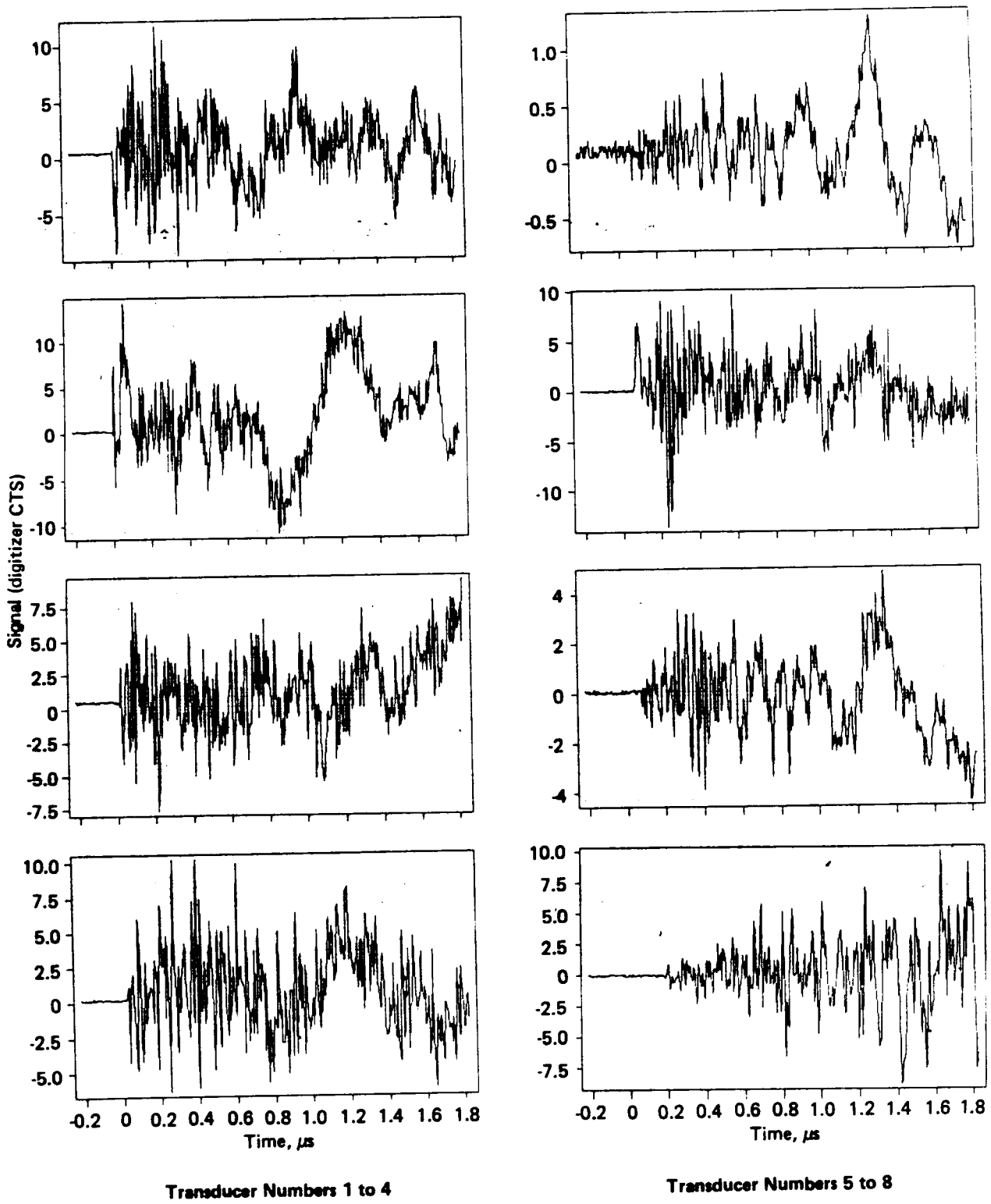

Figure A-31. Second Test of 05/06/87

Appendix B

Space Debirs Momentum Distribution

APPENDIX B

Space Debris Momentum Distribution

Fritz Scholz

Boeing Computer Services

Introduction: In order to obtain more accurate information about the space debris that forms a hazard for the space station it is proposed to use the cylindrical logistics module of the space station to gather space debris impact data. By equipping various outside panels of the cylinder with sensors it is possible to measure time, location and the surface normal momentum component M of each impact. In order to calibrate the impact sensors appropriately it is useful to have some idea of the distribution of the momentum M, i.e. how likely is it to get a momentum outside a certain range. Such an assessment is possible only if certain probabilistic modeling assumptions are made. These assumptions are not unreasonable but represent some simplification of reality. Further, once the model is assumed and the mathematical form of the momentum distribution function is derived, its evaluation still depends on the angle and diameter distributions of the debris particles. These distributions are known only imperfectly and it is the objective of this data gathering experiment to improve on that knowledge or confirm it. The next section discusses the probability modeling assumptions that underlie the derivation for the momentum distribution function. The formula for the distribution function is stated and a proof is given. The final section gives a formula for the expected number of hits of diameter d or greater on a given panel and for the full cylinder mantle some numerical values are given on a yearly basis for several values of d.

The Probability Model: Each debris particle can be characterized by its diameter D and the angle θ that its relative velocity vector forms with the space station flight direction. This relative velocity is then $v(\theta) = 2v_0 \cos(\theta)$ where v_0 is the common orbital velocity of space station and debris particle.

It is assumed that D and θ are independent random variables with respective densities $h(d)$ and $w(\theta)$. The distribution function of D is then $H(d) = P(D \leq d) = \int_0^d h(x)\,dx$ and $1 - H(d) = P(D > d)$ is denoted by $\overline{H}(d)$. It is assumed that the density $w(\theta)$ of θ is explicitly given. $H(d)$ is given only indirectly through the debris flux measure $F_{Deb}(d)$ which repre-

sents the average number of debris particles of diameter $\geq d$ that will pass through a cylinder with cross section 1 in unit time (the cylinder standing perpendicular to the orbital plane). This flux definition is bigger by a factor of 4 than the tumbling plate flux, see [1]. On page 13 of [1] it was shown that

$$\overline{H}(d)\lambda_0(\theta) = \frac{F_{Deb}(d)}{F_{Deb}(0)}|A|F_{Deb}(0)[\cos(\theta-\phi)]^+$$

which implies that $\overline{H}(d) = F_{Deb}(d)/F_{Deb}(0)$. There is a problem in that $F_{Deb}(d)$ is not given for $d < 10^{-2}$ cm and extrapolation suggests that $F_{Deb}(0) = \infty$. A way out of this dilemma is to define a threshold $\epsilon > 0$ such that diameters $\leq \epsilon$ are no longer considered to be space debris. Then define $H(d) = 1 - F_{Deb}(d)/F_{Deb}(\epsilon)$ for $d \geq \epsilon$ and $H(d) = 0$ for $d < \epsilon$. What constitutes a reasonable threshold ϵ is left open at this point.

Since the sensor will measure the surface normal momentum component of the debris particle it becomes necessary to introduce a surface area element A of the cylinder. It is most convenient to consider surface elements that represent narrow vertical rectangular strips on the outside cylinder wall. Such a segment is characterized by the angle ϕ that the ray from the cylinder center to strip centerline forms with the space station flight direction. ϕ may vary from 0 to 2π. If r represents the cylinder base radius, h the height of the rectangular strip and $rd\phi$ its base, then the area $|A|$ of A is $|A| \approx hrd\phi$. To emphasize the dependence of A on ϕ the notation A_ϕ is used. The normal momentum component of a debris particle of diameter D that impacts A_ϕ from direction θ is then $M = cD^3v(\theta)[\cos(\theta-\phi)]^+$ where c is the proportionality factor that relates volume to mass and $[\cos(\theta-\phi)]^+$ accounts for the surface normal part of the momentum which becomes zero whenever $\cos(\theta-\phi) < 0$.

The random process of arrivals of debris particles with their respective random angles and diameters D is modeled by a marked Poisson process N_ϕ with intensity

$$\lambda_\phi(t,\theta,d) = F_{Deb}(\epsilon)|A_\phi|[\cos(\theta-\phi)]^+w(\theta)h(d)I_{[0,\infty)}(t)$$

which is defined on $S = [0,\infty)\times[-\pi/2,\pi/2]\times[0,\infty)$. For any subset $C \subset S$ $N_\phi(C)$ represents the random number of debris particles which hit A_ϕ and which have characteristics $(t,\theta,d) \in C$. Here t refers to the arrival time

of the particles. Further, for any $C \subset S$ the random number $N_\phi(C)$ has a Poisson distribution with mean

$$\mu_\phi(C) = \int_C \lambda(t,\theta,d)\, d(t,\theta,d)$$

and for any $k = 1,2,3,\ldots$ and disjoint $C_1, \ldots, C_k \subset S$ the random variables $N_\phi(C_1), \ldots, N_\phi(C_k)$ are independent. For more details on marked Poisson processes see [2], [3].

A given vertical rectangular panel B on the outside of the cylinder can be thought of as approximated by many narrow strips A_ϕ, $\phi_1 \leq \phi \leq \phi_2$, where ϕ_1 and ϕ_2 delimit the base arc of the panel B. For each narrow strip A_ϕ a marked Poisson process N_ϕ is modeled and it is further assumed that these Poisson processes for different strips are independent. This construction seems reasonable enough since those particles that hit one strip on the outside are separate from the particles that hit any other strip on the outside.

The Momentum Distribution Function: Having made these modeling assumptions it is possible to give the following formula for the distribution function of M, namely

$$G(m) = P(M \leq m) = V/R\,,$$

where

$$V = \int_{\phi_1}^{\phi_2} \int_{-\pi/2}^{\pi/2} [\cos(\theta-\phi)]^+ w(\theta) H\left(\left(\frac{m}{cv(\theta)[\cos(\theta-\phi)]^+}\right)^{1/3}\right) d\theta d\phi$$

and

$$R = \int_{\phi_1}^{\phi_2} \int_{-\pi/2}^{\pi/2} [\cos(\theta-\phi)]^+ w(\theta) d\theta d\phi\,.$$

The proof for this will be given only for the momentum M_1 of the first particle that hits panel B. It is the same for any particle but the derivation is somewhat messier in notation.

Proof: If M_1 is the surface normal momentum component of the first debris particle to hit panel B and τ_1 its time of arrival then

$$G(m) = P(M_1 \leq m) = \lim_{T\to\infty} P(M_1 \leq m,\ \tau_1 < T)$$

and

$$P(M_1 \le m,\ \tau_1 < T) = \sum_{i=1}^{n} P(M_1 \le m,\ \tau_1 \in I_i)$$

where I_i is the interval $[T(i-1)/n, Ti/n)$ for $i = 1,\ 2,\ \ldots,\ n$. Let

$$C_{im} = \left\{ (t,\theta,d) :\ t \in I_i,\ d \le \left(\frac{m}{cv(\theta)[\cos(\theta-\phi)]^+} \right)^{1/3},\ \theta \in J_\phi \right\}$$

where $J_\phi = \{\theta \in [-\pi/2, \pi/2] :\ \cos(\theta-\phi) > 0\}$. C_{im} delineates the characteristics of any particle arriving on A_ϕ during I_i with surface normal momentum component $\le m$. Similarly, let

$$C_{i-1} = \{(t,\theta,d) :\ t \in [0, T(i-1)/n),\ d > 0,\ \theta \in J_\phi\}$$

Then $P(M_1 \le m,\ \tau_1 \in I_i)$ can also be written as

$$\begin{aligned}
&P(N_\phi(C_{i-1}) = 0\ \forall \phi \in [\phi_1, \phi_2], N_\psi(C_{im}) \ge 1 \text{ for some } \psi \in [\phi_1, \phi_2]) \\
&= P(N_\phi(C_{i-1}) = 0\ \forall \phi \in [\phi_1, \phi_2]) P(N_\psi(C_{im}) \ge 1 \text{ for some } \psi \in [\phi_1, \phi_2]) \\
&= \prod_\phi P(N_\phi(C_{i-1}) = 0) P(N_\psi(C_{im}) \ge 1 \text{ for some } \psi \in [\phi_1, \phi_2]) \\
&= \exp(-\sum_\phi \mu_\phi(C_{i-1})) P(N_\psi(C_{im}) \ge 1 \text{ for some } \psi \in [\phi_1, \phi_2])
\end{aligned}$$

where

$$\mu_\phi(C_{i-1}) = \frac{i-1}{n} T \int_{-\pi/2}^{\pi/2} F_{deb}(\epsilon) |A_\phi| [\cos(\theta-\phi)]^+ w(\theta)\ d\theta$$

so that $\sum_\phi \mu_\phi(C_{i-1})$ can be approximated by

$$\frac{i-1}{n} T F_{deb}(\epsilon) r h \int_{\phi_1}^{\phi_2} \int_{-\pi/2}^{\pi/2} [\cos(\theta-\phi)]^+ w(\theta)\ d\theta d\phi = \frac{i-1}{n} T F_{deb}(\epsilon) r h R\ .$$

Since

$$\begin{aligned}
P(N_\psi(C_{im}) \ge 1) &= P(N_\psi(C_{im}) = 1) + P(N_\psi(C_{im}) > 1) \\
&= \mu_\psi(C_{im}) \exp(-\mu_\psi(C_{im})) + P(N_\psi(C_{im}) > 1)
\end{aligned}$$

and

$$P(N_\psi(C_{im}) > 1) = 1 - \mu_\psi(C_{im}) - \mu_\psi(C_{im}) \exp(-\mu_\psi(C_{im})) \leq \mu_\psi^2(C_{im})/2$$

and since

$$\mu_\psi(C_{im}) = \frac{T}{n} \int_{-\pi/2}^{\pi/2} F_{Deb}(\epsilon) |A_\psi| [\cos(\theta - \psi)]^+ w(\theta) H \left(\left(\frac{m}{cv(\theta)[\cos(\theta - \psi)]^+} \right)^{1/3} \right) d\theta$$

which is of order $1/n$, we have

$$P(N_\psi(C_{im}) \geq 1) = P(N_\psi(C_{im}) = 1) + O(1/n^2)$$

and

$$P(N_\psi(C_{im}) = 1) = \mu_\psi(C_{im}) \exp(-\mu_\psi(C_{im})) = O(1/n) \ .$$

Thus (using Bonferroni's inequality) we have

$$P(N_\psi(C_{im}) \geq 1 \text{ for some } \psi \in [\phi_1, \phi_2]) = \sum_\psi P(N_\psi(C_{im}) = 1) + O(1/n^2)$$

and

$$\sum_\psi P(N_\psi(C_{im}) = 1) = \sum_\psi \mu_\psi(C_{im}) \exp(-\mu_\psi(C_{im}))$$

$$\approx \frac{T}{n} rhF_{Deb}(\epsilon) \int_{\phi_1}^{\phi_2} \int_{-\pi/2}^{\pi/2} [\cos(\theta - \psi)]^+ w(\theta) H \left(\left(\frac{m}{cv(\theta)[\cos(\theta - \psi)]^+} \right)^{1/3} \right) d\theta d\psi$$

$$= \frac{T}{n} rhF_{Deb}(\epsilon) V \ .$$

Hence

$$P(M_1 \leq m, \ \tau_1 < T) = \sum_{i=1}^{n} \exp\left(-\frac{i-1}{n} TF_{Deb}(\epsilon) rhR \right) \frac{T}{n} rhF_{Deb}(\epsilon) V + nO(1/n^2)$$

which, as a Riemann sum, approaches

$$\int_0^1 \exp(-xTF_{Deb}(\epsilon) rhR) dx \ TrhF_{Deb}(\epsilon) V = \frac{V}{R} (1 - \exp(-TF_{Deb}(\epsilon) rhR)) \to \frac{V}{R}$$

as $T \to \infty$. Hence $P(M_1 \leq m) = V/R$ as claimed.

Expected Number of Impacts: In order to gauge the feasibility of the experiment it is necessary to find out how many impacts of space debris particles of size d or greater can be expected for a given panel B. To obtain this expected value one proceeds as before by viewing the panel as approximated by many narrow panel strips and by adding the expected values for each of those. To get the expected value for a panel strip let

$$C_T = \{(t, \theta, d) : \ d \geq d_0, t \leq T, \theta \in J_\phi\} \ ,$$

then

$$\mu_\phi(C_T) = T\overline{H}(d_0) r h d\phi F_{Deb}(\epsilon) \int_{-\pi/2}^{\pi/2} [\cos(\theta - \phi)]^+ w(\theta) d\theta$$

$$= T r h d\phi F_{Deb}(d_0) \int_{-\pi/2}^{\pi/2} [\cos(\theta - \phi)]^+ w(\theta) d\theta$$

represents the expected number of debris impacts of diameter $\geq d_0$ during a time period of length T on the strip corresponding ϕ. By summing this over $\phi \in [\phi_1, \phi_2]$ one obtains the corresponding expected number for the full panel B as

$$T r h F_{Deb}(d_0) \int_{\phi_1}^{\phi_2} \int_{-\pi/2}^{\pi/2} [\cos(\theta - \phi)]^+ w(\theta) d\theta d\phi \ ,$$

which for $\phi_1 = 0$ and $\phi_2 = 2\pi$ simplifies after interchange of integration to $2TrhF_{Deb}(d_0)$, which fits in with the used definition of F_{Deb} since $2rh$ represents the cross section of the cylinder. Note that the expected number of impacts is independent of the threshold ϵ provided $d_0 \geq \epsilon$.

Taking the flux data for 400 km altitude as given in [4] for a tumbling plate and noting the factor 4 increase of F_{Deb} over this tumbling plate flux one can read off the following formula for F_{Deb}:

$$F_{Deb}(d) = 6.34 \cdot 10^{-6} \cdot d^{-2.4} \text{ for } d \leq 1.$$

Since the cross section area of the logistics module is about 23.7 m^2 one can expect about 9.5, .038, and .00015 yearly impacts of diameter $\geq$ .01, $\geq$ .1 and $\geq$ 1 respectively, on the outside mantle of the logistics module.

Also of interest is the expected number of impacts with surface normal momentum component $\geq m$. This expected value is obtained as before by

C-2

integrating the expected values over narrow strips. The expected value for a narrow strip is obtained by letting

$$C_{T,m} = \left\{ (t,\theta,d) : t \le T,\ d \ge \left(\frac{m}{cv(\theta)[\cos(\theta-\phi)]^+} \right)^{1/3},\ \theta \in J_\phi \right\}$$

and by computing

$$\mu_\phi(C_{T,m}) = TF_{Deb}(\epsilon) \int_{-\pi/2}^{\pi/2} |A_\phi| [\cos(\theta-\phi)]^+ w(\theta) \overline{H} \left(\left(\frac{m}{cv(\theta)[\cos(\theta-\phi)]^+} \right)^{1/3} \right) d\theta \ .$$

Summing this over $\phi \in [\phi_1, \phi_2]$ one obtains for the expected number of impacts of momentum components $\ge m$ on the panel B the following formula:

$$TrhF_{Deb}(\epsilon) \int_{\phi_1}^{\phi_2} \int_{-\pi/2}^{\pi/2} [\cos(\theta-\phi)]^+ w(\theta) \overline{H} \left(\left(\frac{m}{cv(\theta)[\cos(\theta-\phi)]^+} \right)^{1/3} \right) d\theta d\phi$$

which reduces to

$$Trh \int_{\phi_1}^{\phi_2} \int_{-\pi/2}^{\pi/2} [\cos(\theta-\phi)]^+ w(\theta) F_{Deb} \left(\left(\frac{m}{cv(\theta)[\cos(\theta-\phi)]^+} \right)^{1/3} \right) d\theta d\phi \ .$$

Note that the dependence on ϵ has disappeared as long as ϵ is chosen smaller than any possible argument in the F_{Deb} function. This depends mainly on the choice of m. Since $F_{Deb}(d)$ is not given for $d < 10^{-2}cm$ one still has to make the decision on how to extrapolate $F_{Deb}(d)$ below $10^{-2}cm$. One approach is to take the linear extrapolation on the log-log scale which leads to

$$F_{Deb}(d) = 6.34 \cdot 10^{-6} \cdot d^{-2.4} \text{ for } d \le 1.$$

The other approach is to truncate $F_{Deb}(d)$ for $d \le 10^{-2}cm$ by setting $F_{Deb}(d) = F_{Deb}(10^{-2}cm)$ for $d \le 10^{-2}cm$. The rationale behind that is to treat all particles with diameter $\le 10^{-2}cm$ no longer as debris.

References

[1] F.W. Scholz, "Space Station Penetration Probability Model" revised version, April 15, 1987.

[2] H.M. Taylor and S. Karlin (1981), *A Second Course in Stochastic Processes,* Academic Press, New York.

[3] H.M. Taylor and S. Karlin (1984), *An Introduction to Stochastic Modeling,* Academic Press, Orlando, Florida.

[4] D.J. Kessler, "Orbital Debris Environment for Space Station" JSC–20001.